

Effect of Protuberance Shape and Orientation on Space Shuttle Orbiter Boundary-Layer Transition

*Rudolph A. King, Scott A. Berry, Michael A. Kegerise
Langley Research Center, Hampton, Virginia*

The NASA STI Program Office ... in Profile

Since its founding, NASA has been dedicated to the advancement of aeronautics and space science. The NASA Scientific and Technical Information (STI) Program Office plays a key part in helping NASA maintain this important role.

The NASA STI Program Office is operated by Langley Research Center, the lead center for NASA's scientific and technical information. The NASA STI Program Office provides access to the NASA STI Database, the largest collection of aeronautical and space science STI in the world. The Program Office is also NASA's institutional mechanism for disseminating the results of its research and development activities. These results are published by NASA in the NASA STI Report Series, which includes the following report types:

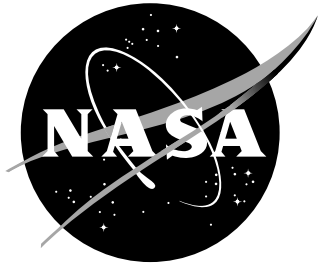
- **TECHNICAL PUBLICATION.** Reports of completed research or a major significant phase of research that present the results of NASA programs and include extensive data or theoretical analysis. Includes compilations of significant scientific and technical data and information deemed to be of continuing reference value. NASA counterpart of peer-reviewed formal professional papers, but having less stringent limitations on manuscript length and extent of graphic presentations.
- **TECHNICAL MEMORANDUM.** Scientific and technical findings that are preliminary or of specialized interest, e.g., quick release reports, working papers, and bibliographies that contain minimal annotation. Does not contain extensive analysis.
- **CONTRACTOR REPORT.** Scientific and technical findings by NASA-sponsored contractors and grantees.

- **CONFERENCE PUBLICATION.** Collected papers from scientific and technical conferences, symposia, seminars, or other meetings sponsored or co-sponsored by NASA.
- **SPECIAL PUBLICATION.** Scientific, technical, or historical information from NASA programs, projects, and missions, often concerned with subjects having substantial public interest.
- **TECHNICAL TRANSLATION.** English-language translations of foreign scientific and technical material pertinent to NASA's mission.

Specialized services that complement the STI Program Office's diverse offerings include creating custom thesauri, building customized databases, organizing and publishing research results ... even providing videos.

For more information about the NASA STI Program Office, see the following:

- Access the NASA STI Program Home Page at ***<http://www.sti.nasa.gov>***
- E-mail your question via the Internet to help@sti.nasa.gov
- Fax your question to the NASA STI Help Desk at (301) 621-0134
- Phone the NASA STI Help Desk at (301) 621-0390
- Write to:
NASA STI Help Desk
NASA Center for AeroSpace Information
7115 Standard Drive
Hanover, MD 21076-1320



Effect of Protuberance Shape and Orientation on Space Shuttle Orbiter Boundary-Layer Transition

*Rudolph A. King, Scott A. Berry, Michael A. Kegerise
Langley Research Center, Hampton, Virginia*

National Aeronautics and
Space Administration

Langley Research Center
Hampton, Virginia 23681-2199

Acknowledgments

This wind-tunnel test would not have been possible without the support and dedication of many individuals: Michael Powers and Mark Griffith for ceramic model fabrication; Pete Veneris for fiducial-mark placement; Walter Wade, Kevin Bonilla and John Hopkins for manufacturing the boundary-layer trips; Gary Wainwright and Louis Simmons for manufacturing the hole template and drilling the holes for trip placement; and Grace Gleason, Rhonda Mills, Harry "Buddy" Stotler and Teck-Seng Kwa for 20-Inch Mach 6 Air Tunnel support and data acquisition. The authors are grateful for their contributions.

The use of trademarks or names of manufacturers in this report is for accurate reporting and does not constitute an official endorsement, either expressed or implied, of such products or manufacturers by the National Aeronautics and Space Administration.
--

Available from:

NASA Center for AeroSpace Information (CASI)
7115 Standard Drive
Hanover, MD 21076-1320
(301) 621-0390

National Technical Information Service (NTIS)
5285 Port Royal Road
Springfield, VA 22161-2171
(703) 605-6000

Abstract

This document describes an experimental study conducted to examine the effects of protuberances on hypersonic boundary-layer transition. The experiment was conducted in the Langley 20-Inch Mach 6 Tunnel on a series of 0.9%-scale Shuttle Orbiter models. The data were acquired to complement the existing ground-based boundary-layer transition database that was used to develop Version 1.0 of the boundary-layer transition RTF (return-to-flight) tool. The existing ground-based data were all acquired on 0.75%-scale Orbiter models using diamond-shaped (“pizza-box”) trips. The larger model scale facilitated in manufacturing higher fidelity protuberances. The end use of this experimental database will be to develop a technical basis (in the form of a boundary-layer transition correlation) to assess representative protrusion shapes, e.g., gap fillers and protrusions resulting from possible tile repair concepts. The primary objective of this study is to investigate the effects of protuberance-trip location and geometry on Shuttle Orbiter boundary-layer transition. Secondary goals are to assess the effects of gap-filler orientation and other protrusion shapes on boundary-layer transition. Global heat-transfer images using phosphor thermography of the Orbiter windward surface and the corresponding streamwise and spanwise heating distributions were used to infer the state of the boundary layer, i.e., laminar, transitional, or turbulent.

Contents

List of Tables	3
List of Figures	4
1 Introduction	7
2 Experimental Methods	8
2.1 Test Facility	8
2.2 Test Models	8
2.3 Test Instrumentation	10
2.4 Data Analysis	11
2.5 Test Matrix and Tunnel Conditions	13
3 Results and Discussion	13
3.1 Untripped Data	14
3.2 Tripped Data	15
4 Summary	17
References	19

List of Tables

1	Plug locations for the tripped model configurations.	21
2	Fiducial locations on all the final models.	21
3	Protuberance dimensions and quantities requested to be manufactured. Note that the trip heights, k , in the table are the designed values, not the as-built heights.	21
4	Proposed test plan and test conditions for models with protuberances (base- line configuration tests not included).	22
5	Test 6922 final run log.	23
5	Test 6922 final run log – (Cont).	24
5	Test 6922 final run log – (Cont).	25
5	Test 6922 final run log – (Cont).	26
6	Final Test 6922 matrix and BLT Tool v.1 flow parameters based on LATCH solutions for models with protuberances (baseline configuration test results not included). The nominal Mach number is $M = 6$ for all test conditions. . .	27

List of Figures

1	Photograph of a 0.9%-scale Orbiter model installed in the LaRC 20-Inch Mach 6 Air Tunnel.	28
2	Sketch of a 0.9%-scale Orbiter model installed in the LaRC 20-Inch Mach 6 Air Tunnel.	28
3	Windward surface sketch of the 7 models used for Test 6922. Holes to accommodate metal dowels are indicated by the filled blue circles.	29
4	Schematic of trip-dowel assemblies used as protuberances.	30
5	Photograph of four typical trip-dowel assemblies used as protuberances are shown above to demonstrate the scale of the trips. The trip-dowel assemblies shown from left to right are a pizza-box trip, a rounded pizza-box trip, a hemisphere trip, and a fence trip.	31
6	Schematic depicting a blank dowel inserted into a cast ceramic model to match OML of surface.	32
7	Illustration of phosphor thermography acquisition system.	33
8	Photographic image of model 1 installed in the 20-Inch Mach 6 Air Tunnel.	34
9	Global aeroheating images for baseline model 1.	35
10	Streamwise line cuts of normalized heat-transfer measurements at $y/L_{ref} = 0$ for baseline model 1.	36
11	Spanwise line cuts of normalized heat-transfer measurements at $x/L_{ref} = 0.9$ for baseline model 1.	36
12	Sketch and close-up image of model 2 with a blank dowel installed.	37
13	Streamwise line cuts of normalized heat-transfer measurements at $y/L_{ref} = 0$ for model 2 with a blank dowel and baseline model 1.	38
14	Spanwise line cuts of normalized heat-transfer measurements at $x/L_{ref} = 0.9$ for model 2 with a blank dowel and baseline model 1.	38
15	Close-up image of model 2 with configuration 1.	39
16	Global aeroheating images for model 2 with configuration 1.	40
17	Streamwise line cuts of normalized heat-transfer measurements at $y/L_{ref} = 0$ for model 2 with configuration 1.	41
18	Spanwise line cuts of normalized heat-transfer measurements at $x/L_{ref} = 0.9$ for model 2 with configuration 1.	41
19	Close-up image of model 2 with configuration 2. Clockwise rotation of fence relative to model centerline is denoted as positive angle.	42
20	Global aeroheating images for model 2 with configuration 2.	43
21	Streamwise line cuts of normalized heat-transfer measurements at $y/L_{ref} = 0$ for model 2 with configuration 2.	44
22	Spanwise line cuts of normalized heat-transfer measurements at $x/L_{ref} = 0.9$ for model 2 with configuration 2.	44
23	Sketch and close-up image of model 3 with three blank dowels installed.	45
24	Streamwise line cuts of normalized heat-transfer measurements at $y/L_{ref} = 0$ for model 3 with three blank dowels and baseline model 1.	46
25	Spanwise line cuts of normalized heat-transfer measurements at $x/L_{ref} = 0.9$ for model 3 with three blank dowels and baseline model 1.	46
26	Close-up image of model 3 with configuration 5. Clockwise rotation of fence relative to model centerline is denoted as positive angle.	47
27	Global aeroheating images for model 3 with configuration 5.	48
28	Streamwise line cuts of normalized heat-transfer measurements at $y/L_{ref} = 0$ for model 3 with configuration 5.	49
29	Spanwise line cuts of normalized heat-transfer measurements at $x/L_{ref} = 0.9$ for model 3 with configuration 5.	49

30	Close-up image of model 3 with configuration 5A. Clockwise rotation of fence relative to model centerline is denoted as positive angle.	50
31	Global aeroheating images for model 3 with configuration 5A.	51
32	Streamwise line cuts of normalized heat-transfer measurements at $y/L_{ref} = 0$ for model 3 with configuration 5A.	52
33	Spanwise line cuts of normalized heat-transfer measurements at $x/L_{ref} = 0.9$ for model 3 with configuration 5A.	52
34	Close-up image of model 3 with configuration 5B. Clockwise rotation of fence relative to model centerline is denoted as positive angle.	53
35	Global aeroheating images for model 3 with configuration 5B.	54
36	Streamwise line cuts of normalized heat-transfer measurements at $y/L_{ref} = 0$ for model 3 with configuration 5B.	55
37	Spanwise line cuts of normalized heat-transfer measurements at $x/L_{ref} = 0.9$ for model 3 with configuration 5B.	55
38	Close-up image of model 4 with three blank dowels installed.	56
39	Global aeroheating images for model 4 with three blank dowels.	57
40	Streamwise line cuts of normalized heat-transfer measurements at $y/L_{ref} = 0$ for model 4 with three blank dowels.	58
41	Spanwise line cuts of normalized heat-transfer measurements at $x/L_{ref} = 0.8$ for model 4 with three blank dowels	58
42	Streamwise line cuts of normalized heat-transfer measurements at $y/L_{ref} = 0$ for model 4 with three blank dowels and baseline model 1.	59
43	Spanwise line cuts of normalized heat-transfer measurements at $x/L_{ref} = 0.8$ for model 4 with three blank dowels and baseline model 1.	59
44	Close-up image of model 4 with configuration 6A. Clockwise rotation of fence relative to model centerline is denoted as positive angle.	60
45	Global aeroheating images for model 4 with configuration 6A.	61
46	Streamwise line cuts of normalized heat-transfer measurements at $y/L_{ref} = 0$ for model 4 with configuration 6A.	62
47	Spanwise line cuts of normalized heat-transfer measurements at $x/L_{ref} = 0.9$ for model 4 with configuration 6A.	62
48	Close-up image of model 4 with configuration 6B. Diagonal of PB trip is at 45° from model centerline.	63
49	Global aeroheating images for model 4 with configuration 6B.	64
50	Streamwise line cuts of normalized heat-transfer measurements at $y/L_{ref} = 0$ for model 4 with configuration 6B.	65
51	Spanwise line cuts of normalized heat-transfer measurements at $x/L_{ref} = 0.9$ for model 4 with configuration 6B.	65
52	Close-up image of model 4 with configuration 6C. Diagonal of PB trip is approximately -22.5° from model centerline.	66
53	Global aeroheating images for model 4 with configuration 6C.	67
54	Streamwise line cuts of normalized heat-transfer measurements at $y/L_{ref} = 0$ for model 4 with configuration 6C.	68
55	Spanwise line cuts of normalized heat-transfer measurements at $x/L_{ref} = 0.9$ for model 4 with configuration 6C.	68
56	Close-up image of model 6 with a blank dowel installed.	69
57	Global aeroheating images for model 6 with a blank dowel.	70
58	Streamwise line cuts of normalized heat-transfer measurements at $y/L_{ref} = 0$ for model 6 with a blank dowel.	71
59	Spanwise line cuts of normalized heat-transfer measurements at $x/L_{ref} = 0.9$ for model 6 with a blank dowel.	71

60	Streamwise line cuts of normalized heat-transfer measurements at $y/L_{ref} = 0$ for model 6 with a blank dowel and baseline model 1.	72
61	Spanwise line cuts of normalized heat-transfer measurements at $x/L_{ref} = 0.8$ for model 6 with a blank dowel and baseline model 1.	72
62	Close-up image of model 6 with configuration 12.	73
63	Global aeroheating images for model 6 with configuration 12.	74
64	Streamwise line cuts of normalized heat-transfer measurements at $y/L_{ref} = 0$ for model 6 with configuration 12.	75
65	Spanwise line cuts of normalized heat-transfer measurements at $x/L_{ref} = 0.9$ for model 6 with configuration 12.	75
66	Close-up image of model 6 with configuration 12B.	76
67	Global aeroheating images for model 6 with configuration 12B.	77
68	Streamwise line cuts of normalized heat-transfer measurements at $y/L_{ref} = 0$ for model 6 with configuration 12B.	78
69	Spanwise line cuts of normalized heat-transfer measurements at $x/L_{ref} = 0.9$ for model 6 with configuration 12B.	78
70	Close-up image of model 6 with configuration 12A.	79
71	Global aeroheating images for model 6 with configuration 12A.	80
72	Streamwise line cuts of normalized heat-transfer measurements at $y/L_{ref} = 0$ for model 6 with configuration 12A.	81
73	Spanwise line cuts of normalized heat-transfer measurements at $x/L_{ref} = 0.9$ for model 6 with configuration 12A.	81
74	Photographic image of model 7 installed in the 20-Inch Mach 6 Air Tunnel.	82
75	Global aeroheating images for baseline model 7.	83
76	Streamwise line cuts of normalized heat-transfer measurements at $y/L_{ref} = 0$ for baseline model 7.	84
77	Spanwise line cuts of normalized heat-transfer measurements at $x/L_{ref} = 0.9$ for baseline model 7.	84
78	Global aeroheating images for baseline model 7 and baseline model 1.	85
79	Streamwise line cuts of normalized heat-transfer measurements at $y/L_{ref} = 0$ for baseline model 7 and baseline model 1.	86
80	Sketch and close-up image of model 5 with three blank dowels installed.	87
81	Streamwise line cuts of normalized heat-transfer measurements at $y/L_{ref} = 0$ for model 5 with three blank dowels and baseline model 1.	88
82	Spanwise line cuts of normalized heat-transfer measurements at $x/L_{ref} = 0.9$ for model 5 with three blank dowels and baseline model 1.	88
83	Close-up image of model 5 with configuration 8.	89
84	Global aeroheating images for model 5 with configuration 8.	90
85	Streamwise line cuts of normalized heat-transfer measurements at $y/L_{ref} = 0$ for model 5 with configuration 8.	91
86	Spanwise line cuts of normalized heat-transfer measurements at $x/L_{ref} = 0.9$ for model 5 with configuration 8.	91
87	Close-up image of model 5 with configuration 8A.	92
88	Global aeroheating images for model 5 with configuration 8A.	93
89	Streamwise line cuts of normalized heat-transfer measurements at $y/L_{ref} = 0$ for model 5 with configuration 8A.	94
90	Spanwise line cuts of normalized heat-transfer measurements at $x/L_{ref} = 0.9$ for model 5 with configuration 8A.	94
91	Comparison of existing Mach 6 data and newly acquired TEI data in the parameter space of the BLT Tool v.1.	95

1 Introduction

The Entry Aeroheating Working Group led by NASA Johnson Space Center was created as a result of the Columbia Accident Investigation Board’s (CAIB) final report [1] to address the health of the Orbiter’s thermal protection system (TPS) prior to reentry. Part of the charter of this working group (see Ref. [2] for details) is to provide real-time support to the Damage Assessment Team during each Shuttle mission subsequent to STS-107 (STS - Space Transportation System). Damage to the ceramic tiles that cover a majority of the Shuttle windward surface is typically in the form of cavities resulting from debris impact during launch, but can also comprise of protruding gap fillers from between the tiles. Depending on the size and location of the resulting cavity or protrusion, the localized change in the outer mold line (OML) may destabilize the windward surface boundary layer and lead to premature boundary-layer transition during reentry. The boundary-layer transition (BLT) tool, which is one of the suite of engineering tools developed by the working group, is used in a rapid-turnaround environment to assess if and when these damage sites can cause early transition on the windward surface. At the time of this study, the version of the BLT Tool approved by the Shuttle Program was Version 1.0 [3–5]. This tool requires size, location and geometry (i.e., cavity versus protuberance) of the damage/repair sites obtained from on-orbit inspection to infer the expected time within the flight trajectory of boundary-layer transition onset relative to entry interface. Early transition times (i.e., occurring at high reentry Mach numbers) can lead to excessive thermal loads on the TPS and can ultimately affect the safety margins of the vehicle.

The BLT Tool (Version 1.0) is based on correlations of identified thresholds for boundary-layer transition from discrete elements that simulate TPS damage/repair on the Orbiter. That correlation methodology was established through a series of hypersonic wind-tunnel experiments on scaled Shuttle models with simulated TPS damage/repair on the windward surface [6, 7] and limited Orbiter flight data (recently reexamined flight data presented in Ref. [8]). The focus of this study is to examine TPS damage in the form of raised protuberances on the windward surface of the Orbiter. These protuberances are in the form of gap fillers, raised tiles and potential tile repair concepts. The experimental wind-tunnel database developed by Liechty *et al.* [6] was acquired on 0.75%-scaled Orbiter models with protuberances in the form of diamond-shaped (“pizza-box”) trips. The data were obtained in NASA Langley Research Center (LaRC) Aerothermodynamic Laboratory (LAL) which consists of three hypersonic wind tunnels [9]. The three tunnels are the 20-Inch Mach 6 Air Tunnel, the 20-Inch Mach 6 CF₄ Tunnel, and the 31-Inch Mach 10 Air Tunnel. The test parametrics included angle-of-attack of 30 and 40 degrees, side-slip angle of 0 degrees, freestream unit Reynolds numbers from 2×10^4 to 7.3×10^6 ft⁻¹, wall-to-edge temperature ratios of 0.4 to 0.8, and normal shock density ratios of approximately 5 (for Mach 6 and 10 air) and 12 (for Mach 6 CF₄). Global heat-transfer images using phosphor thermography of the Orbiter windward surface and the corresponding centerline and spanwise heating distributions were used to infer the state of the boundary layer (laminar, transitional, or turbulent). Transition onset (incipient¹) values identified from that database, along with predicted boundary-layer edge parameters, were used to formulate protuberance-induced transition correlations for Version 1.0 of the BLT Tool [3–5].

This reports documents a wind-tunnel experiment conducted as part of a technical expert investigation (TEI) study. TEI funding was allocated to the BLT team as a discretionary resource to support potential studies that the team deemed important with concurrence from the working group. The BLT team decided to use the resources to support ten days of testing in the 20-Inch Mach 6 Air Tunnel for a protuberance-induced transition study, herein

¹Incipient transition is defined as the first appearance of transition on the Orbiter downstream of the trip. When transition first occurs immediately downstream of the trip location, it is referred to effective transition which is not the subject of this document.

referred to as the TEI study. The measurements were acquired on 0.9%-scale Orbiter models at a nominal angle-of-attack of 40° . The larger model scale (0.9% versus 0.75%) facilitated improved manufacturing capabilities of the protuberances. The current database expands the existing Mach 6 database by acquiring data for other representative protuberance shapes (e.g., gap fillers and shapes resulting from tile repair concepts) and for protuberances at aft locations on the Orbiter. The primary objective of this study is to investigate the effects of protuberance-trip geometry and location on Shuttle Orbiter boundary-layer transition. The geometry sensitivity was done by simulating protuberance shapes that are representative of those realized in flight. This addresses the outstanding question as to whether on not protuberance shape (e.g., pizza box versus gap filler) has a first-order effect on incipient transition. The location sensitivity is twofold. Namely, the existing database is limited to protuberances located at $x/L_{ref} \leq 0.7$ and all outboard trip locations are confined to the attachment-line region. The exception to these locations is limited data measured in the 20-Inch Mach 6 Air Tunnel during STS-121 mission support that were acquired on 0.75%-scale models at a nominal angle-of-attack of 40° [10]. Data are acquired in this TEI study for $x/L_{ref} > 0.7$ and at outboard locations inboard of the shock interaction region. The secondary objective is to assess the effect of gap-filler orientation on the Orbiter boundary-layer transition. This newly acquired data will be used to help corroborate recently measured MH-13 data [11] obtained in the Calspan-University of Buffalo Research Center (CUBRC) LENS-I Shock Tunnel [12] on a 1.8%-scale Orbiter model and for the development of Version 2 of the BLT Tool.

2 Experimental Methods

2.1 Test Facility

The experimental study was performed in the NASA Langley Research Center 20-Inch Mach 6 Air Tunnel. The 20-Inch Mach 6 Air Tunnel is a blowdown facility in which heated, dried, and filtered air is used as the test gas. The tunnel has a two-dimensional, contoured nozzle that opens into a 20.5-inch by 20-inch test section. The tunnel is equipped with a bottom-mounted injection system that can transfer the model from the sheltered model box to the tunnel centerline in less than 0.5 seconds. Run times on the order of 15 minutes are possible, although for the current aeroheating study run times of only a few seconds are required. The nominal reservoir conditions of the facility are stagnation pressures of 30 to 500 psi with stagnation temperatures of 760 to 1000 °R, that very nearly produces perfect gas ($\gamma = 1.4$) freestream flows with Mach numbers between 5.8 and 6.1 and unit Reynolds numbers of 0.5×10^6 to $7.3 \times 10^6 \text{ ft}^{-1}$. An image of an Orbiter model installed in the sheltered model box of the facility is shown in Fig. 1. Recent calibration measurements in this facility [13] indicate that the test-core diameter is at least 10 inches and can be as large as 14 inches depending on the flow conditions. A schematic of a 0.9%-scale model in a 10-inch diameter flow core of the facility is shown in Fig. 2, thus illustrating that the model fits in the uniform flow core.

2.2 Test Models

The test models for this study, see Fig. 1, are cast ceramic Shuttle Orbiter models ($L_{ref} \approx 11.5$ inches long from nose to body-flap hinge) manufactured with a standard construction technique. An epoxy mold constructed from a 0.9%-scale stereo-lithography pattern of the Shuttle 2002 CAD geometry was used to fabricate the models. (See Bibb [14] for more details on the Shuttle 2002 CAD geometry.) Specifically, wax patterns created from the mold were used to cast each individual Orbiter model using a patented silica ceramic slip casting technique. The cast shells were then back-filled with a hydraulically setting silica

ceramic for strength and support of the base mounted cylindrical sting. Small ink-based identification marks (i.e., fiducial marks) were then placed on the model surface to locate the placement of the metallic dowels with attached protuberances and to assist in the alignment of the model in the tunnel. The larger scale models and metal inserts were required in order to more accurately reproduce the small-scale gap-filler trips. Finally, the models were coated with a mixture of phosphors suspended in a silica-based colloidal binder. Buck *et al.* [15] gives further details on the construction of the ceramic Orbiter models.

Seven basic model configurations were built: two baseline models (smooth OML models with no holes for trips but intended to have different levels of phosphor coating distributed roughness) and five with holes drilled perpendicular to the surface at distinct locations, as shown in Fig. 3. Models 1 and 7 are the baseline models. Model 1 has a surface roughness consistent with the other models. Hand working the model surface with soft-textured wipes is the process typically used to remove the loose phosphor particles on the surface during coating process. It is done by applying a reasonable amount of pressure between the wipe and model surface without removing most of the phosphor coating. A final coat of binder is applied to the model surface before testing. Model 7 was processed somewhat differently. The loose phosphor particles were not removed from the model surface. A final coat of the binder was applied to the model surface in preparation for testing. The surface of model 7 was hand worked slightly in the tunnel after the first run with this model to remove some of the larger particles that prematurely tripped the flow. The model surface was hand worked with a wipe by applying a few stokes so that some of the phosphor coating was lost. A folded paper was then used to lightly brush the windward surface of the model to remove any loose particles. Surface roughness measurements were acquired on both models after the completion of the test using surface profilometry, a Taylor-Hobson Form Talysurf-120L. Two measurements were obtained on the symmetry plane at $x/L_{ref} \approx 0.2$ and 0.7 and one on each wing at $(x/L_{ref}, y/L_{ref}) \approx (0.85, \pm 0.25)$ for both models. Note that the axial distance from the nosetip is represented by x and the spanwise distance from the centerline (CL) symmetry plane is y . The mean values of the four roughness averages, R_a , for model 1 and model 7 are $R_a = 177 \mu\text{-in.}$ (or root-mean-square roughness, $R_q = 220 \mu\text{-in.}$) and $R_a = 281 \mu\text{-in.}$ ($R_q = 365 \mu\text{-in.}$), respectively. Before applying the phosphor coating on models 2 - 6, holes were drilled normal to the model surfaces as indicated in Fig. 3. The center locations of the precision drilled holes are given in Table 1. Fiducial marks were placed at the location of the desired hole centers for models 2 - 6. A glove-like template was fabricated using a stereo-lithography pattern from the Shuttle CAD geometry. This fixture served as a setup guide for the drill press to insure that the holes were all normal to the local model surface. After drilling the required hole(s) in each model, the models were coated with the mixture of phosphors suspended in the binder. Final fiducial marks were placed on all the models for alignment purposes and mapping of the thermography images (locations identified in Table 2).

Fig. 4 shows the four basic trip-dowel insert configurations that were built along with pertinent dimensions. All the trip configurations consisted of an external dowel (simply referred to herein as dowel) in conjunction with either shim stock or an interior dowel. The dowel assemblies, which are placed into the drilled holes within the ceramic, were cut from precision drill rods. The bottom end of each dowel was bevelled for easy placement into the models and the top end ground flat. For the dowels with slots, electrical discharge machining (EDM) was used to generate the slots. The shim stock pieces, which were used to simulate the protuberances, were cut using EDM or laser ablation depending on the thickness of the shim stock. The “pizza-box” (**PB**) trips represent the previous database that utilized adhesively backed Teflon trips on 0.75%-scale models [6]. The pizza-box trips for the 0.9%-scaled models were sized at $0.060''$ by $0.060''$ as opposed to the $0.050''$ by $0.050''$ size used for the 0.75%-scale models. The “rounded pizza-box” (**RPB**) trip was selected to identify if any first-order effects can be attributed to the sharp trip corner geometry. The “hemisphere”

(H) trip was selected to identify if the existing database provides any conservatism with regard to repair scenarios, e.g., STA-54 repairs. The hemisphere trips were manufactured using two dowels where one interior dowel with a rounded top was inserted into a reamed hole in the dowel. Lastly, the “gap-filler” trip, identified as either a fence (F) or an angled fence (AF), was selected to investigate any differences between the existing ground-based data and the typical flight-type protuberances. For the pizza-box and rounded pizza-box trips, shim stock of different thicknesses was used to provide the trip height variation, k . For the fence trips, shim stock cut with dimensions of $0.060'' \times H$ (H is dimension normal to dowel), as shown in Fig. 4, were used to provide k -variation of the trips. These trip configurations were completed with the use of a high-temperature adhesive (Loctite 498 Super Bonder) to secure the assembly and to fill in any exposed gaps. A photograph of four typical trip configurations are shown in Fig. 5 for completeness. The photograph clearly demonstrates the small scale of the trip-dowel assemblies relative to a dime. Table 3 shows types and quantities of protuberances manufactured. The trip heights, k , in the table are the designed values. The as-built heights will be given later in the document.

To secure the dowel inserts into the model, a neodymium magnet was secured to the bottom of the precision-drilled holes, as depicted in Fig. 6. Blank dowels were used to fit check all holes to insure proper match to the model OML. Individual adjustment with each hole could be made by stacking 0.001-in. thick shim stock or 0.003-in. thick double-sided tape as needed. Once the hole fit check was complete, the blank dowels were also used during the test to verify the integrity of the overall fit by acquiring untripped data for comparison to the baseline models without holes. The uncertainty of the trip heights was estimated to be ± 0.0005 -in. for all trips. To remove the trip assemblies from the models, a series of larger magnets were used to extract the dowels/trip assemblies from the drilled holes in the models.

2.3 Test Instrumentation

Two-color, relative intensity, phosphor thermography was used to measure global temperature to infer the global surface heating distributions on the windward surface of the Orbiter models [16] - [19]. This technique uses a mixture of phosphors that, when illuminated with ultraviolet light, fluoresce across regions of the visible spectrum, of which the red and green wave bands are used. The intensity of the fluorescence is dependent on the amount of incident ultraviolet light and the local surface temperature of the phosphor. This phosphor mixture (batch #12² used for this test), which is suspended in a silica ceramic binder and applied with an air brush, is used to coat the slip cast silica ceramic models. The final coating thickness is approximately 0.001 inches. Using a 3-CCD (Charge Coupled Device) camera, fluorescence intensity images of an illuminated phosphor model exposed to the hypersonic stream are acquired and converted to temperature mappings via a temperature-intensity calibration. The temperature calibration uses the ratio of the red and green components of the image to construct a lookup table which converts the intensities to temperature values. Currently, this calibration, done prior to the test, is valid over a temperature range from 532 to 800 °R. The temperature data from the time-sequenced images taken during a wind-tunnel run is then reduced to heat-transfer rate at every pixel on the image (and hence globally on the model) using a heat-transfer rate calculation assuming one-dimensional semi-infinite slab heat conduction [19]. An illustration of the phosphor thermography acquisition system is shown in Fig. 7.

There are two main advantages of this technique over conventional transient thin-skin

²Batch #12 is given here for completeness. The different batch numbers represent differences in the preparations of the phosphor coatings used for testing in global phosphor thermography. Some discussion on the temporal collapse of the heating distributions on Orbiter models using batches #10, 11, and 12 are given in Ref. [20].

calorimeter and thin-film resistance methods. The first is the global resolution of temperature/heating data that provides the detailed information of specific flow features. Surface heating is determined in a global sense; at every point on the model surface within view of the camera and at various times during the run. Secondly, the model fabrication method used produces a coating that does not require re-application between runs, thereby significantly enhancing the efficiency of the phosphor technique. In addition, the slip-casting model fabrication method is a rapid process whereby, in three to four weeks, a full array of inexpensive models can be fabricated, complete with various perturbations needed for a configuration build-up scheme such as variable nose radii and control flap deflections.

Flow condition data were acquired using a 16-bit analog-to-digital facility acquisition system. The values of the measured uncertainties for the stagnation pressure, P_t , and stagnation temperature, T_t , are estimated to be ± 0.4 psia and ± 2.12 °R, respectively [13]. The uncertainties in the angle-of-attack of the model are estimated to be $\pm 0.2\%$. The heating measurements from the phosphor technique have been estimated to be accurate to within $\pm 15\%$ [21]. It should be noted, however, that absolute heating measurements are not required for determining transition onset as this is determined by departure of the measured non-laminar heating level from a baseline undisturbed laminar value. Run-to-run repeatability of the heating data for a given model was better than $\pm 4\%$.

2.4 Data Analysis

For each model, global aeroheating image data were acquired over a range of freestream unit Reynolds numbers. Transition onset for each model configuration was then inferred from the corresponding line cuts of the aeroheating image data (centerline cuts and spanwise cuts at different streamwise stations). Line-cut data were extracted from the aeroheating images with the IHEAT software package [21]. The results are presented in terms of a non-dimensional heat-transfer coefficient ratio h/h_{FR} , where h_{FR} is the theoretical stagnation point heat-transfer coefficient for a 0.108-in. radius sphere (the nose radius of a 0.9%-scale Orbiter model) computed using the method of Fay-Riddell [22] for a wall temperature of 540 °R. A departure in the normalized mean heat-transfer rate from the laminar baseline was used as the basis with which to develop the transition criterion. Throughout this document, an estimate of the incipient transition unit Reynolds number, Re_{inc} , is defined as the average unit Reynolds number between the last fully laminar condition ($Re_{\infty,1}$) and the first condition with evidence of laminar departure ($Re_{\infty,2}$), where $Re_{\infty} = \rho_{\infty} u_{\infty} / \mu_{\infty}$. This basis for defining the incipient conditions will be used throughout this document. For the freestream unit Reynolds number increments tested, we were able to identify transition onset to within $\pm 10\%$ (i.e., $\pm 5\%$ uncertainty in the transition parameter, Re_{θ}/M_e).

The BLT Tool v.1 was developed using incipient transition data acquired in the Langley 20-Inch Mach 6 Tunnel and a few historical flight data. Incipient transition is defined as the first evidence of laminar-to-turbulent transition on the windward surface of the Orbiter. The generalized correlation approach used in this report follows the work summarized in Ref. [23]. The equation of generalized correlation has the form $Y_{tr} = CX_{tr}^n$, where X_{tr} is the disturbance parameter and Y_{tr} the transition parameter. A line plot represented by this equation delineates a *best estimate* boundary for the correlation such that data below the line denote laminar flow and data above denote turbulent flow. For small disturbance parameters, the transition parameter should asymptote to a smooth-wall limit, which is facility dependent. Similarly, for large disturbance parameters, the transition parameter asymptotes to a limiting lower value – a *protuberance limit* or a *lower threshold limit*³. The current tool [3, 4] assigns as the disturbance parameter k/δ where k is the protuberance

³The protuberance limit implies that further increases in roughness height k has no additional effect on transition and the lower threshold limit implies that the unit Reynolds number is too low to produce and/or maintain the turbulence.

height and δ the boundary-layer thickness and the transition parameter as Re_θ/M_e where $Re_\theta (= \rho_e u_e \theta / \mu_e)$ and M_e are the momentum thickness Reynolds number and boundary-layer edge Mach number, respectively. The curve coefficient, $C = 27$, was selected using a 95% confidence level, such that statistically 95% of the incipient transition data lie above the correlation curve, which introduces some conservatism into the tool. Note that data obtained in the 20-Inch Mach 6 CF_4 Tunnel and the 31-Inch Mach 10 Air Tunnel were not used in the correlation to evaluate the value of C . The BLT Tool v.1 is expressed as

$$\frac{Re_\theta}{M_e} \times \frac{k}{\delta} = C \quad (1)$$

where the power of $n = -1$ represents a straight line at -45° in log-log space.

The flow properties used in the development of the BLT Tool v.1 were derived from an engineering code called LATCH [5], which utilized a two-layer engineering approach [24] with inviscid LAURA solutions. The flow properties captured with LATCH are limited to boundary-layer edge properties and wall conditions. The flow solutions were all computed for 0.75%-scale Orbiter models but the current transition measurements were acquired on 0.9%-scale Orbiter models. As both models are geometrically similar and exposed to the same freestream and wall temperature conditions, the solutions for the 0.75%-scale models were transformed to obtain 0.9%-scale model solutions in lieu of recomputing the flow properties using LATCH for the 0.9%-scale models. The analysis was done where all flow properties were transformed at a given freestream unit Reynolds number, Re_∞ , and prescribed surface location, \vec{X}/L_{ref} , for both model scales, i.e.,

$$Re_\infty = Re_\infty \Big|_{0.9\%} = Re_\infty \Big|_{0.75\%} \quad (2)$$

and

$$\vec{X}/L_{ref} = (x/L_{ref}, y/L_{ref})_{0.9\%} = (x/L_{ref}, y/L_{ref})_{0.75\%}. \quad (3)$$

Inviscid flow similarity exists for a given freestream condition (assumes weak inviscid/viscid interaction), such that edge flow properties are the same, i.e.,

$$\left\{ M_e, T_e, P_e, \vec{u}_e, \rho_e, \dots \right\}_{0.9\%} = \left\{ M_e, T_e, P_e, \vec{u}_e, \rho_e, \dots \right\}_{0.75\%}. \quad (4)$$

Based on local boundary-layer similarity, the boundary-layer thickness, $\delta(\vec{X}/L_{ref}, Re_\infty)$, is assumed proportional to $\sqrt{X/Re_e}$ where $Re_e = \rho_e u_e / \mu_e$. For the two different model scales of interest, this leads to

$$\frac{\sqrt{X}}{\delta(\vec{X}/L_{ref}, Re_\infty)} \Big|_{0.9\%} = \frac{\sqrt{X}}{\delta(\vec{X}/L_{ref}, Re_\infty)} \Big|_{0.75\%} \quad (5)$$

since the edge unit Reynolds numbers, Re_e , are equal per Eq. 4. Utilizing Eq. 3, this is rearranged to give

$$\frac{\delta(\vec{X}/L_{ref}, Re_\infty) \Big|_{0.9\%}}{\delta(\vec{X}/L_{ref}, Re_\infty) \Big|_{0.75\%}} = \sqrt{\frac{X_{0.9\%}}{X_{0.75\%}}} = \sqrt{\frac{L_{0.9\%}}{L_{0.75\%}}} = 1.095. \quad (6)$$

The displacement thickness, $\delta^*(\vec{X}/L_{ref}, Re_\infty)$, and momentum thickness, $\theta(\vec{X}/L_{ref}, Re_\infty)$, are given by a similar expression, namely

$$\left\{ \delta_{0.9\%}, \delta_{0.9\%}^*, \theta_{0.9\%} \right\} = \left(\sqrt{\frac{L_{0.9\%}}{L_{0.75\%}}} \right) \left\{ \delta_{0.75\%}, \delta_{0.75\%}^*, \theta_{0.75\%} \right\}. \quad (7)$$

Applying Eqs. 4 and 7, the scaling for the momentum thickness Reynolds numbers is

$$Re_\theta \Big|_{0.9\%} = \frac{\theta_{0.9\%}}{\theta_{0.75\%}} \times Re_\theta \Big|_{0.75\%} = \left(\sqrt{\frac{L_{0.9\%}}{L_{0.75\%}}} \right) \times Re_\theta \Big|_{0.75\%}. \quad (8)$$

The flow properties on the 0.9%-scale model required for the BLT Tool v.1 were obtained by first probing the LATCH database for the properties on the 0.75%-scale model at the desired Re_∞ and \bar{X}/L_{ref} . The disturbance (k/δ) and transition (Re_θ/M_e) parameters were then computed using Eqs. 4, 7 and 8.

2.5 Test Matrix and Tunnel Conditions

The proposed test plan of Test 6922 in the 20-Inch Mach 6 Tunnel for the tripped configurations is shown in Table 4. Twelve tripped configurations were proposed between the five models (models 2 - 6). The proposed plan included the effects of protuberance shape, orientation, and location. A concise objective for each configuration is given in the table. Note that ‘shape effect data’ implies both protuberance shape and orientation effects. The designed incipient unit Reynolds numbers, Re_{inc} , were derived using the BLT Tool v.1 (Eq. 1) with database computed from LATCH. A total of five runs were budgeted for each configuration. Two Reynolds numbers below the predicted incipient value and two above were targeted in an attempt to bracket the actual incipient value. A maximum change of 20% was selected between adjacent Reynolds number values. In addition to the proposed runs noted in Table 4, test runs were planned for the two baseline models (1 and 7) and for each of the configuration models with blank dowels installed.

Some difficulty was experienced in trying to bracket the incipient Reynolds number values at the designed incipient lower Reynolds number values ($\sim 0.6 \times 10^6/\text{ft}$) due to lower Reynolds number limits of the facility and the inability to extract the test section flow conditions at these low Reynolds numbers using the current process (GASPROPS code [25]). The test plan was therefore changed in real time and the run matrix as completed is presented in Table 5. Thirteen tripped and untripped configurations were tested and resulted in a total of 121 runs during the test entry. For all runs, the model angle-of-attack was set to 40 degrees. The yaw angle, body-flap angle, and aileron angle were fixed at 0 degrees. The test section flow conditions presented in the tables were computed using the GASPROPS code with the measured reservoir stagnation pressure P_t , stagnation temperature T_t , and pitot pressure calibrations of the facility as inputs. The targeted Reynolds numbers were computed using GASPROPS code by providing the pertinent tunnel conditions. Generally, aeroheating image data were acquired for each model at four to nine different values of freestream unit Reynolds number. Additional runs, more than the proposed five, were typically required to ensure that the model was set to zero sideslip and to provide sufficient resolution for measuring incipient Reynolds numbers.

3 Results and Discussion

For each Orbiter model configuration, a series of results are presented in the form of a photograph of the model windward surface (includes close-up images as necessary), global aeroheating image data for the different freestream unit Reynolds numbers, and line cuts (centerline and streamwise) of the aeroheating image data. The photographs were all taken with the models installed in the tunnel but retracted in the sheltered model box position. The aeroheating image data are shown as colormaps of the normalized heat-transfer coefficient, h/h_{FR} . Test run numbers and the corresponding unit Reynolds numbers are included with the images for reference. A sketch of the windward surface depicting the trip type,

orientation and location are also included with the aeroheating image data. The line cuts of the aeroheating data were found to be more objective than relying on the colormaps of the global aeroheating image data to detect the onset of transition. For the runs with a centerline protuberance, the centerline line cuts over the Reynolds number range are used to detect laminar departure of h/h_{FR} as a result of that trip. To detect laminar departure resulting from off-centerline protuberances, a series of spanwise line cuts, typically at $x/L_{ref} = 0.8$ or 0.9 , are plotted for the range of Reynolds numbers tested. The incipient unit Reynolds number, Re_{inc} , for each of the thirteen model configurations with trips are presented in Table 6. The unit Reynolds numbers of the last fully laminar value, $Re_{\infty,1}$, and the first evidence of laminar departure, $Re_{\infty,2}$, along with the LATCH derived disturbance and transition parameters are also noted in the table. The trip heights, k , in this table are the as-built heights. All the measured test data are presented below in the form of figures and tables. The plots of all the test data and accompanying photographs are presented in Figs. 8 - 90 in chronological run order. For the sake of brevity, only a few key configurations are discussed to illustrate the process by which Table 6 was populated.

3.1 Untripped Data

The first set of runs were conducted with baseline model 1 to verify consistency with data acquired on 0.75%-scale models. A photograph showing the windward surface of the model is presented in Fig. 8. The corresponding global aeroheating image data and line cuts are given in Figs. 9 - 11. The resulting heating patterns are fairly symmetric, including the transition front movement in the center region as evident from the elevated heat-transfer rates. These trends are consistent with earlier measurements on the 0.75%-scale models [6]. The other smooth OML model 7 with the rougher phosphor coating is shown in Fig. 74. Recall that the surface of models 1 and 7 were intentionally processed differently to achieve different distributed roughness. The resulting aeroheating patterns observed in Fig. 75 are fairly symmetric except for runs 103 and 99. The heating on the starboard wing is more intense than that on the port wing. Similar trends are seen in the line cut data presented in Figs. 76 and 77. The presence of an unintentional isolated roughness, likely a clump of phosphor particles, is observed in the form of elevated heating in the spanwise line cuts on the port side of the model ($y/L_{ref} \approx 0.05$).

A comparison of the global aeroheating images at similar unit Reynolds numbers between both baseline models (1 and 7) is shown in Fig. 78. Differences in the transition locations due to the distributed roughness are evident in this figure and the trends are consistent with expectations, i.e., transition occurs earlier for the surface with the larger distributed roughness. Recall from the discussion in Section 2.2 that four surface roughness measurements were obtained on both models, two on the symmetry plane and one on each wing. The mean values of the four roughness averages, R_a , for model 1 and model 7 are $R_a = 177 \mu\text{-in.}$ (or root-mean-square roughness, $R_q = 220 \mu\text{-in.}$) and $R_a = 281 \mu\text{-in.}$ ($R_q = 365 \mu\text{-in.}$), respectively. The streamwise line cuts of the heating data corresponding to Fig. 78 are shown in Fig. 79 (note that run 3 data are included for comparison). Transition onset on the symmetry plane for both runs 3 ($Re_{\infty} \approx 5.45 \times 10^6/\text{ft}$) and 99 ($Re_{\infty} \approx 3.78 \times 10^6/\text{ft}$) occurred at $x/L_{ref} \approx 0.57$. The transition Reynolds number, based on freestream conditions and the centerline distance from the model leading edge to the transition onset location, for model 1 (run 3) is $Re_{\infty,tr} \approx 3.0 \times 10^6$ and for model 7 (run 99) is $Re_{\infty} \approx 2.1 \times 10^6$. The transition parameters for models 1 and 7 are $Re_{\theta}/M_e \approx 295$ and 245 , respectively. The corresponding k/δ ($= R_a/\delta$) values for distributed roughnesses at $x/L_{ref} \approx 0.57$ of models 1 and 7 are $k/\delta \approx 0.012$ and 0.018 , respectively. These k/δ values are based on mean values of the symmetry plane roughness averages. These mean values for models 1 and 7 are $R_a = 156 \mu\text{-in.}$ ($R_q = 193 \mu\text{-in.}$) and $R_a = 284 \mu\text{-in.}$ ($R_q = 361 \mu\text{-in.}$), respectively. The k/δ values for the distributed surface roughness are more than an order

of magnitude smaller than those for the isolated three-dimensional roughnesses used in this study. The corresponding Re_k ($= \rho_k u_k k / \mu_k$) values at incipient transition locations for the distributed roughnesses are order one (based on Navier-Stokes solution database) and are not believed to have adverse effects on the discrete roughness results which have Re_k values two orders of magnitude larger than the distributed results.

3.2 Tripped Data

Before tripped configurations were tested, blank dowels (no trips bonded to dowels) were installed in each model to verify the integrity of the fit, i.e., to insure the dowel/hole combinations do not prematurely trip the downstream flow. This was generally done for Reynolds numbers up to at least twice the designed incipient values. In most cases, the phosphor coatings were chipped around the holes as a result of the constant insertion and removal of the trip assemblies. To mitigate any adverse effects of the chipped coatings with respect to premature transition, dental plaster was generally used to fill the chipped areas when the amount of lost coating became significant. In the close up photographs, the areas around the holes that were filled with dental plaster appear white in the images. A close-up photograph and aeroheating data for model 2 (trip located on centerline at $x/L_{ref} = 0.1$) with a blank dowel inserted are shown in Figs. 12 - 14. Note that blank dowels are denoted by red x's in the model sketches (see Fig. 12). The aeroheating line cuts also include data from baseline model 1 (denoted M1 in the plot legend) for comparison at a comparable Reynolds number. Also compare the run 6 colormap image imbedded in Fig. 13 to the run 1 image in Fig. 9. The resulting heating results are nearly identical to model 1 up to $Re_\infty = 2.08 \times 10^6$ /ft, which is twice the designed incipient Reynolds number for the trip configurations with model 2. Next, consider configuration 2 (see Table 6) where a fence (F) trip with height $k = 0.008''$ was installed in model 2. The associated close-up photograph and aeroheating data are given in Figs. 19 - 22. The orientation of the trip is clearly illustrated in the Fig. 20 where the trailing edge of the fence points towards the starboard (STB) side of the Orbiter. Positive angle notations used in the figures and tables indicate a clockwise rotation of the trip relative to the model centerline. The heating patterns resulting from the trip are slightly asymmetric, perhaps due to the asymmetry of the fence trip. The run 16 image and line cuts clearly show an increase in heating downstream of the trip from the observed laminar values of runs 17 and 19. The expected incipient value derived from the BLT Tool v.1 was $Re_\infty \approx 1.0 \times 10^6$ /ft, while the resulting incipient value from the current data based on the average approach is $Re_{inc} = 0.685 \times 10^6$ /ft, i.e., the average Re_∞ of runs 17 and 16. Therefore, the BLT Tool v.1 predicts later incipient transition than realized in the test implying that the tool is nonconservative for this configuration. It is important to recall that the tool was designed to be conservative (95% confidence limit) for the existing database.

Next, consider configuration 3 with three trips located at $x/L = 0.5$ on model 3. A close-up photograph showing all three trips and a table with trip types and locations are given in Fig. 30. The outboard trips were intended to be on the attachment lines. The aeroheating data and line cuts are shown in Figs. 31 - 33. The resulting heating patterns are fairly symmetric. The run 41 image shows a slight increase in heating downstream of the centerline trip. The resulting incipient value from the centerline fence trip is $Re_{inc} = 1.14 \times 10^6$ /ft based on the line cuts in Figs. 32 and 33. The freestream unit Reynolds number was increased to about three times the designed incipient value and no elevated heating resulting from the attachment-line trips (PB and H) was observed downstream. The attachment-line trips are postulated to be too far outboard such that the resulting disturbances are being swept to the leeside of the Orbiter model. This was observed for all of the configurations tested with model 3; consequently, we were unable to acquire off-centerline incipient transition data for the model 3 configurations. It should be noted that attachment-line data were acquired in

the previous test at Mach 6 on the 0.75%-scale models at this forebody location [6]. There is a minor difference in the tabulated trip locations noted in this study and those noted in Ref. [6]. For the current study, the trip locations are based on the centroidal locations of the trips, i.e., the hole centers. In the previous study [6], the pizza-box trips were located based on the upstream vertex of the trips. It is plausible that the upstream placement of the trips by one half the trip length in the current study relative to the previous study is partly responsible for this inconsistency.

The photograph and aeroheating data for configuration 6A on model 4 are presented in Figs. 44 - 47. Three trips are located at $x/L_{ref} = 0.7$ for this configuration, one on the centerline and two outboard (see table imbedded in Fig. 44). The outboard trips for model 4 were intended to be inboard of the attachment lines. The heating patterns in the global aerothermal images for configuration 6A are fairly symmetric. The run 56 image and line cuts show a slight increase in heating downstream of the centerline trip. The resulting incipient value from the centerline fence trip is $Re_{inc} = 0.945 \times 10^6/\text{ft}$. The outboard trips are clearly inboard of the attachment lines and are evident in the images, as the disturbance wedges are being swept nearly directly aft. Elevated heating due to the port side trip is first evident in the aeroheating data of run 58 (see line cuts). The resulting incipient data from this port side pizza-box trip is $Re_{inc} = 0.765 \times 10^6/\text{ft}$. Similarly, elevated heating due to the starboard side trip is first evident in run 60. The resulting incipient value from the starboard side hemisphere trip is $Re_{inc} = 1.65 \times 10^6/\text{ft}$. Clearly, the pizza-box trip is more effective than the hemisphere trip for this outboard trip location.

Consider configuration 6C on model 4. The photograph and heating data are shown in Figs. 52 - 55. The centerline and starboard trips are a fence and an angled fence, respectively, oriented parallel to the model centerline (see sketch in Fig. 53). The port trip is a pizza-box trip where the diagonal line from the upstream vertex makes approximately a -22.5° angle relative to the model centerline (negative value implies a counterclockwise rotation). The resulting heating patterns are fairly symmetric. The run 72 image and line cuts show an increase in heating downstream of the centerline fence trip. The resulting incipient value from the centerline fence trip is $Re_{inc} = 2.40 \times 10^6/\text{ft}$ compared to the designed value of $Re_\infty \approx 1.0 \times 10^6/\text{ft}$. As anticipated, the BLT Tool v.1 is very conservative for the centerline fence trip due to the orientation of the fence. Per line cuts in Fig. 55, the resulting incipient data from the port pizza-box trip is $Re_{inc} = 0.97 \times 10^6/\text{ft}$ which is within the experimental uncertainty of the design value. The starboard incipient data for the angled fence appeared to be contaminated by a mismatch between the dowel and the OML due to significant coating lost around the edge of the hole; consequently, no transition resulting from the starboard trip data was acquired for this configuration.

Data are presented here for configuration 8 on model 5 where three trips are located at $x/L_{ref} = 0.74$. The two outboard trips for model 5 were intended to be located just inboard of the attachment lines. The trips are a fence trip at $+45^\circ$, a fence trip at -45° and a pizza-box trip on the model centerline, port side and starboard side, respectively. A close-up photograph and table with pertinent trip information are given in Fig. 83. The designed incipient Reynolds number for configuration 8 is $Re_\infty \approx 0.6 \times 10^6/\text{ft}$. As is evident in Figs. 84 - 86, the run 109 image and line cuts show an increase in heating downstream of the centerline fence trip. The resulting incipient Reynolds number from the centerline fence trip is $Re_{inc} = 1.0 \times 10^6/\text{ft}$. The attachment line trips appear to be near the attachment line, as designed, since the disturbance wedges stay near to the wing leading edge. Increased heating downstream of the port fence trip is first observed in run 111 (see spanwise line cuts in Fig. 86), resulting in an incipient value on the port side of $Re_{inc} = 0.505 \times 10^6/\text{ft}$. Note that the orientation of the port fence trip is nearly aligned with the wing leading edge implying that the fence is in the general direction of the inviscid edge flow. One might assume that due to the small relative angle of the fence to the local edge streamlines this orientation may be somewhat less effective at promoting boundary-layer transition, but the

data do not support that conclusion. In the outboard regions, there is crossflow generated by spanwise gradients that leads to flow angularity between the incoming boundary-layer flow and the fence. This is in contrast to the centerline trip in configuration 6C discussed earlier where there is no crossflow on the model centerline. Increased heating downstream of the starboard pizza-box trip is first seen in run 113 and the resulting incipient value is $Re_{inc} = 0.665 \times 10^6/\text{ft}$ which is consistent with the designed value. The port fence trip is more effective than the starboard pizza-box trip for this configuration as demonstrated by the lower Re_{inc} and k values for the port fence trip.

Consider configuration 8A on model 5 shown in Fig. 87 where three trips are located at $x/L_{ref} = 0.74$. The trips are a pizza-box trip, a fence trip at $+45^\circ$ and an angled fenced trip at -45° on the model centerline, port side and starboard side, respectively. Note that pertinent trip information is imbedded in the table of the figure. The global images and line cuts are given in Figs. 88 - 90. The resulting heating patterns are symmetric. The run 115 image and line cuts show a slight increase in heating downstream of the centerline pizza-box trip resulting in an incipient value of $Re_{inc} = 1.0 \times 10^6/\text{ft}$. The port fence trip orientation for this configuration was achieved by simply rotating the fence in configuration 8 by 90° . Evidence of elevated heating due to the port fence trip is first apparent in run 118, corresponding to $Re_{inc} = 0.86 \times 10^6/\text{ft}$. Note that the port fence trip with the orientation in configuration 8 (nearly aligned to the wing leading edge) is more effective than the fence trip in configuration 8A (oriented nearly perpendicular to the wing leading edge). This observation was somewhat counter intuitive to our expectations based solely on the relative alignment of the edge flow and fence trip. Similarly, the resulting incipient value from the starboard angled fence is $Re_{inc} = 1.36 \times 10^6/\text{ft}$.

This concludes the brief discussion overview of the configurations tested, with and without protuberances. The incipient transition data resulting from discrete protuberances are tabulated in Table 6. These results are plotted in Fig. 91 along with the previous Mach 6 data in the BLT Tool v.1 correlation space. It should be noted that the existing data presented in the figure are a slight variation from those used to develop the BLT Tool v.1 correlation [3, 4]. The incipient values used to develop Version 1 of the BLT Tool were generally defined as the first value of laminar departure versus the average approach used for this analysis. However, with this change in the definition of the incipient values, both approaches were found to be consistent. The transition and disturbance parameters given in Table 6 are based on the LATCH database. The experimental correlation constant, C , for each configuration is also given in the table. For all except two values (shown as bold in the table), the BLT Tool v.1 with $C = 27$ is conservative as designed. The two non-conservative configurations happen to be fences oriented at 45 degrees relative to the model centerline at x/L_{ref} locations of 0.1 and 0.74. The tool was most conservative ($C = 74$) for a fence aligned with the flow on the model centerline at $x/L_{ref} = 0.70$. In the correlation plot presented in Fig. 91, the TEI data demonstrate more scatter than the existing Mach 6 data. This increased scatter is expected since the TEI data includes the effects of protuberance shape and orientation on transition onset not captured within the previous Version 1 dataset [6].

4 Summary

This report documents the TEI wind-tunnel test on 0.9%-scale Shuttle Orbiter models in the Langley 20-Inch Mach 6 Tunnel. The uses of this experimental database are to assess the applicability of the BLT Tool v.1 for different protrusion shapes and to ultimately develop a more comprehensive version of the BLT Tool to include all of the available ground-based and flight data. Phosphor thermography was used to measure the global aeroheating on the windward surface of the Orbiter models in order to distinguish laminar and/or turbulent

heating. A Reynolds-number sweep was performed to identify boundary-layer transition onset for each model configuration. Transition sensitivity to various protuberance types, more representative of realistic trips, were examined to establish if the BLT Tool v.1 is still conservative for protuberances other than the pizza-box trips. The protuberance types include pizza-box, rounded pizza-box, fence, angled fence, and hemisphere trips with heights in the range of $0.006'' \leq k \leq 0.011''$ ($0.22 < k/\delta < 0.52$) at axial locations in the range of $0.10 \leq x/L_{ref} \leq 0.85$. The effect of distributed roughness on a secondary baseline model with surface roughness larger than the primary baseline model with nominal surface roughness was examined. The results clearly demonstrate earlier transition onset on the acreage region of windward surface for the model with the larger surface roughness ($\sim 1/3$ reduction in $Re_{\infty, tr}$). The mean values of the measured roughness averages along the model symmetry plane for the primary and secondary baseline models are $R_a = 156 \mu\text{-in.}$ and $R_a = 284 \mu\text{-in.}$, respectively.

The protuberance test results are summarized in Table 6 and presented in Fig. 91. Some general observations from this study are highlighted below.

- Some protuberance geometry effects were observed for fence and pizza-box trips. Within experimental uncertainty, fence trips oriented at $\pm 45^\circ$ appear more effective than pizza-box and hemisphere trips for a given trip height, k , and model location. Hemisphere protuberances are the least destabilizing trips tested in the nominal orientations, i.e., fences at $\pm 45^\circ$ and pizza boxes with diagonals parallel to the model centerline.
- Pizza-box trips appear more effective in the traditional orientation (diagonal from upstream vertex parallel to model centerline) at the outboard locations for $x/L_{ref} = 0.70$ than for the other orientations tested.
- Fence trips on the Orbiter centerline appear to be most effective for transition onset at orientations of $\pm 45^\circ$, least effective at 0° , and have an intermediate effectiveness at 90° . The fence trip oriented at 0° on the model centerline is the least destabilizing trip configuration tested.
- Fences aligned almost parallel to the wing leading edge near the attachment line are very effective. Care must be taken not to falsely assume that outboard gap fillers are ineffective if they are closely aligned with the wing leading edge.
- Fences approximately normal to the wing leading edge are less effective than fences nearly parallel to wing leading edge. This may seem somewhat counter intuitive.
- At $x/L_{ref} = 0.85$, the BLT Tool v.1 is measurably conservative for the protuberance types tested (pizza-box, rounded pizza-box, and fence trips). This result may be significant as it implies that the tool may predict early transition for protuberances at aft locations on the Orbiter.
- BLT Tool v.1 is conservative for all newly acquired incipient data except for two data points with fence trips at $x/L_{ref} = 0.10$ on the centerline and at $x/L_{ref} = 0.74$ near the attachment line (fence nearly parallel to the wing leading edge).
- Shape effects and orientation effects are mostly confined to the scatter in the existing Mach 6 data, i.e., no significant first-order effects with protuberance type are apparent in the existing Version 1 of the BLT Tool.

References

1. Columbia Accident Investigation Board Final Reports, Vol. I-VI [online resource], URL: <http://caib.nasa.gov/> [cited August and October 2003].
2. Campbell, C. H., Anderson, B., Bourland, G., Bouslog, S., Cassady, A., Horvath, T. J., Berry, S. A., Gnoffo, P. A., Wood, W. A., Reuther, J. J., Driver, D. M., Chao, D. C., Hyatt, J., and Picetti, D., "Orbiter Return To Flight Entry Aeroheating," AIAA Paper 2006-2917, June 2006.
3. Berry, S. A., Horvath, T. J., Green, F. A., Kinder, G. R., and Wang, K. C., "Overview of Boundary Layer Transition Research in Support of Orbiter Return To Flight," AIAA Paper 2006-2918, June 2006.
4. Horvath, T. J., Berry, S. A., Merski, N. R., Berger, K. T., Buck, G. M., Liechty, D. S., and Schneider, S. P., "Shuttle Damage/Repair from the Perspective of Hypersonic Boundary Layer Transition - Experimental Results," AIAA Paper 2006-2919, June 2006.
5. Greene, F. A. and Hamilton, H. H., "Development of a Boundary Layer Properties Interpolation Tool in Support of Orbiter Return to Flight," AIAA Paper 2006-2920, June 2006.
6. Liechty, D. S., Berry, S. A., and Horvath, T. J., "Shuttle Return To Flight Experimental Results: Protuberance Effects on Boundary Layer Transition," NASA TM-2006-214306, May 2006.
7. Liechty, D. S., Horvath, T. J., and Berry, S. A., "Shuttle Return to Flight Experimental Results: Cavity Effects on Boundary Layer Transition," NASA TM-2006-214305, May 2006.
8. McGinley, C. B., Berry, S. A., Kinder, G. R., Barnwell, M., Wang, K. C., and Kirk, S. K., "Review of Orbiter Flight Boundary Layer Transition Data," AIAA Paper 2006-2921, June 2006.
9. Miller, C. G., "Hypersonic Aerodynamic/Aerthermodynamic Testing Capabilities at Langley Research Center," AIAA Paper 1992-3937, July 1992.
10. Kegerise, M. A., King, R. A., and Berry, S. A., "Wind Tunnel Test in Support of STS-121: Protuberance Effects on Boundary-Layer Transition," NASA JSC EG-SS-07-06, 2007.
11. Cassady, A. M., Bourland, G., King, R. A., Kegerise, M. A., Marichalar, J., Kirk, B. S., and Treviño, L., "MH-13 Space Shuttle Orbiter Aerothermodynamic Test Report," NASA TP-2007-214758, 2007.
12. AAEC Research Staff, LENS Brochure, *Capabilities and Technologies*, Buffalo, NY 2004.
13. Rhode, M. N., and DeLoach R., "Hypersonic Wind Tunnel Calibration Using the Modern Design of Experiments," AIAA Paper 2005-4274, July 2005.
14. Bibb, K. L., "2002 Shuttle Orbiter CAD Geometry, as used in Support of the Columbia Accident Investigation and Return-to-Flight," NASA JSC Orbiter Entry Aeroheating Note OEAN-0305-005.

15. Buck, G. M., Powers, M. A., Griffith, M. S., Hopkins, J. W., Veneris, P. H., and Kuykendoll, K. A., "Fabrication of 0.0075-Scale Orbiter Phosphor Thermography Test Models for Shuttle RTF Aeroheating Studies," NASA TM-2006-214507, November 2006.
16. Buck, G. M., "Automated Thermal Mapping Techniques Using Chromatic Image Analysis," NASA TM-101554, April 1989.
17. Buck, G. M., "Surface Temperature/Heat Transfer Measurement Using a Quantitative Phosphor Thermography System," AIAA Paper 91-0064, January 1991.
18. Merski, N. R., "A Relative-Intensity, Two-Color Phosphor Thermography System," NASA TM-104123, September 1991.
19. Merski, N. R., "Global Aeroheating Wind-Tunnel Measurements Using Improved Two-Color Phosphor Thermography Method," *Journal of Spacecraft and Rockets*, Vol. 36, No. 2, 1999, pp. 160-170.
20. Kegerise, M. A., King, R. A., and Berry, S. A., "Cavity Effects on Space Shuttle Orbiter Boundary-Layer Transition," NASA TM-2008-215113, March 2008.
21. Merski, N. R., "Reduction and Analysis of Phosphor Thermography Data with IHEAT Software Package," AIAA Paper 98-0712, January 1998.
22. Fay, J. A., and Riddell, F. R. "Theory of Stagnation Point Heat Transfer in Dissociated Air," *Journal of the Aeronautical Sciences*, Vol. 25, No. 2, 1958, pp. 73-85.
23. Reda, D. C., "Review and Synthesis of Roughness-Dominated Transition Correlations for Reentry Applications," *Journal of Spacecraft and Rockets*, Vol. 39, No. 2, 2002, pp. 161-167.
24. Hamilton, H. H., DeJarnette, F. R., and Weilmuenster, K. J. "Applications of Axisymmetric Analog for Calculating Heating in Three-Dimensional Flows," *Journal of the Spacecraft and Rockets*, Vol. 24, No. 4, 1987, pp. 296-302.
25. Hollis, B. R., "Real-Gas Flow Properties for NASA Langley Research Center Aerothermodynamic Facilities Complex Wind Tunnels," NASA CR-4755, September 1996.

Table 1. Plug locations for the tripped model configurations.

Model 2		Model 3		Model 4		Model 5		Model 6	
x/L_{ref}	y/L_{ref}	x/L_{ref}	y/L_{ref}	x/L_{ref}	y/L_{ref}	x/L_{ref}	y/L_{ref}	x/L_{ref}	y/L_{ref}
0.10	0	0.50	0	0.70	0	0.74	0	0.85	0
–	–	0.50	0.1008	0.70	0.1658	0.74	0.2348	–	–
–	–	0.50	-0.1008	0.70	-0.1658	0.74	-0.2348	–	–

Table 2. Fiducial locations on all the final models.

x/L_{ref}	y/L_{ref}
0.05	0
0.30	0
0.80	0
1.00	0
0.70	0.2298
0.70	-0.2298
0.80	0.2937
0.80	-0.2937

Table 3. Protuberance dimensions and quantities requested to be manufactured. Note that the trip heights, k , in the table are the designed values, not the as-built heights.

Trip Type	k {inch}	Quantity
PB	0.006	3
	0.007	3
	0.010	1
	0.012	1
RPB	0.010	1
	0.012	1
F	0.005	1
	0.006	1
	0.007	3
	0.010	3
	0.012	2
AF	0.006	2
H	0.008	2
TOTAL		24

Table 4. Proposed test plan and test conditions for models with protuberances (baseline configuration tests not included).

Config.	Model	Nominal Mach	Re_{inc}/ft (Design)	x/L_{ref}	y/L_{ref}	Protuberance Type (Loc)	k {inch}	k/δ	Objective	Runs per Config.
1	2	6	1.0×10^6	0.10	0	PB (CL)	0.007	0.378	Repeat of existing data	5
2	2	6	1.0×10^6	0.10	0	F (CL)	0.007	0.378	Shape effect data	5
3	2	6	0.6×10^6	0.10	0	F (CL)	0.012	0.506	Shape effect data	5
4	3	6	0.6×10^6	0.50	0	F (CL)	0.012	0.333	Shape effect data	5
				0.50	-0.1008	PB (Port AL)	0.012	0.405	Repeat of existing data	
				0.50	0.1008	RPB (STB AL)	0.012	0.405	Shape effect data	
5	3	6	1.0×10^6	0.50	0	PB (CL)	0.007	0.250	Repeat of existing data	5
				0.50	-0.1008	F (Port AL)	0.007	0.304	Shape effect data	
				0.50	0.1008	H (STB AL)	0.008	0.348	Shape effect data	
6	4	6	0.6×10^6	0.70	0	F (CL)	0.010	0.250	Shape effect data	5
				0.70	-0.1658	PB (Port side)	0.010	0.370	Data inbound shock interaction	
				0.70	0.1658	RPB (STB side)	0.010	0.370	Data inbound shock interaction	
7	4	6	1.0×10^6	0.70	0	PB (CL)	0.006	0.193	Extension of existing data	5
				0.70	-0.1658	F (Port side)	0.006	0.286	Data inbound shock interaction	
				0.70	0.1658	AF (STB side)	0.006	0.286	Data inbound shock interaction	
8	5	6	0.6×10^6	0.74	0	F (CL)	0.010	0.247	Shape effect data	5
				0.74	-0.2348	F (Port side)	0.007	0.400	Shape effect data	
				0.74	0.2348	PB (STB side)	0.007	0.400	Extension of existing data	
9	5	6	1.0×10^6	0.74	0	PB (CL)	0.006	0.191	Extension of existing data	5
				0.74	-0.2348	F (Port side)	0.005	0.368	Shape effect data	
				0.74	0.2348	H (STB side)	0.008	0.588	Shape effect data	
10	6	6	1.0×10^6	0.85	0	PB (CL)	0.006	0.179	Repeat of existing data	5
11	6	6	1.0×10^6	0.85	0	AF (CL)	0.006	0.179	Shape effect data	5
12	6	6	0.6×10^6	0.85	0	F (CL)	0.010	0.232	Shape effect data	5
$L_{ref} = 11.52$ in.										Total Potential Protuberance Runs = 60

Table 5. Test 6922 final run log.

Run	Date (2006)	Model	Config.	Re_{∞}/ft $\times 10^{-6}$	P_t {psia}	T_t {°F}	Trips							
							x/L_{ref}	Port Side		y/L_{ref}	Centerline		Starboard Side	
								Type	k {in.}		Type	k {in.}	Type	k {in.}
1	8/21	1	Bsln	1.90	114	442	-	-	-	-	-	-	-	-
2	8/21	1	Bsln	3.74	230	447	-	-	-	-	-	-	-	-
3	8/21	1	Bsln	5.45	350	469	-	-	-	-	-	-	-	-
4	8/21	1	Bsln	0.57	30	397	-	-	-	-	-	-	-	-
5	8/21	1	Bsln	4.49	291	474	-	-	-	-	-	-	-	-
6	8/22	2	Bsln	2.08	126	445	0.10	-	-	-	-	-	-	-
7*	8/22	2	Bsln	3.77	231	445	0.10	-	-	-	-	-	-	-
8*	8/22	2	Bsln	2.08	125	442	0.10	-	-	-	-	-	-	-
9	8/22	2	Bsln	2.08	125	443	0.10	-	-	-	-	-	-	-
10	8/22	2	1	1.78	107	441	0.10	-	-	0	PB	0.008	-	-
11	8/22	2	1	1.09	61	414	0.10	-	-	0	PB	0.008	-	-
12	8/23	2	1	1.25	71	420	0.10	-	-	0	PB	0.008	-	-
13	8/23	2	1	0.86	47	409	0.10	-	-	0	PB	0.008	-	-
14	8/23	2	2	1.77	106	445	0.10	-	-	0	F	0.008	-	-
15	8/23	2	2	1.06	59	414	0.10	-	-	0	F	0.008	-	-
16	8/23	2	2	0.80	46	408	0.10	-	-	0	F	0.008	-	-
17	8/23	2	2	0.57	30	397	0.10	-	-	0	F	0.008	-	-
18*	8/23	2	2	0.25	-	-	0.10	-	-	0	F	0.008	-	-
19	8/23	2	2	0.45	22	377	0.10	-	-	0	F	0.008	-	-
20	8/23	2	2	1.25	71	419	0.10	-	-	0	F	0.008	-	-
21	8/24	3	Bsln	1.89	113	439	0.50	-	-	-	-	-	-	-
22	8/24	3	Bsln	3.74	228	447	0.50	-	-	-	-	-	-	-
23*	8/24	3	5	1.78	106	440	0.50	-0.1008	F	0.007	PB	0.008	0.1008	0.014
24*	8/24	3	5	1.78	106	439	0.50	-0.1008	F	0.007	PB	0.008	0.1008	0.007
25	8/24	3	5	1.76	105	441	0.50	-0.1008	F	0.007	PB	0.008	0.1008	0.007
26	8/24	3	5	2.07	125	443	0.50	-0.1008	F	0.007	PB	0.008	0.1008	0.007
27	8/24	3	5	2.50	153	446	0.50	-0.1008	F	0.007	PB	0.008	0.1008	0.007
28	8/24	3	5	1.07	60	418	0.50	-0.1008	F	0.007	PB	0.008	0.1008	0.007
29	8/24	3	5	1.22	69	421	0.50	-0.1008	F	0.007	PB	0.008	0.1008	0.007
30	8/24	3	5	1.50	86	425	0.50	-0.1008	F	0.007	PB	0.008	0.1008	0.007

* Data not acquired for these runs. 'Bsln' refers to baseline (no trips). $y/L_{ref} > 0$ implies STB side and $y/L_{ref} < 0$ Port side.
Fence trips are oriented 45 degrees relative to the model centerline unless noted otherwise.
Pizza-box and rounded pizza-box trips are oriented with a diagonal line parallel (i.e., faces of trip $\pm 45^\circ$) to model centerline unless noted otherwise.

Table 5. Test 6922 final run log – (Cont).

Run	Date (2006)	Model	Config.	Re_{∞}/ft $\times 10^{-6}$	P_t {psia}	T_t {°F}	Trips									
							x/L_{ref}	Port Side		Centerline				Starboard Side		
								y/L_{ref}	Type	k {in.}	y/L_{ref}	Type	k {in.}	y/L_{ref}	Type	k {in.}
31	8/25	3	5	3.06	185	440	0.50	-0.1008	F	0.007	0	PB	0.008	0.1008	H	0.007
32	8/25	3	5	1.64	96	428	0.50	-0.1008	F	0.007	0	PB	0.008	0.1008	H	0.007
33	8/25	3	5	3.43	212	448	0.50	-0.1008	F	0.007	0	PB	0.008	0.1008	H	0.007
34	8/25	3	5A	2.06	124	441	0.50	-0.1008	PB	0.008	0	F	0.007	0.1008	H	0.007
35	8/25	3	5A	1.49	86	424	0.50	-0.1008	PB	0.008	0	F	0.007	0.1008	H	0.007
36	8/25	3	5A	1.09	61	414	0.50	-0.1008	PB	0.008	0	F	0.007	0.1008	H	0.007
37	8/25	3	5A	1.23	70	420	0.50	-0.1008	PB	0.008	0	F	0.007	0.1008	H	0.007
38	8/25	3	5A	3.01	184	446	0.50	-0.1008	PB	0.008	0	F	0.007	0.1008	H	0.007
39	8/25	3	5A	2.55	155	442	0.50	-0.1008	PB	0.008	0	F	0.007	0.1008	H	0.007
40	8/25	3	5A	3.38	209	450	0.50	-0.1008	PB	0.008	0	F	0.007	0.1008	H	0.007
41	8/25	3	5A	1.18	67	422	0.50	-0.1008	PB	0.008	0	F	0.007	0.1008	H	0.007
42	8/28	3	5B	1.51	88	428	0.50	-0.1008	PB	0.008	0	H	0.007	0.1008	F	0.007
43	8/28	3	5B	1.78	107	443	0.50	-0.1008	PB	0.008	0	H	0.007	0.1008	F	0.007
44	8/28	3	5B	1.23	70	423	0.50	-0.1008	PB	0.008	0	H	0.007	0.1008	F	0.007
45	8/28	3	5B	2.10	126	441	0.50	-0.1008	PB	0.008	0	H	0.007	0.1008	F	0.007
46	8/28	3	5B	2.56	155	443	0.50	-0.1008	PB	0.008	0	H	0.007	0.1008	F	0.007
47*	8/28	4	Bsln	2.53	153	441	0.70	-	-	-	-	-	-	-	-	-
48	8/28	4	Bsln	3.70	227	445	0.70	-	-	-	-	-	-	-	-	-
49	8/28	4	Bsln	4.49	290	472	0.70	-	-	-	-	-	-	-	-	-
50	8/28	4	Bsln	3.75	231	447	0.70	-	-	-	-	-	-	-	-	-
51	8/28	4	Bsln	2.07	125	444	0.70	-	-	-	-	-	-	-	-	-
52	8/28	4	Bsln	2.55	156	448	0.70	-	-	-	-	-	-	-	-	-
53	8/28	4	Bsln	1.08	61	416	0.70	-	-	-	-	-	-	-	-	-
54*	8/29	4	Bsln	3.04	185	441	0.70	-	-	-	-	-	-	-	-	-
55	8/29	4	Bsln	3.05	186	444	0.70	-	-	-	-	-	-	-	-	-
56	8/29	4	6A	1.04	58	413	0.70	-0.1658	PB	0.008	0	F	0.007	0.1658	H	0.007
57	8/29	4	6A	0.68	35	398	0.70	-0.1658	PB	0.008	0	F	0.007	0.1658	H	0.007
58	8/29	4	6A	0.85	46	407	0.70	-0.1658	PB	0.008	0	F	0.007	0.1658	H	0.007
59*	8/30	4	6A	1.78	106	439	0.70	-0.1658	PB	0.008	0	F	0.007	0.1658	H	0.007
60	8/30	4	6A	1.79	107	443	0.70	-0.1658	PB	0.008	0	F	0.007	0.1658	H	0.007

Table 5. Test 6922 final run $\log - (\text{Cont})$.

Run	Date (2006)	Model	Config.	Re_∞/ft $\times 10^{-6}$	P_t {psia}	T_t {°F}	Trips									
							Port Side		Centerline		Starboard Side					
							x/L_{ref}	y/L_{ref}	Type	k {in.}	y/L_{ref}	Type	k {in.}	y/L_{ref}	Type	k {in.}
61	8/30	4	6A	1.50	87	425	0.70	-0.1658	PB	0.008	0	F	0.007	0.1658	H	0.007
62	8/30	4	6A	1.22	69	418	0.70	-0.1658	PB	0.008	0	F	0.007	0.1658	H	0.007
63	8/30	4	6A	2.06	124	443	0.70	-0.1658	PB	0.008	0	F	0.007	0.1658	H	0.007
64	8/30	4	6B	1.06	59	414	0.70	-0.1658	PB ¹	0.008	0	F ¹	0.007	0.1658	AF ¹	0.006/0.004
65	8/30	4	6B	1.50	86	425	0.70	-0.1658	PB ¹	0.008	0	F ¹	0.007	0.1658	AF ¹	0.006/0.004
66	8/30	4	6B	0.85	46	409	0.70	-0.1658	PB ¹	0.008	0	F ¹	0.007	0.1658	AF ¹	0.006/0.004
67	8/30	4	6B	1.23	70	420	0.70	-0.1658	PB ¹	0.008	0	F ¹	0.007	0.1658	AF ¹	0.006/0.004
68	8/31	4	6B	1.79	107	440	0.70	-0.1658	PB ¹	0.008	0	F ¹	0.007	0.1658	AF ¹	0.006/0.004
69	8/31	4	6C	1.79	107	440	0.70	-0.1658	PB ³	0.008	0	F ²	0.007	0.1658	AF ²	0.006/0.004
70	8/31	4	6C	1.08	60	414	0.70	-0.1658	PB ³	0.008	0	F ²	0.007	0.1658	AF ²	0.006/0.004
71	8/31	4	6C	0.86	47	408	0.70	-0.1658	PB ³	0.008	0	F ²	0.007	0.1658	AF ²	0.006/0.004
72	8/31	4	6C	2.56	155	441	0.70	-0.1658	PB ³	0.008	0	F ²	0.007	0.1658	AF ²	0.006/0.004
73	8/31	4	6C	3.04	186	447	0.70	-0.1658	PB ³	0.008	0	F ²	0.007	0.1658	AF ²	0.006/0.004
74	8/31	4	6C	2.23	134	441	0.70	-0.1658	PB ³	0.008	0	F ²	0.007	0.1658	AF ²	0.006/0.004
75	8/31	6	Bsln	3.04	185	444	0.85	-	-	-	-	-	-	-	-	-
76	8/31	6	Bsln	1.92	115	441	0.85	-	-	-	-	-	-	-	-	-
77	8/31	6	Bsln	3.80	231	441	0.85	-	-	-	-	-	-	-	-	-
78	8/31	6	Bsln	4.50	290	472	0.85	-	-	-	-	-	-	-	-	-
79	8/31	6	Bsln	5.41	350	473	0.85	-	-	-	-	-	-	-	-	-
80*	9/1	6	12	1.08	60	414	0.85	-	-	-	0	F	0.011	-	-	-
81	9/5	6	12	1.07	60	419	0.85	-	-	-	0	F	0.011	-	-	-
82*	9/5	6	12	0.77	42	411	0.85	-	-	-	0	F	0.011	-	-	-
83	9/5	6	12	0.91	50	411	0.85	-	-	-	0	F	0.011	-	-	-
84	9/5	6	12	1.50	87	428	0.85	-	-	-	0	F	0.011	-	-	-
85	9/5	6	12	0.77	41	408	0.85	-	-	-	0	F	0.011	-	-	-
86	9/5	6	12	1.78	107	443	0.85	-	-	-	0	F	0.011	-	-	-
87	9/5	6	12B	1.06	59	414	0.85	-	-	-	0	PB	0.010	-	-	-
88	9/5	6	12B	1.49	86	424	0.85	-	-	-	0	PB	0.010	-	-	-
89*	9/6	6	12B	2.00	125	450	0.85	-	-	-	0	PB	0.010	-	-	-
90	9/6	6	12B	2.07	125	443	0.85	-	-	-	0	PB	0.010	-	-	-

¹ Face of trip perpendicular to model centerline.

² Face of trip parallel to model centerline.

³ Upstream inboard face of trip ~ 22.5 degrees relative to model centerline.

Table 5. Test 6922 final run log – (Cont).

Run	Date (2006)	Model	Config.	Re_{∞}/ft $\times 10^{-6}$	P_t {psia}	T_t {°F}	Trips									
							Port Side		Centerline		Starboard Side					
							x/L_{ref}	y/L_{ref}	Type	k {in.}	y/L_{ref}	Type	k {in.}	y/L_{ref}	Type	k {in.}
91	9/6	6	12B	1.79	108	442	0.85	-	-	-	0	PB	0.010	-	-	-
92	9/6	6	12B	2.31	140	443	0.85	-	-	-	0	PB	0.010	-	-	-
93	9/6	6	12A	1.07	60	415	0.85	-	-	-	0	RPB	0.010	-	-	-
94	9/6	6	12A	1.78	107	442	0.85	-	-	-	0	RPB	0.010	-	-	-
95	9/6	6	12A	1.23	70	420	0.85	-	-	-	0	RPB	0.010	-	-	-
96	9/6	6	12A	1.51	87	426	0.85	-	-	-	0	RPB	0.010	-	-	-
97	9/6	6	12A	2.08	125	441	0.85	-	-	-	0	RPB	0.010	-	-	-
98	9/6	7	Bsln	3.77	231	445	-	-	-	-	-	-	-	-	-	-
99	9/6	7	Bsln	3.78	231	444	-	-	-	-	-	-	-	-	-	-
100	9/7	7	Bsln	1.92	115	440	-	-	-	-	-	-	-	-	-	-
101	9/7	7	Bsln	0.59	30	399	-	-	-	-	-	-	-	-	-	-
102*	9/7	7	Bsln	3.01	184	445	-	-	-	-	-	-	-	-	-	-
103	9/7	7	Bsln	3.03	185	446	-	-	-	-	-	-	-	-	-	-
104	9/7	7	Bsln	4.51	290	469	-	-	-	-	-	-	-	-	-	-
105	9/7	5	Bsln	2.07	124	441	-	-	-	-	-	-	-	-	-	-
106*	9/7	5	Bsln	2.56	156	445	-	-	-	-	-	-	-	-	-	-
107*	9/7	5	Bsln	2.53	155	446	-	-	-	-	-	-	-	-	-	-
108	9/7	5	Bsln	2.54	155	446	-	-	-	-	-	-	-	-	-	-
109	9/7	5	8	1.06	59	414	0.74	-0.2348	F	0.007	0	F	0.011	0.2348	PB	0.008
110	9/8	5	8	0.94	51	407	0.74	-0.2348	F	0.007	0	F	0.011	0.2348	PB	0.008
111	9/8	5	8	0.57	29	396	0.74	-0.2348	F	0.007	0	F	0.011	0.2348	PB	0.008
112	9/8	5	8	0.44	22	395	0.74	-0.2348	F	0.007	0	F	0.011	0.2348	PB	0.008
113	9/8	5	8	0.76	41	409	0.74	-0.2348	F	0.007	0	F	0.011	0.2348	PB	0.008
114	9/8	5	8	1.92	115	443	0.74	-0.2348	F	0.007	0	F	0.011	0.2348	PB	0.008
115	9/8	5	8A	1.06	59	414	0.74	-0.2348	F	0.007	0	PB	0.010	0.2348	AF	0.006/0.004
116	9/8	5	8A	0.59	30	398	0.74	-0.2348	F	0.007	0	PB	0.010	0.2348	AF	0.006/0.004
117	9/8	5	8A	0.78	42	408	0.74	-0.2348	F	0.007	0	PB	0.010	0.2348	AF	0.006/0.004
118	9/8	5	8A	0.94	51	408	0.74	-0.2348	F	0.007	0	PB	0.010	0.2348	AF	0.006/0.004
119	9/8	5	8A	1.52	88	427	0.74	-0.2348	F	0.007	0	PB	0.010	0.2348	AF	0.006/0.004
120	9/11	5	8A	1.20	68	421	0.74	-0.2348	F	0.007	0	PB	0.010	0.2348	AF	0.006/0.004
121*	9/11	5	8A	3.00	185	-	0.74	-0.2348	F	0.007	0	PB	0.010	0.2348	AF	0.006/0.004

Table 6. Final Test 6922 matrix and BLT Tool v.1 flow parameters based on LATCH solutions for models with protuberances (baseline configuration test results not included). The nominal Mach number is $M = 6$ for all test conditions.

Config.	Model	Re_{inc}/ft	$Re_{\infty,1}/ft$	$Re_{\infty,2}/ft$	x/L_{ref}	y/L_{ref}	Trip Type	k {in.}	Re_{θ}/M_e	k/δ	C	Runs per Config.
1	2	9.75×10^5	8.60×10^5	1.09×10^6	0.10	0	PB	0.008	66.21	0.428	28.31	4
2	2	6.85×10^5	5.70×10^5	8.00×10^5	0.10	0	F (+45°)	0.008	55.84	0.360	20.11	6
5	3	1.57×10^6	1.50×10^6	1.64×10^6	0.50	0	PB	0.008	142.68	0.357	50.90	9
					0.50	-0.1008	F (+45°)	0.007	-	-	-	
5A	3	1.14×10^6	1.09×10^6	1.18×10^6	0.50	0	F (+45°)	0.007	121.86	0.267	32.48	8
					0.50	-0.1008	PB	0.008	-	-	-	
5B	3	1.65×10^6	1.51×10^6	1.78×10^6	0.50	0	H	0.007	146.06	0.320	46.67	5
					0.50	-0.1008	PB	0.008	-	-	-	
6A	4	9.45×10^5	8.50×10^5	1.04×10^6	0.70	0	F (+45°)	0.007	134.35	0.219	29.42	7
					0.70	-0.1658	PB	0.008	87.54	0.335	29.30	
6B	4	1.65×10^6	1.50×10^6	1.79×10^6	0.70	0.1658	H	0.007	127.43	0.427	54.40	5
					0.70	0	F (90°)	0.007	148.37	0.242	35.84	
6C	4	9.70×10^5	8.60×10^5	1.08×10^6	0.70	-0.1658	PB (90°)	0.008	97.23	0.373	36.22	6
					0.70	0.1658	AF (90°)	0.006/0.004	116.60	0.335	39.03	
12	6	9.90×10^5	9.10×10^5	1.07×10^6	0.85	0	F (0°)	0.007	213.22	0.347	74.03	5
12B	6	1.64×10^6	1.49×10^6	1.79×10^6	0.85	0	PB (~ -22.5°)	0.008	98.00	0.375	36.79	
12A	6	1.37×10^6	1.23×10^6	1.51×10^6	0.85	0	AF (0°)	0.006/0.004	-	-	-	5
8	5	1.00×10^6	9.40×10^5	1.06×10^6	0.74	0	F (+45°)	0.011	148.85	0.326	48.52	6
					0.74	-0.2348	F (-45°)	0.010	191.30	0.381	72.81	
8A	5	5.05×10^5	4.40×10^5	5.70×10^5	0.74	0	RPB	0.010	175.63	0.349	61.36	6
					0.74	0.2348	PB	0.011	142.79	0.349	49.86	
8A	5	1.00×10^6	9.40×10^5	1.06×10^6	0.74	0	F (+45°)	0.007	57.70	0.367	21.14	6
					0.74	-0.2348	PB	0.008	66.41	0.482	32.01	
8A	5	8.60×10^5	7.80×10^5	9.40×10^5	0.74	0	PB	0.010	142.79	0.317	45.32	6
					0.74	-0.2348	F (+45°)	0.007	75.08	0.478	35.87	
Total Number of Acceptable Tripped Runs =												77
- Transition data not acquired.												

- Transition data not acquired.

$$Re_{inc} = \frac{1}{2}(Re_{\infty,1} + Re_{\infty,2})$$



Figure 1. Photograph of a 0.9%-scale Orbiter model installed in the LaRC 20-Inch Mach 6 Air Tunnel.

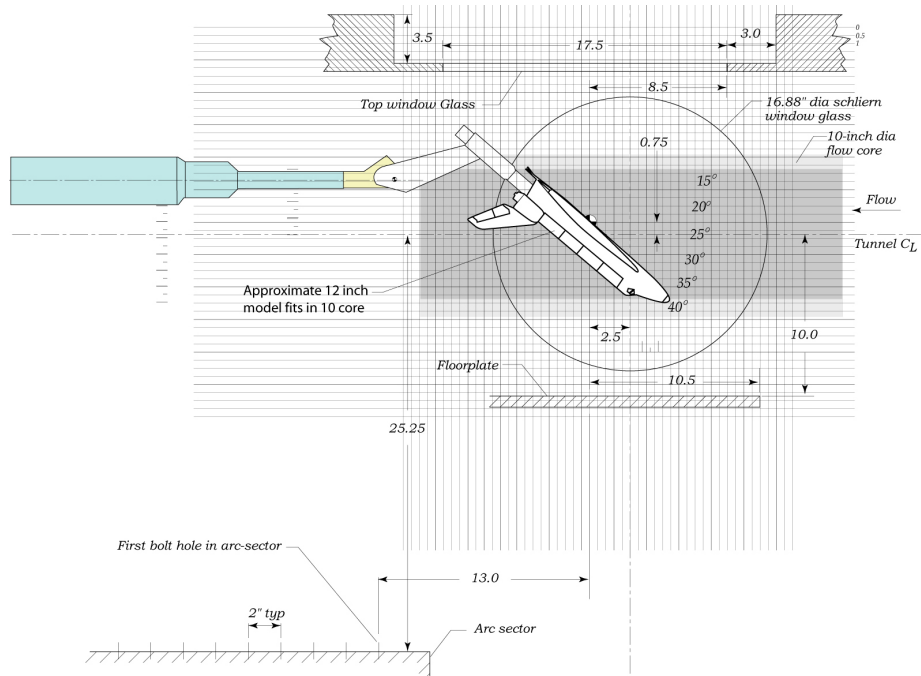


Figure 2. Sketch of a 0.9%-scale Orbiter model installed in the LaRC 20-Inch Mach 6 Air Tunnel.

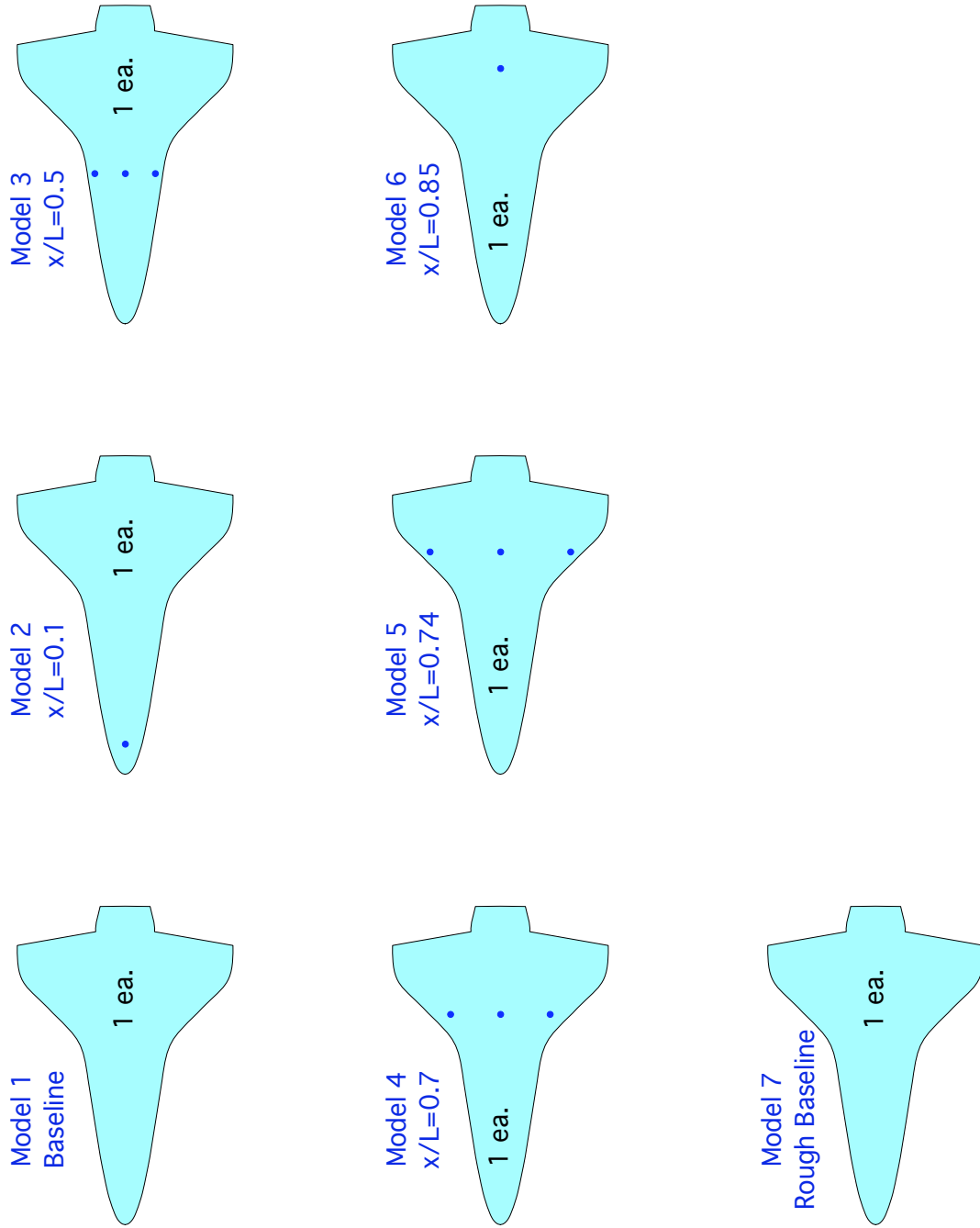


Figure 3. Windward surface sketch of the 7 models used for Test 6922. Holes to accommodate metal dowels are indicated by the filled blue circles.

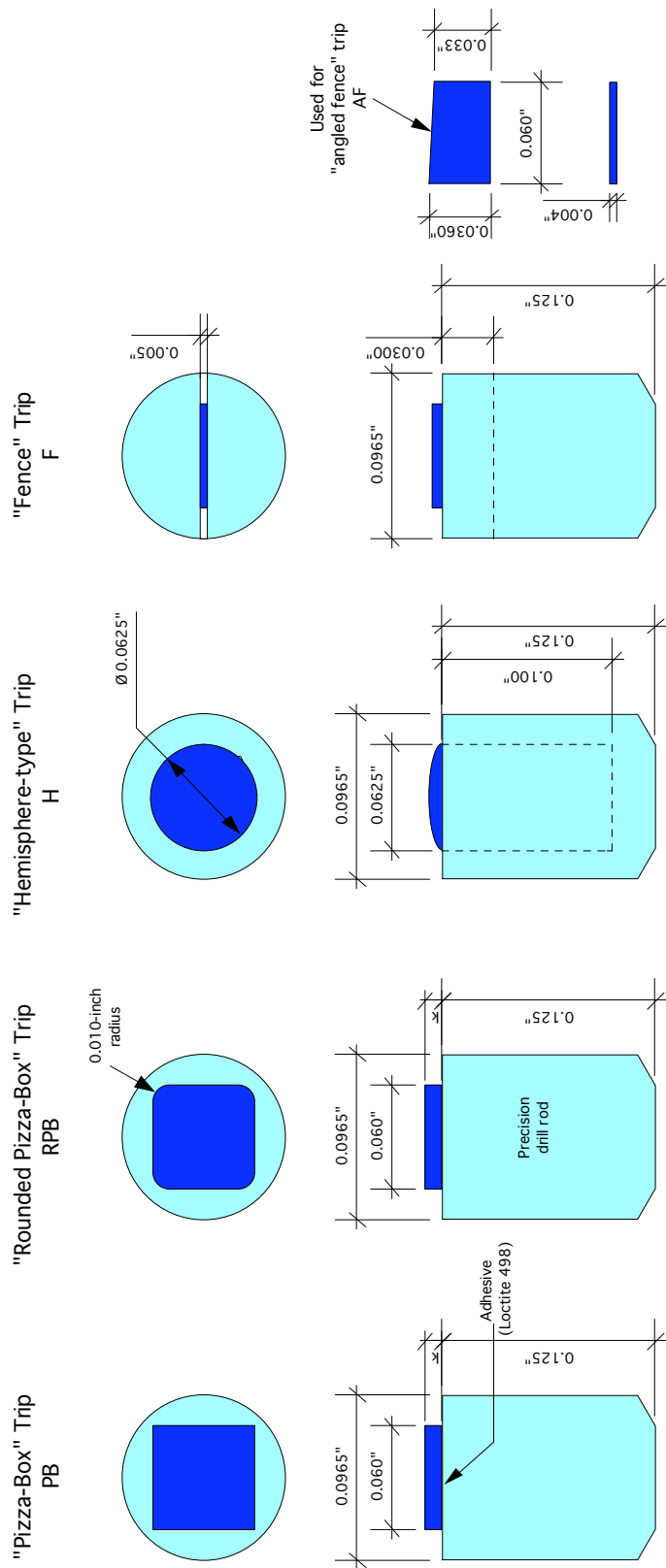


Figure 4. Schematic of trip-dowel assemblies used as protuberances.

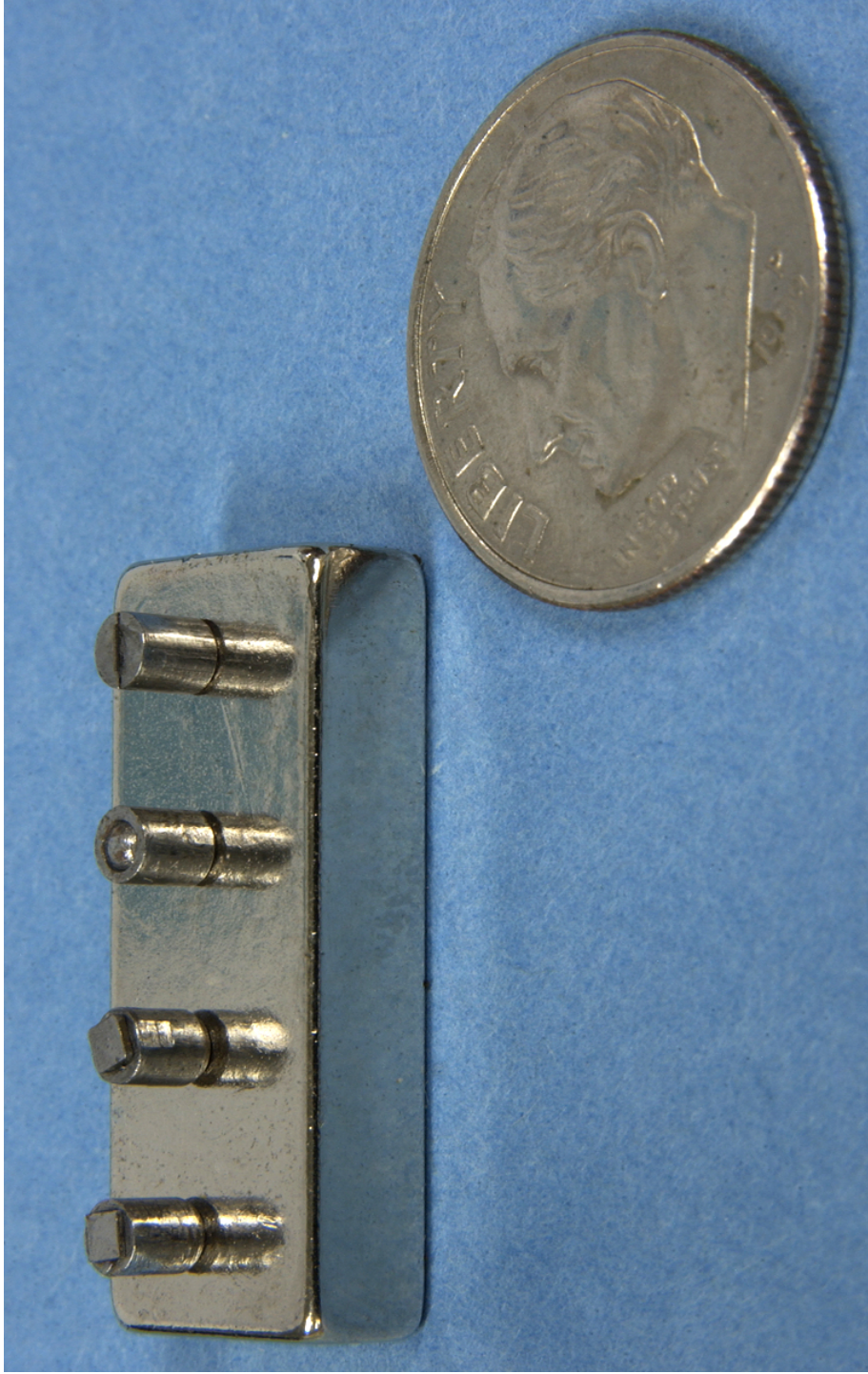


Figure 5. Photograph of four typical trip-dowel assemblies used as protuberances are shown above to demonstrate the scale of the trips. The trip-dowel assemblies shown from left to right are a pizza-box trip, a rounded pizza-box trip, a hemisphere trip, and a fence trip.

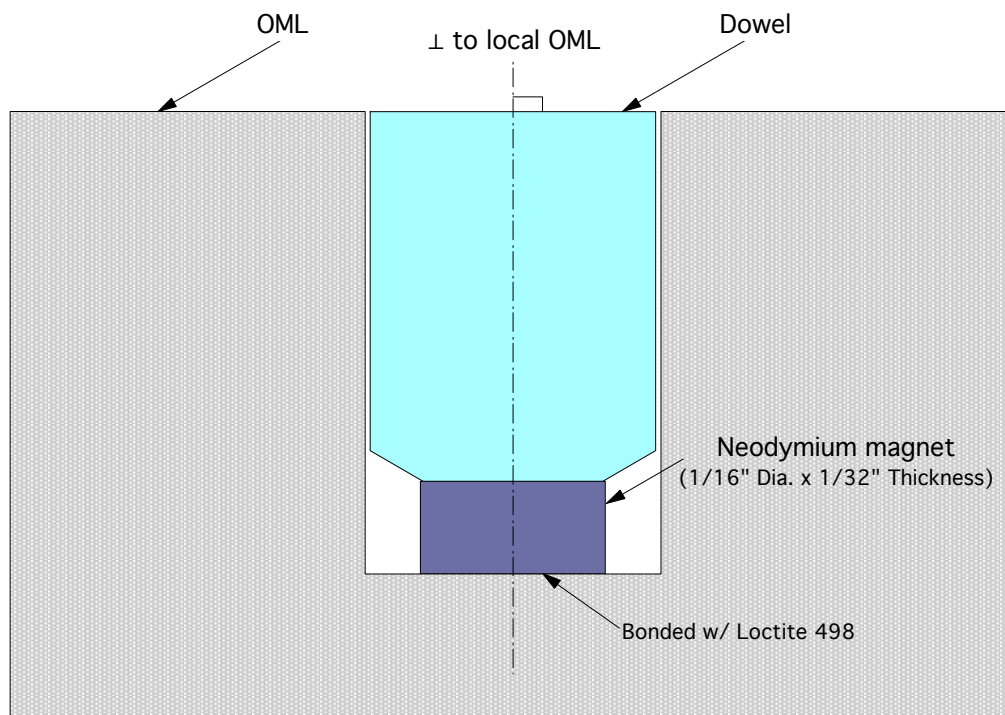


Figure 6. Schematic depicting a blank dowel inserted into a cast ceramic model to match OML of surface.

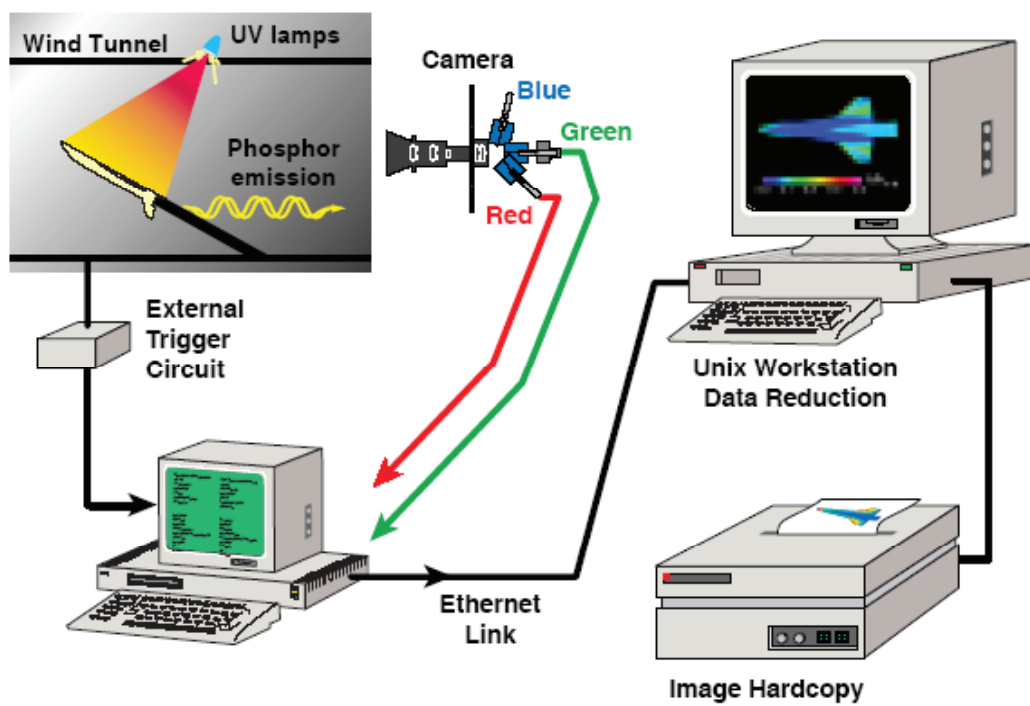


Figure 7. Illustration of phosphor thermography acquisition system.

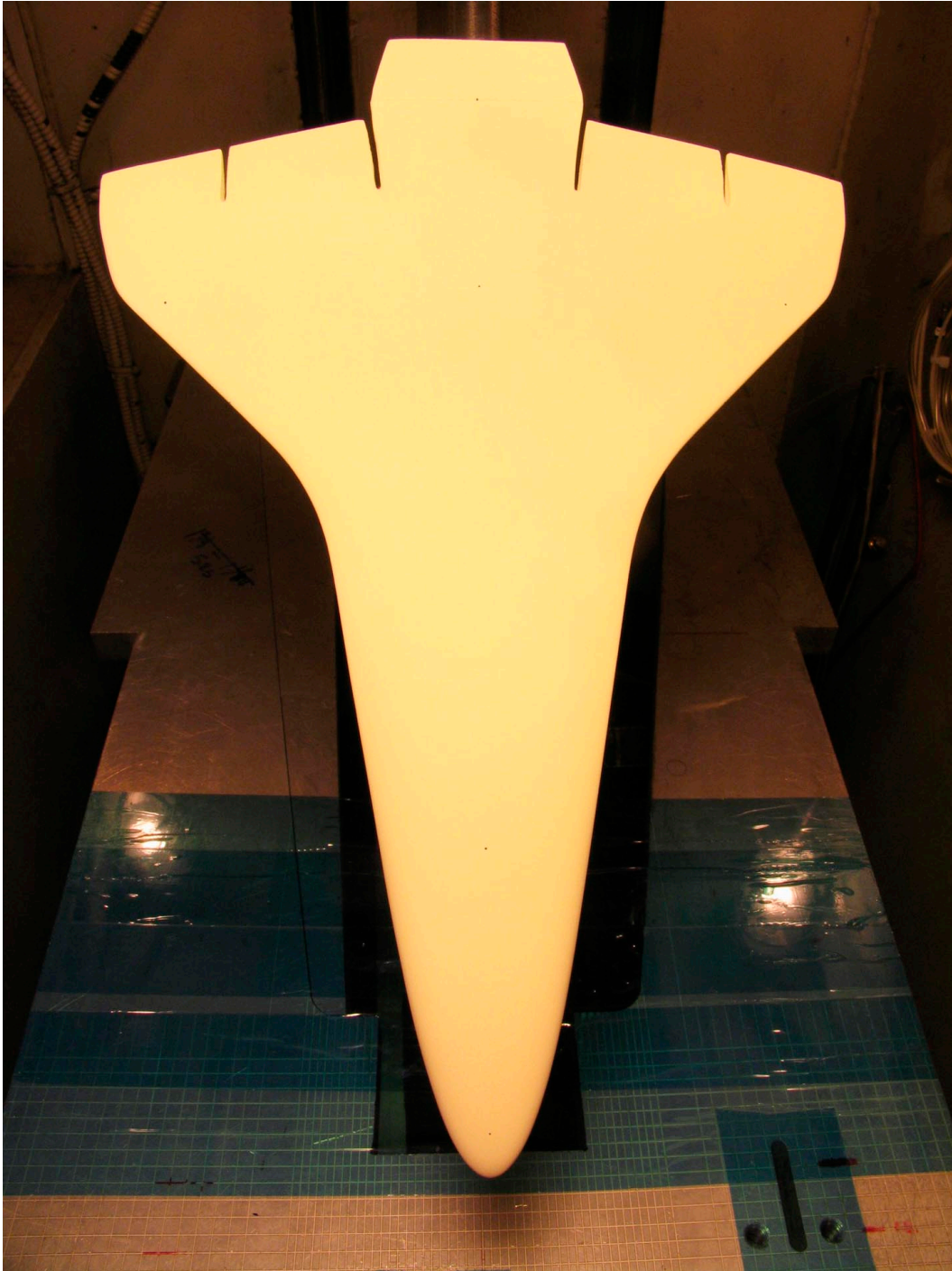


Figure 8. Photographic image of model 1 installed in the 20-Inch Mach 6 Air Tunnel.

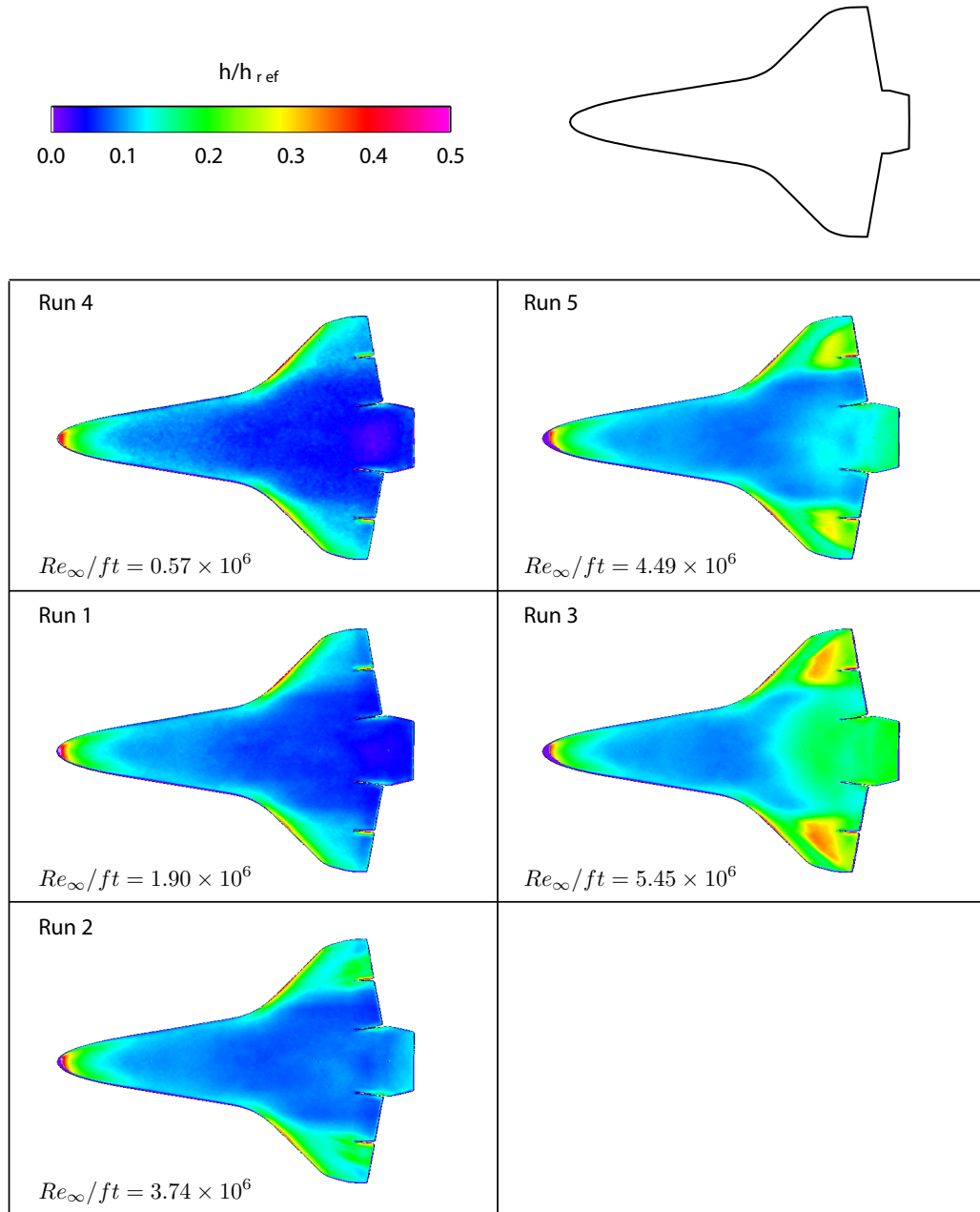


Figure 9. Global aeroheating images for baseline model 1.

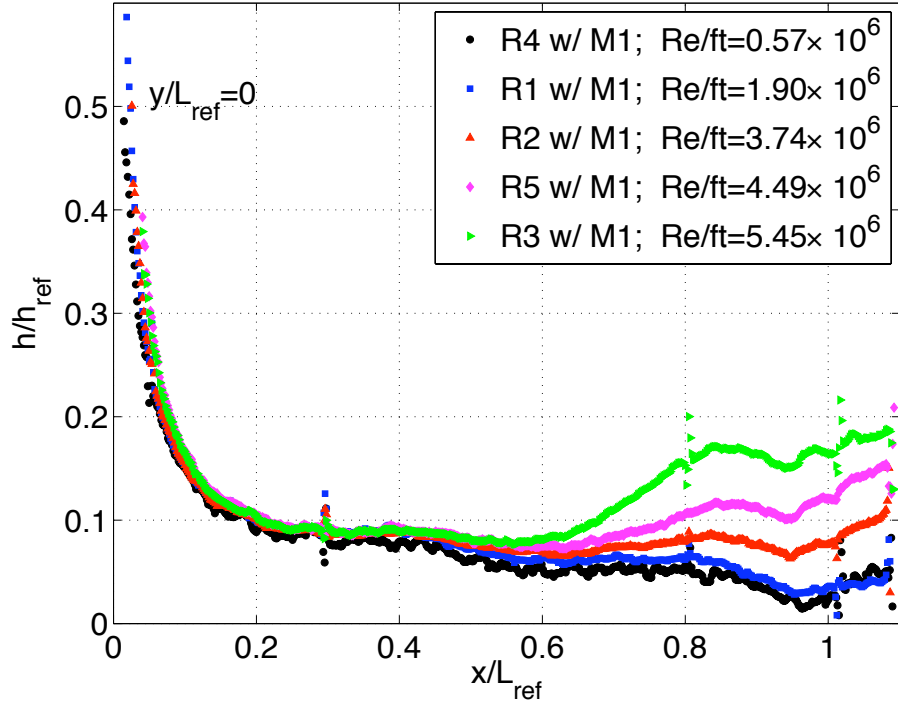


Figure 10. Streamwise line cuts of normalized heat-transfer measurements at $y/L_{ref} = 0$ for baseline model 1.

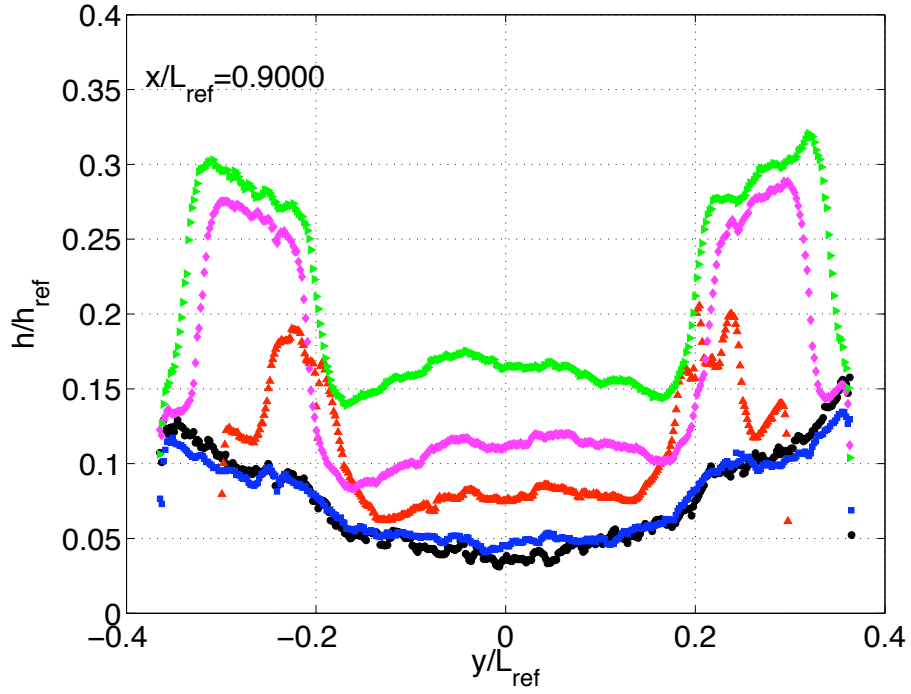


Figure 11. Spanwise line cuts of normalized heat-transfer measurements at $x/L_{ref} = 0.9$ for baseline model 1.

Type	x/L	y/L
Blank	0.10	0

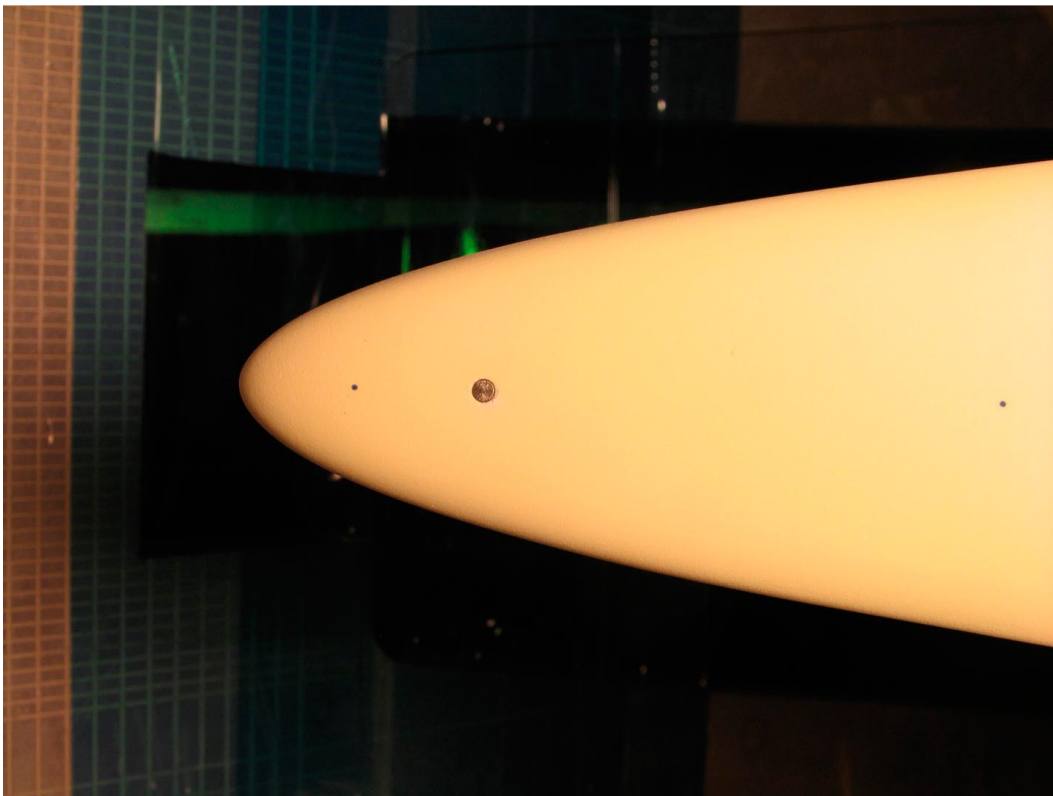
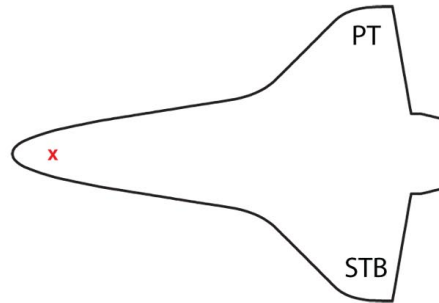


Figure 12. Sketch and close-up image of model 2 with a blank dowel installed.

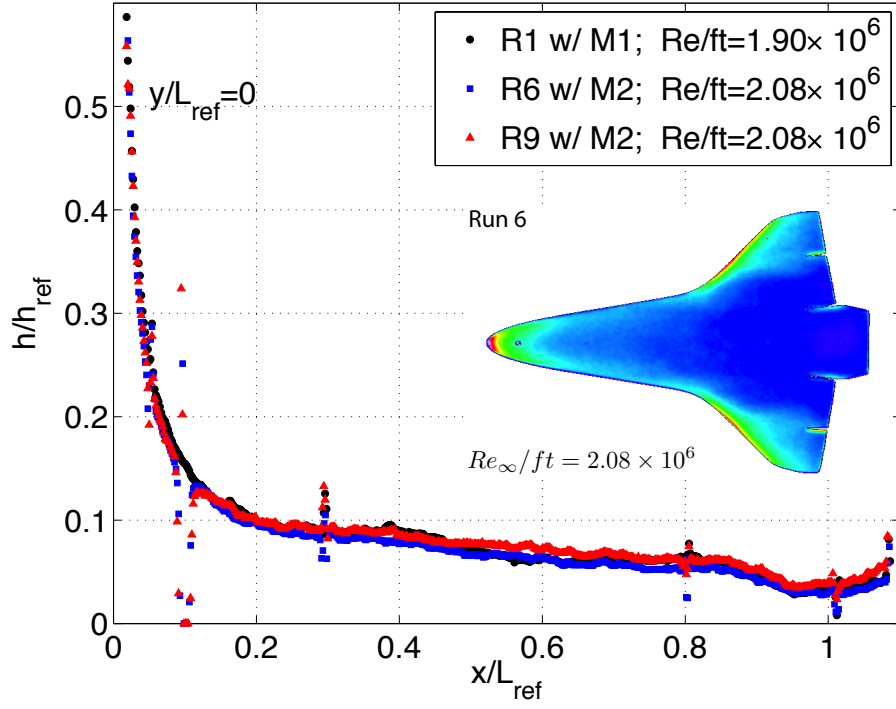


Figure 13. Streamwise line cuts of normalized heat-transfer measurements at $y/L_{ref} = 0$ for model 2 with a blank dowel and baseline model 1.

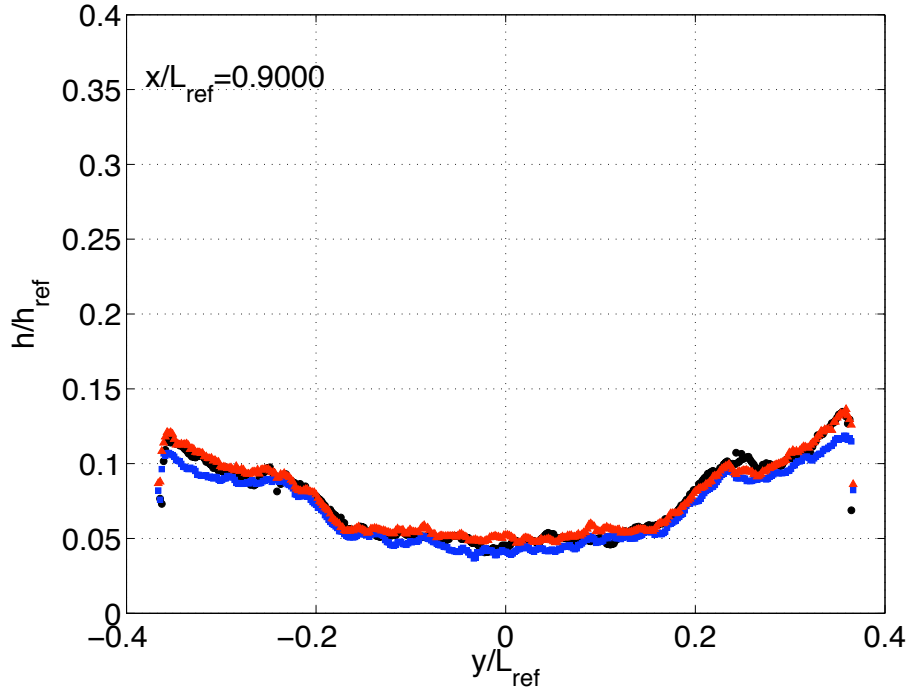


Figure 14. Spanwise line cuts of normalized heat-transfer measurements at $x/L_{ref} = 0.9$ for model 2 with a blank dowel and baseline model 1.

Type	x/L	y/L	k (in)
PB	0.10	0	0.008

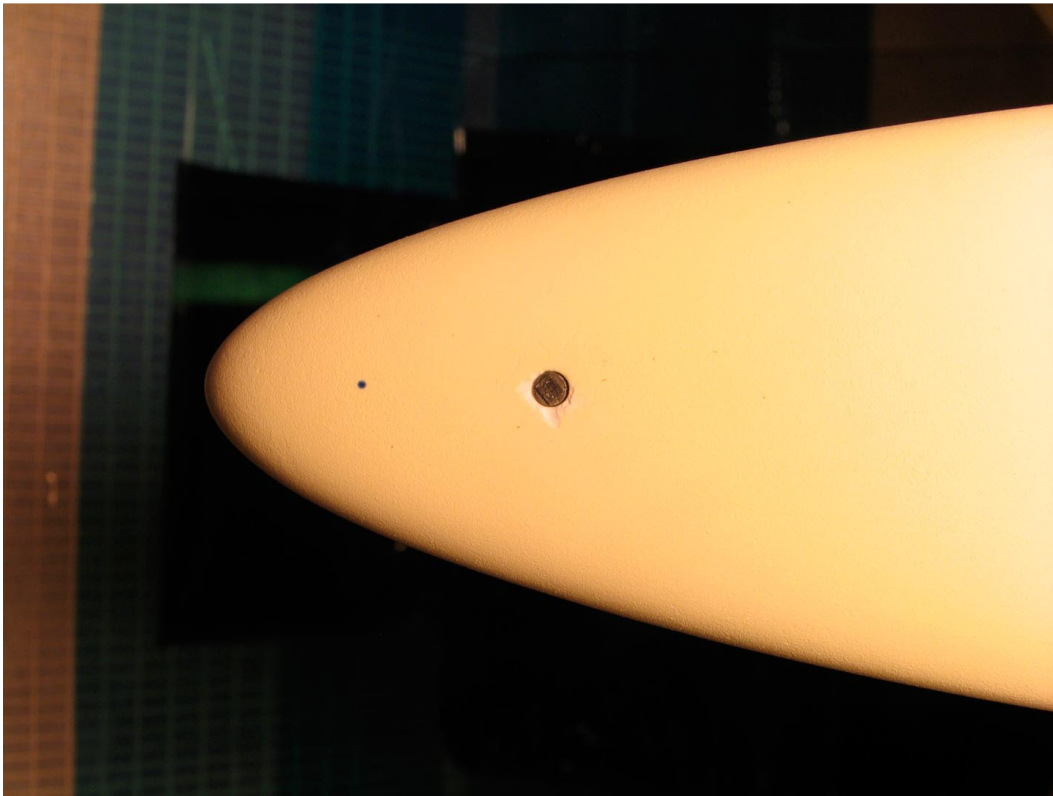


Figure 15. Close-up image of model 2 with configuration 1.

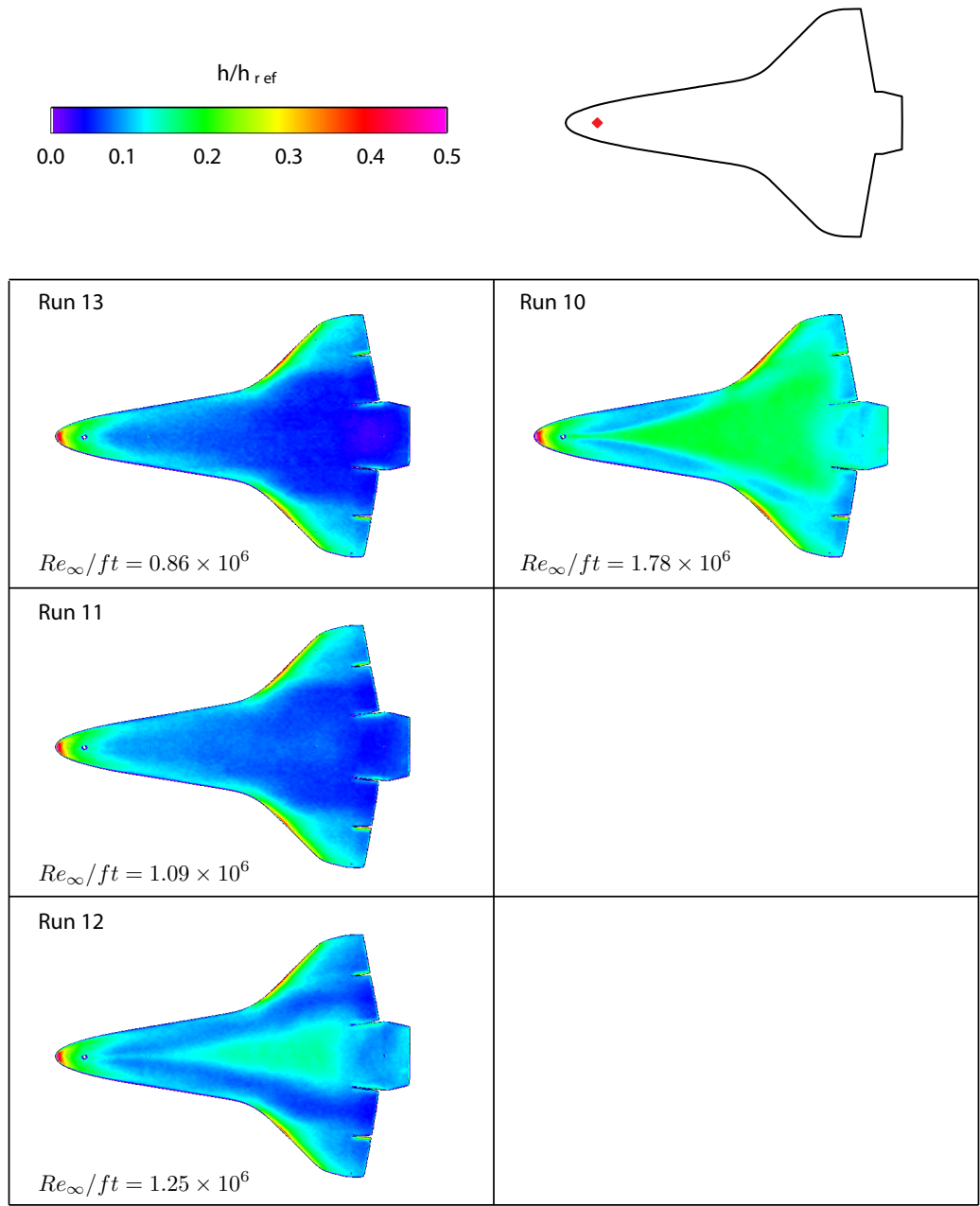


Figure 16. Global aeroheating images for model 2 with configuration 1.

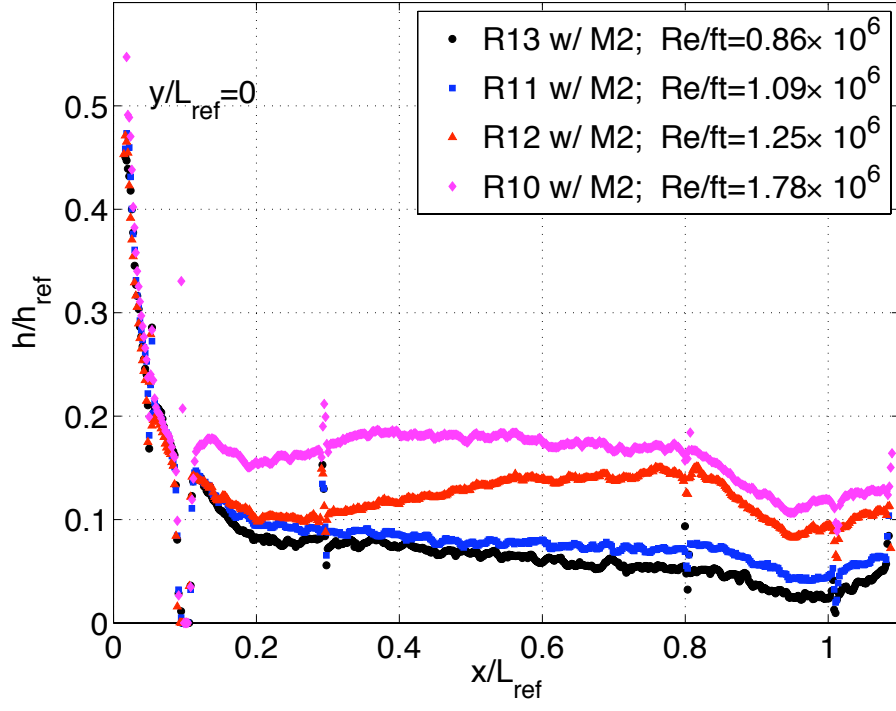


Figure 17. Streamwise line cuts of normalized heat-transfer measurements at $y/L_{ref} = 0$ for model 2 with configuration 1.

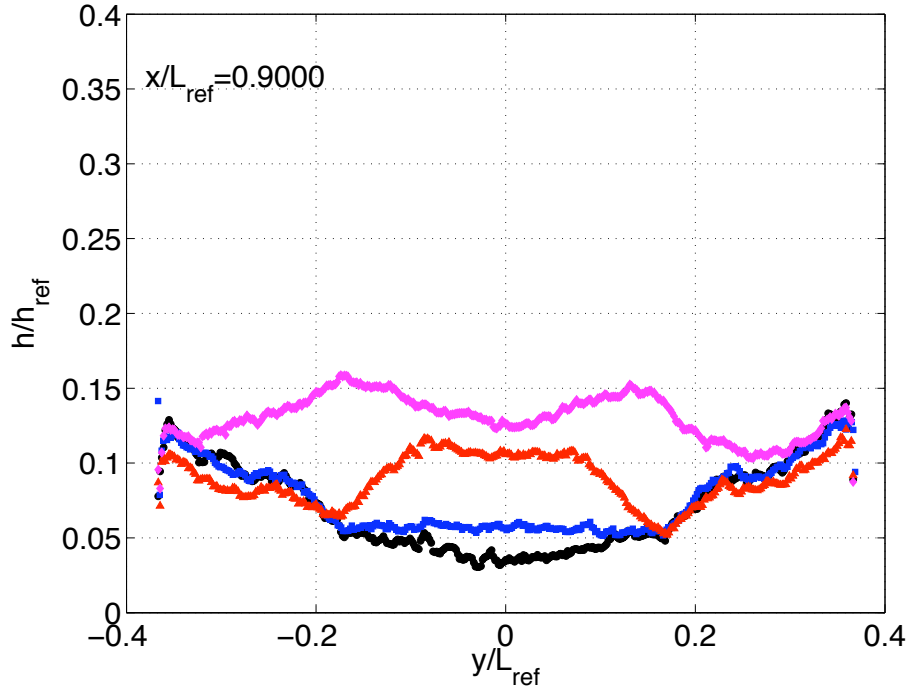


Figure 18. Spanwise line cuts of normalized heat-transfer measurements at $x/L_{ref} = 0.9$ for model 2 with configuration 1.

Type	x/L	y/L	k (in)
F(+45°)	0.10	0	0.008

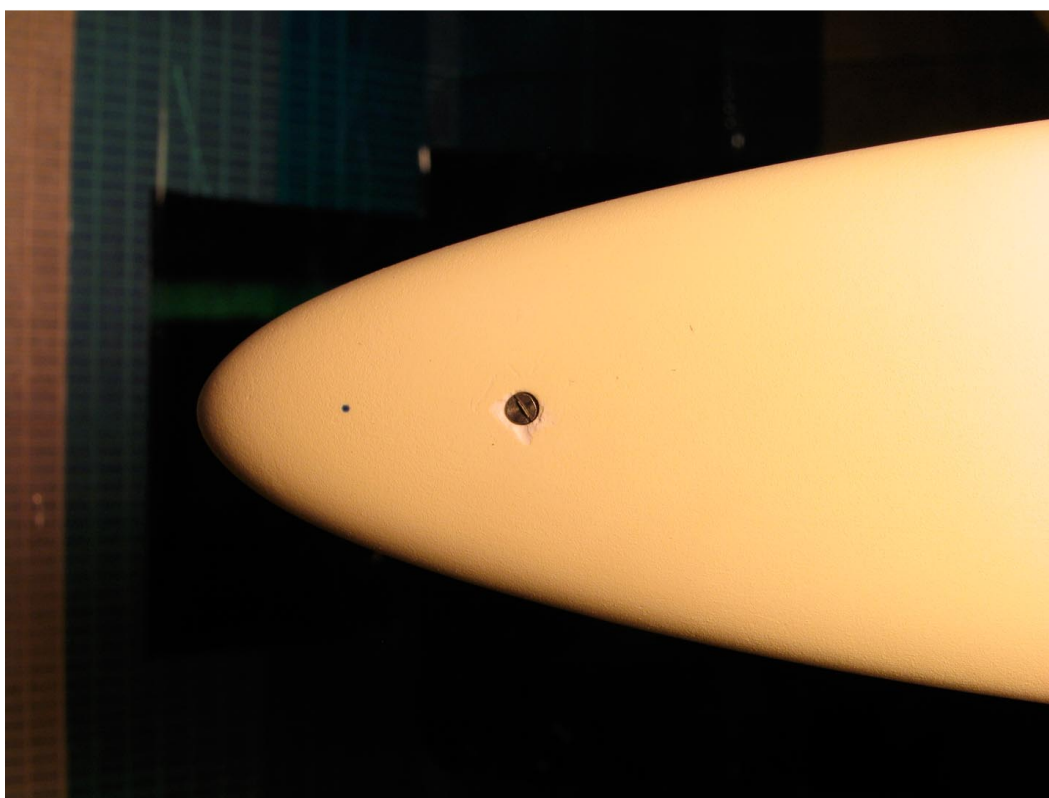


Figure 19. Close-up image of model 2 with configuration 2. Clockwise rotation of fence relative to model centerline is denoted as positive angle.

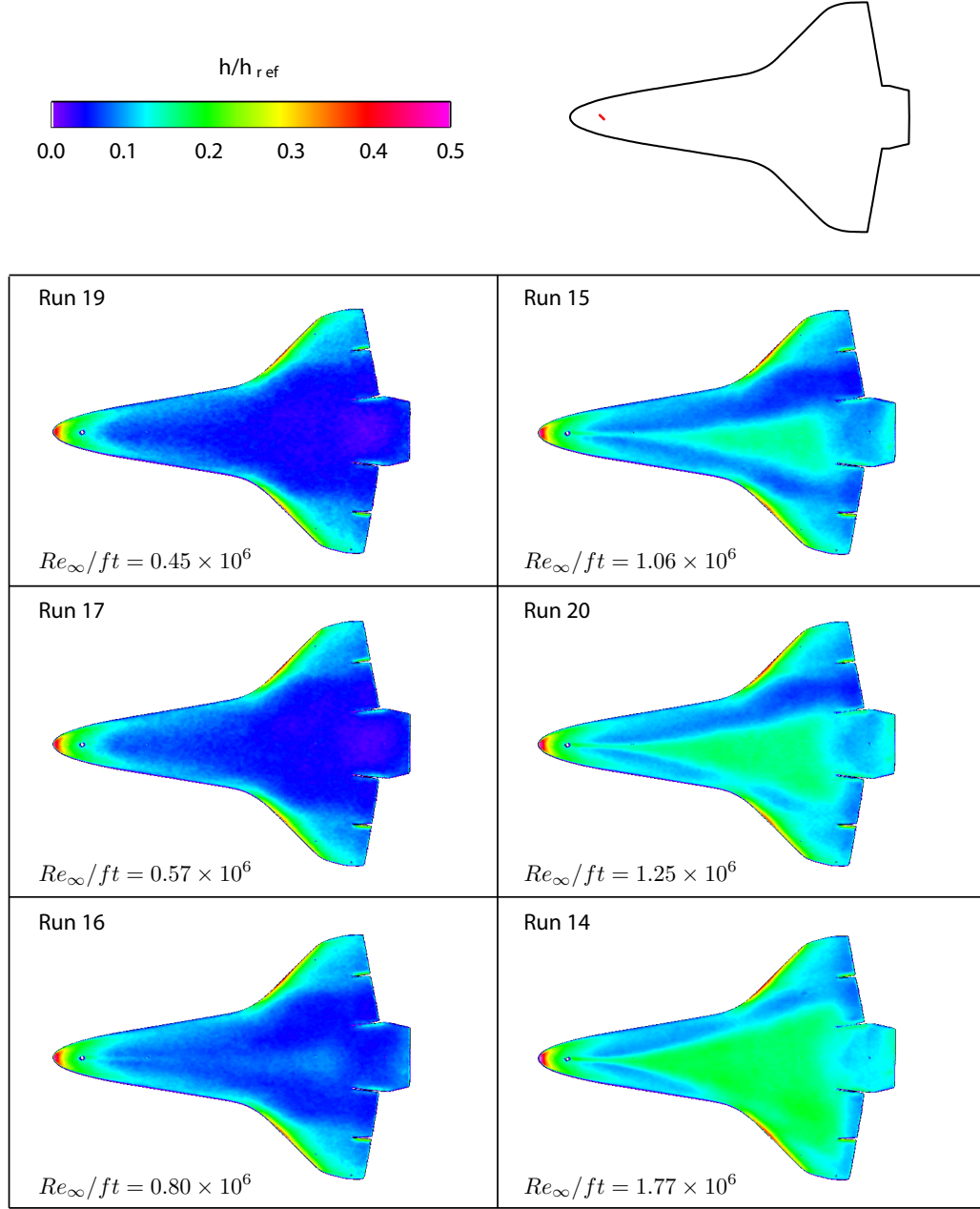


Figure 20. Global aeroheating images for model 2 with configuration 2.

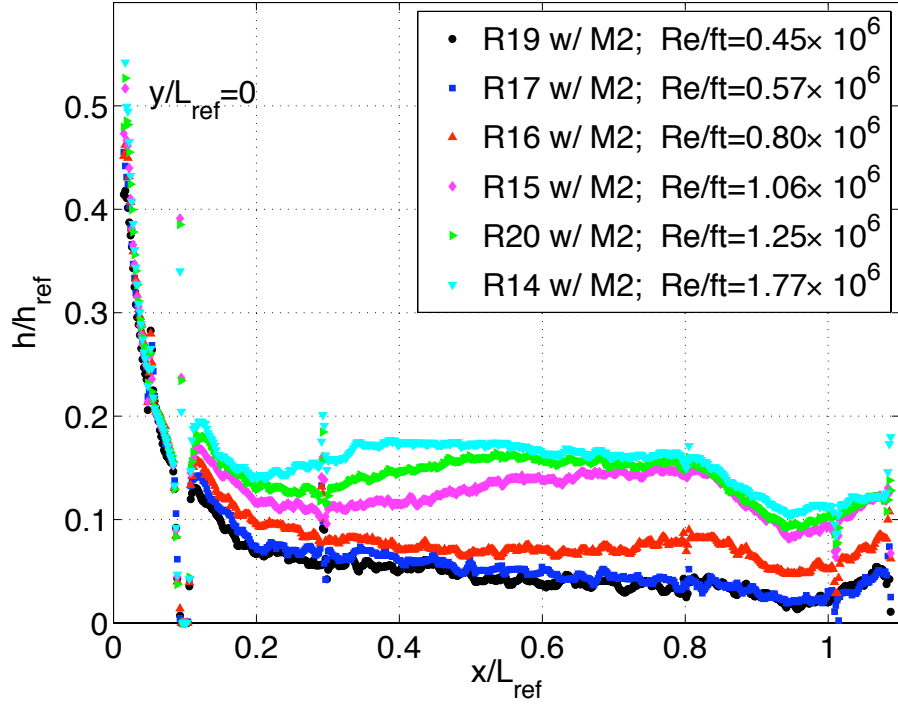


Figure 21. Streamwise line cuts of normalized heat-transfer measurements at $y/L_{ref} = 0$ for model 2 with configuration 2.

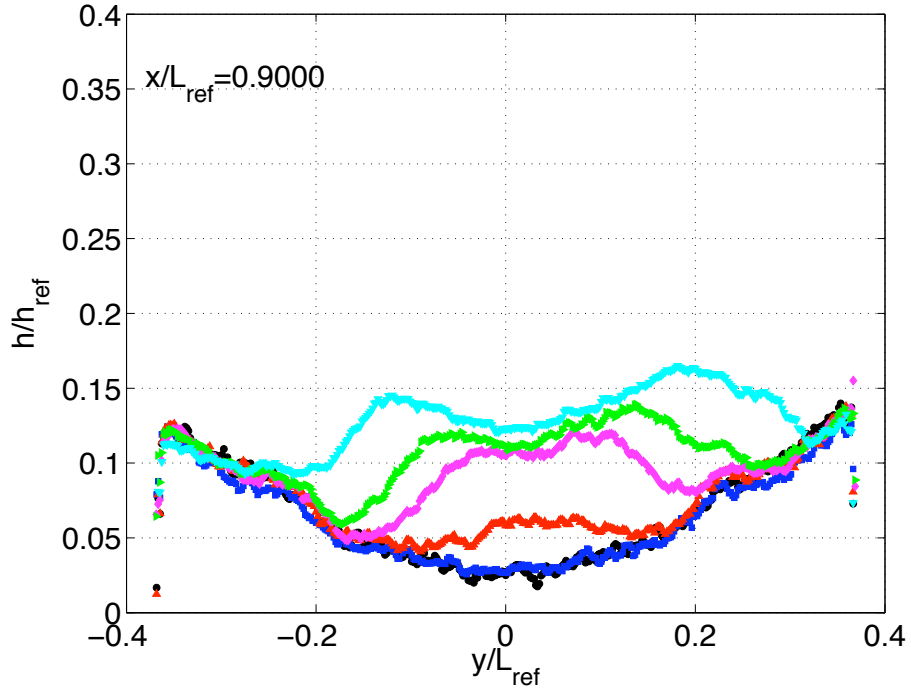


Figure 22. Spanwise line cuts of normalized heat-transfer measurements at $x/L_{ref} = 0.9$ for model 2 with configuration 2.

Type	x/L	y/L
Blank	0.50	-0.1008
Blank	0.50	0
Blank	0.50	0.1008

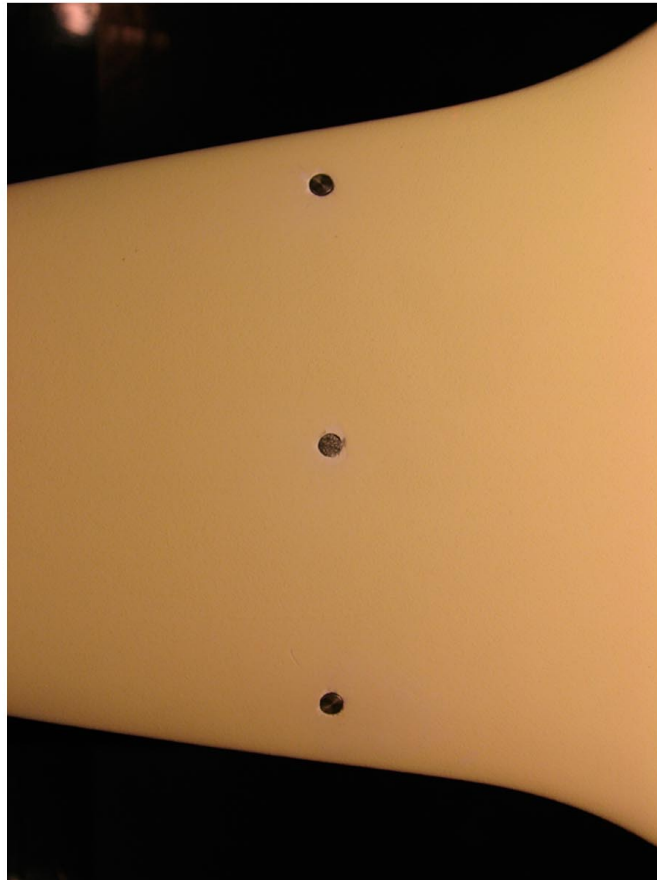
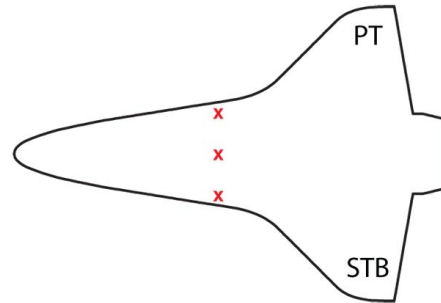


Figure 23. Sketch and close-up image of model 3 with three blank dowels installed.

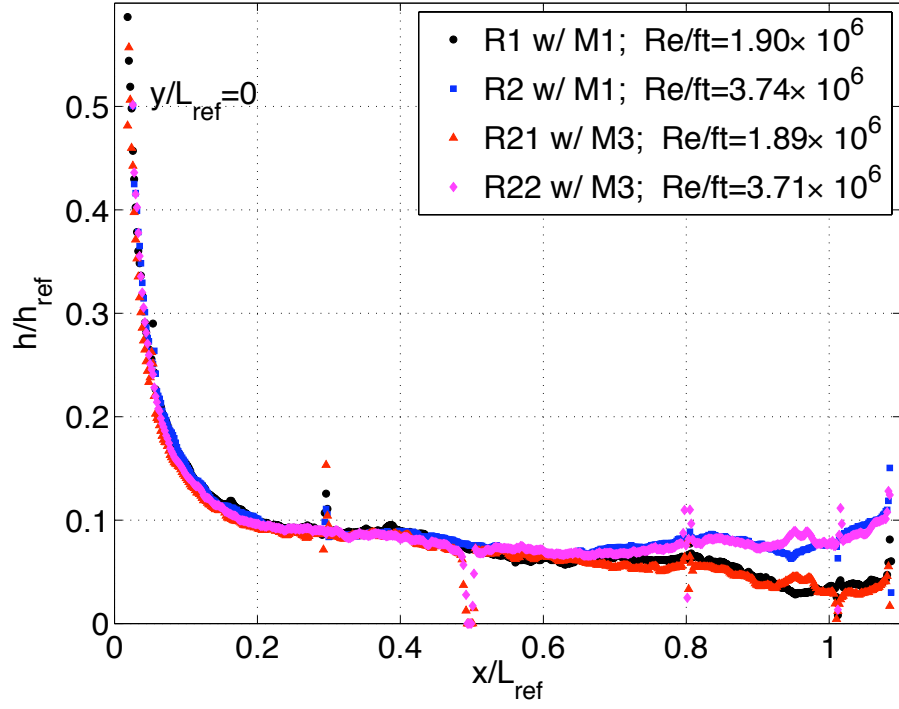


Figure 24. Streamwise line cuts of normalized heat-transfer measurements at $y/L_{ref} = 0$ for model 3 with three blank dowels and baseline model 1.

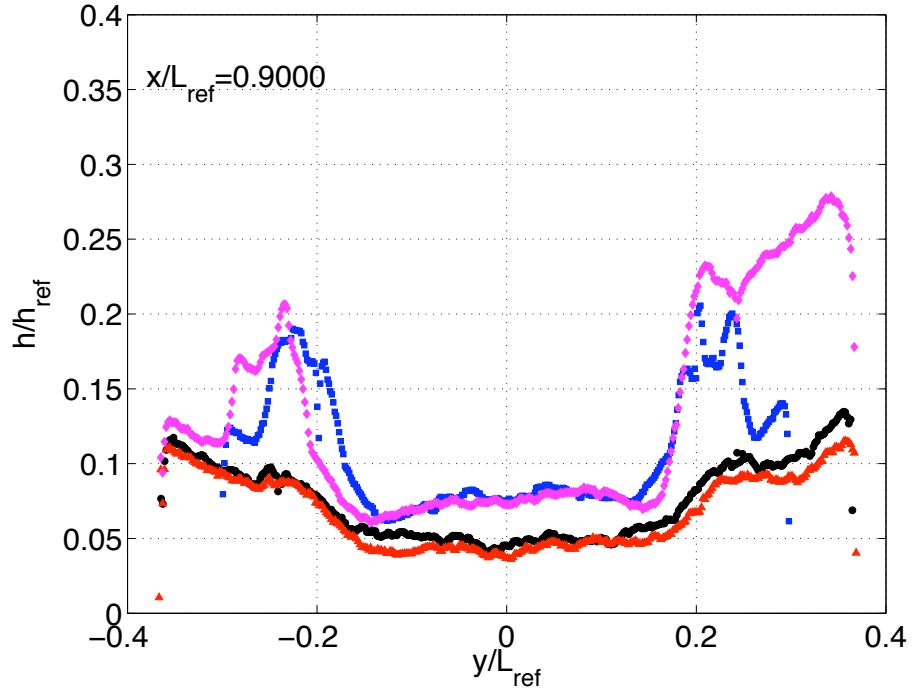


Figure 25. Spanwise line cuts of normalized heat-transfer measurements at $x/L_{ref} = 0.9$ for model 3 with three blank dowels and baseline model 1.

Type	x/L	y/L	k (in)
F(+45°)	0.50	-0.1008	0.007
PB	0.50	0	0.008
H	0.50	0.1008	0.007

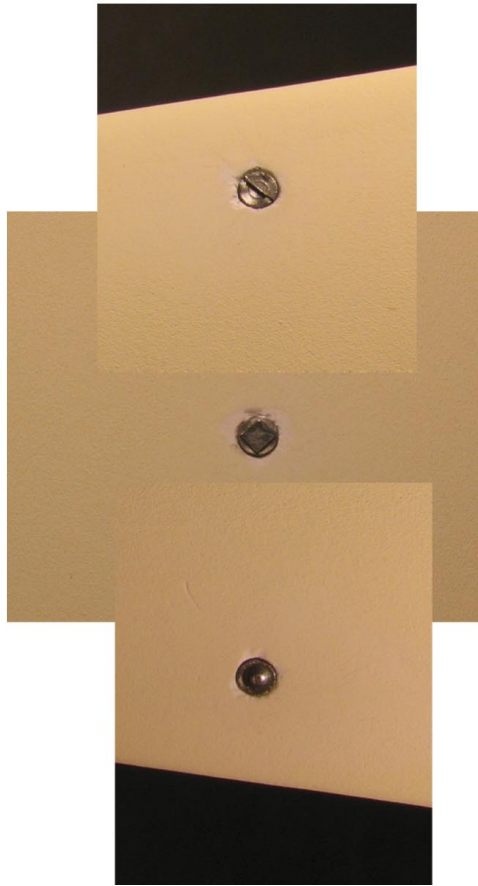


Figure 26. Close-up image of model 3 with configuration 5. Clockwise rotation of fence relative to model centerline is denoted as positive angle.

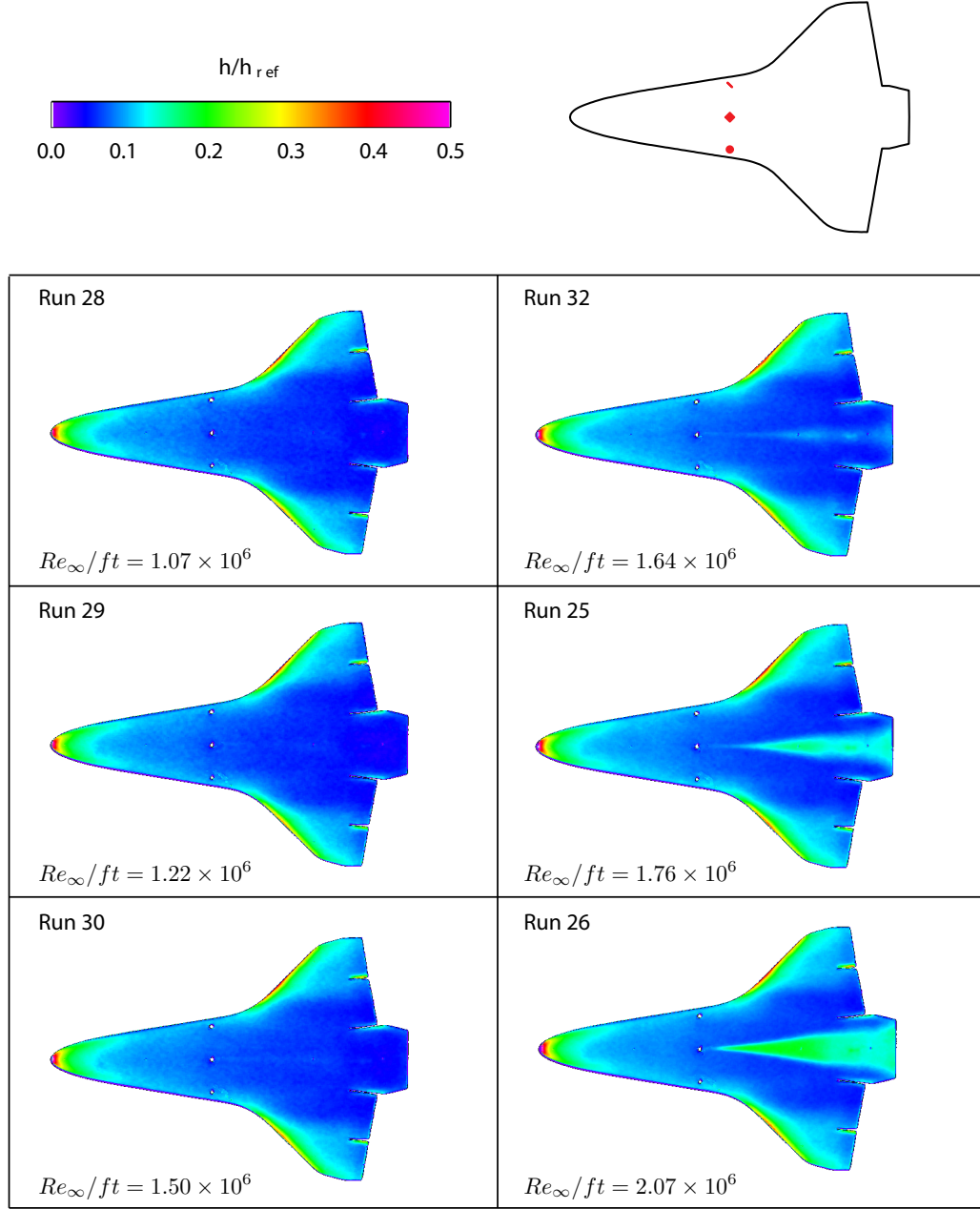


Figure 27. Global aeroheating images for model 3 with configuration 5.

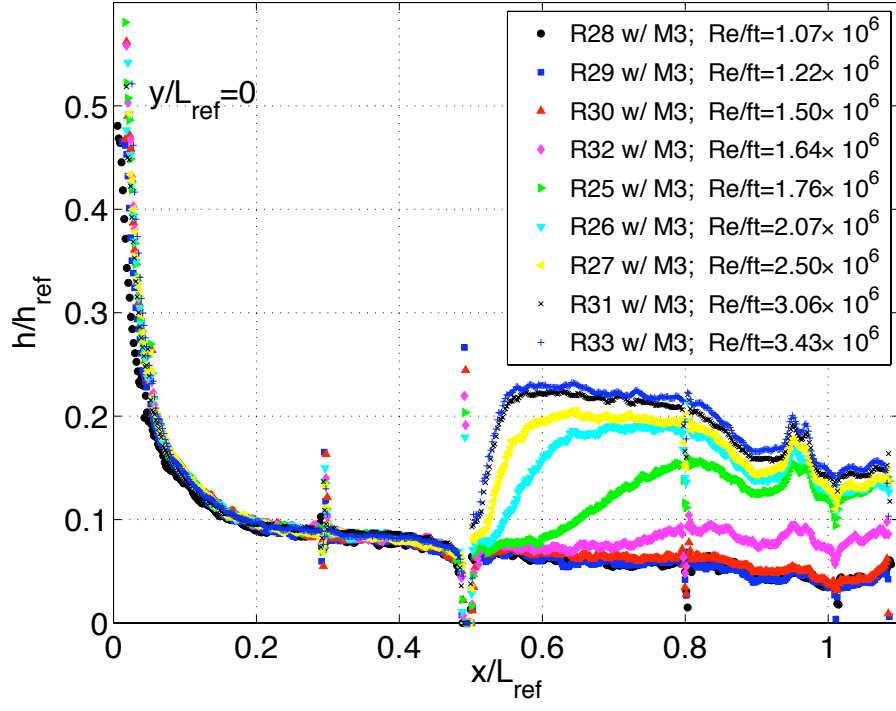


Figure 28. Streamwise line cuts of normalized heat-transfer measurements at $y/L_{ref} = 0$ for model 3 with configuration 5.

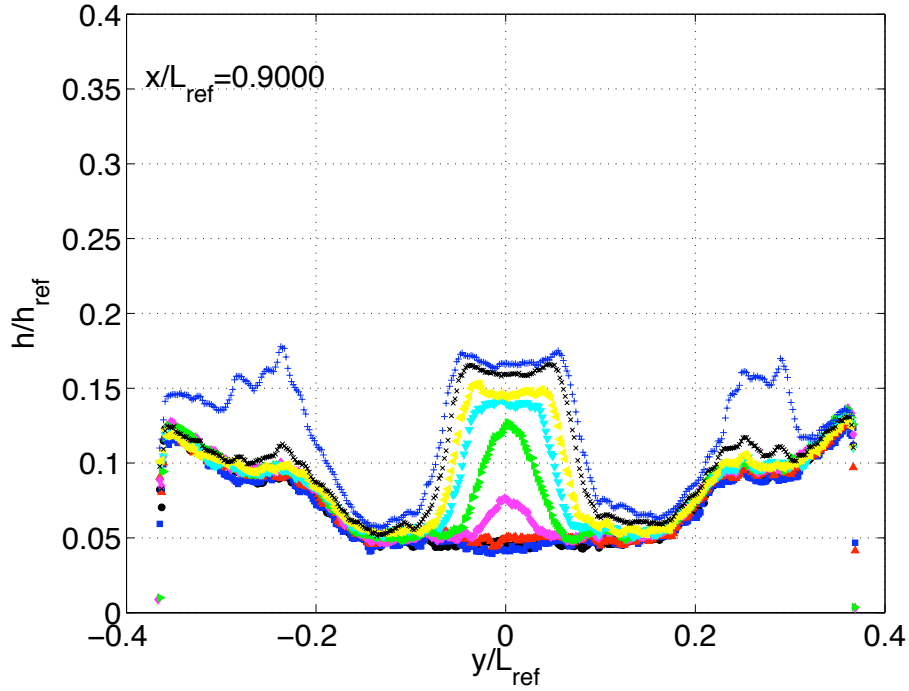


Figure 29. Spanwise line cuts of normalized heat-transfer measurements at $x/L_{ref} = 0.9$ for model 3 with configuration 5.

Type	x/L	y/L	k (in)
PB	0.50	-0.1008	0.008
F(+45°)	0.50	0	0.007
H	0.50	0.1008	0.007

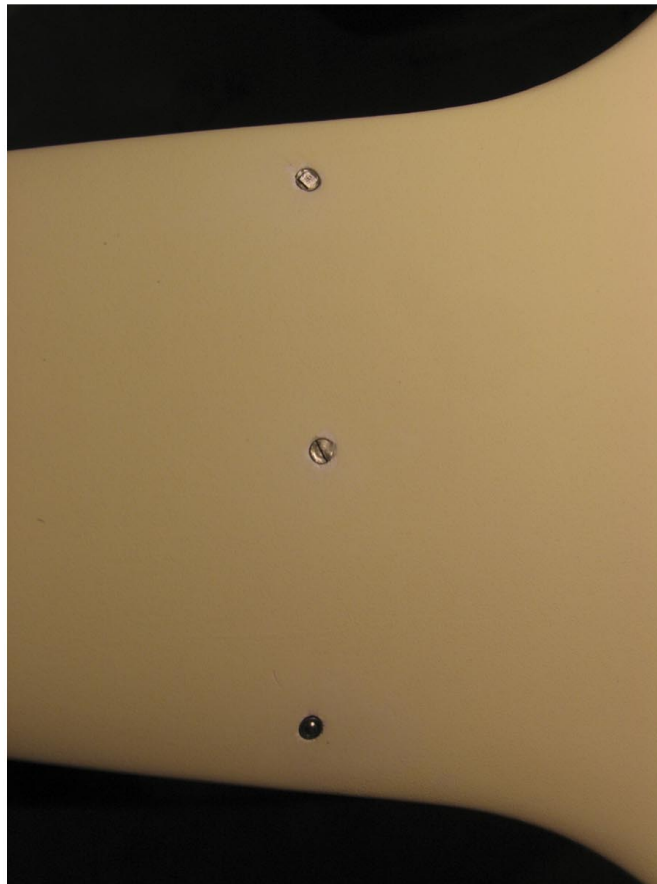


Figure 30. Close-up image of model 3 with configuration 5A. Clockwise rotation of fence relative to model centerline is denoted as positive angle.

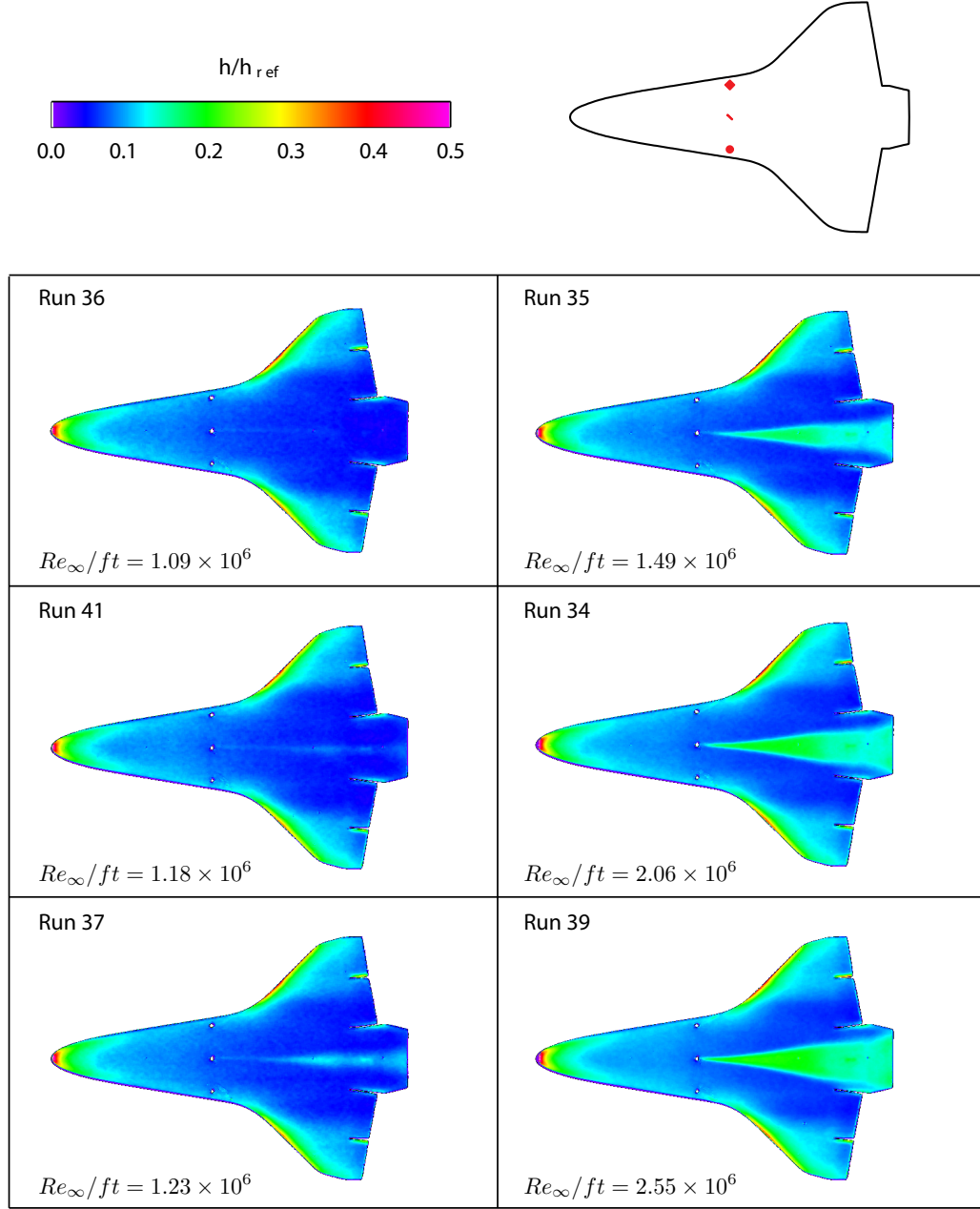


Figure 31. Global aeroheating images for model 3 with configuration 5A.

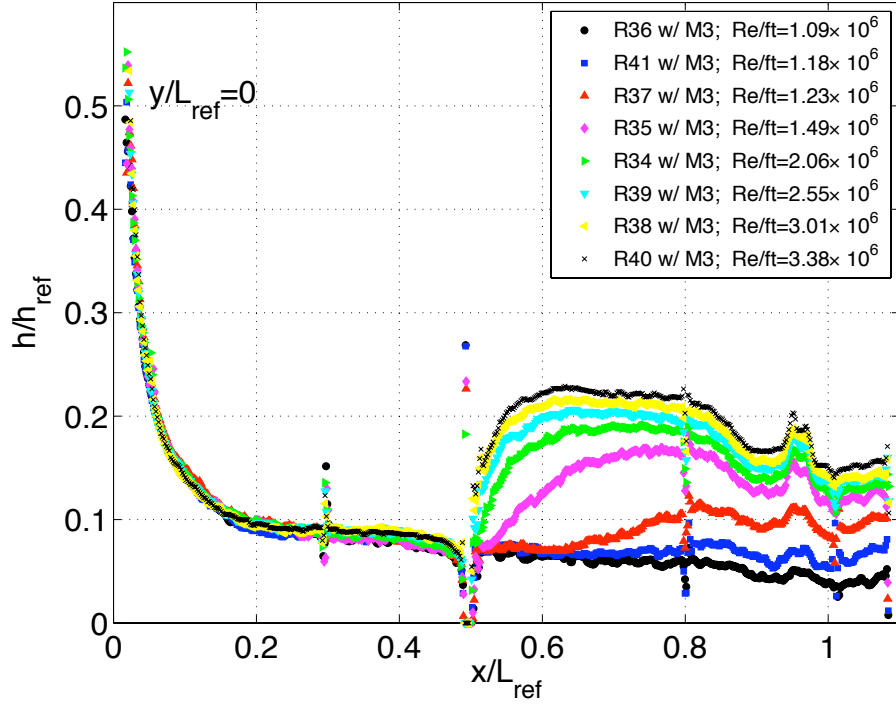


Figure 32. Streamwise line cuts of normalized heat-transfer measurements at $y/L_{ref} = 0$ for model 3 with configuration 5A.

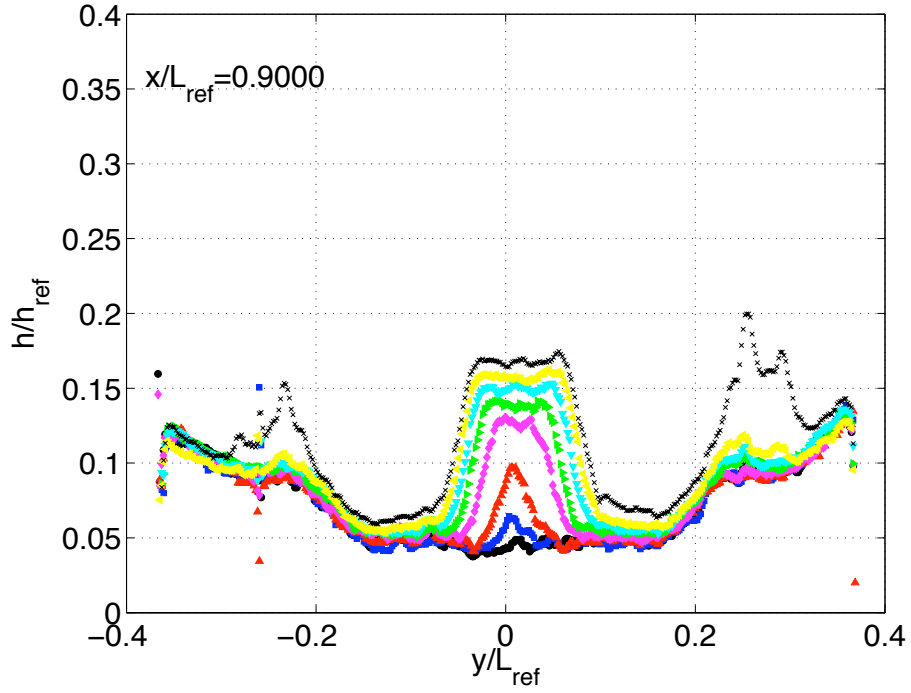


Figure 33. Spanwise line cuts of normalized heat-transfer measurements at $x/L_{ref} = 0.9$ for model 3 with configuration 5A.

Type	x/L	y/L	k (in)
PB	0.50	-0.1008	0.008
H	0.50	0	0.007
F(+45°)	0.50	0.1008	0.007

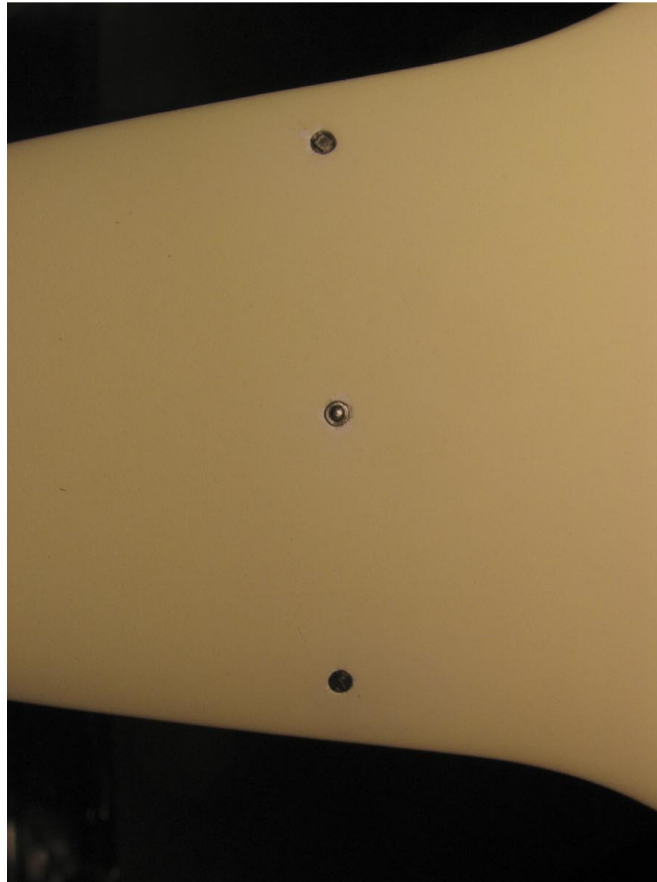


Figure 34. Close-up image of model 3 with configuration 5B. Clockwise rotation of fence relative to model centerline is denoted as positive angle.

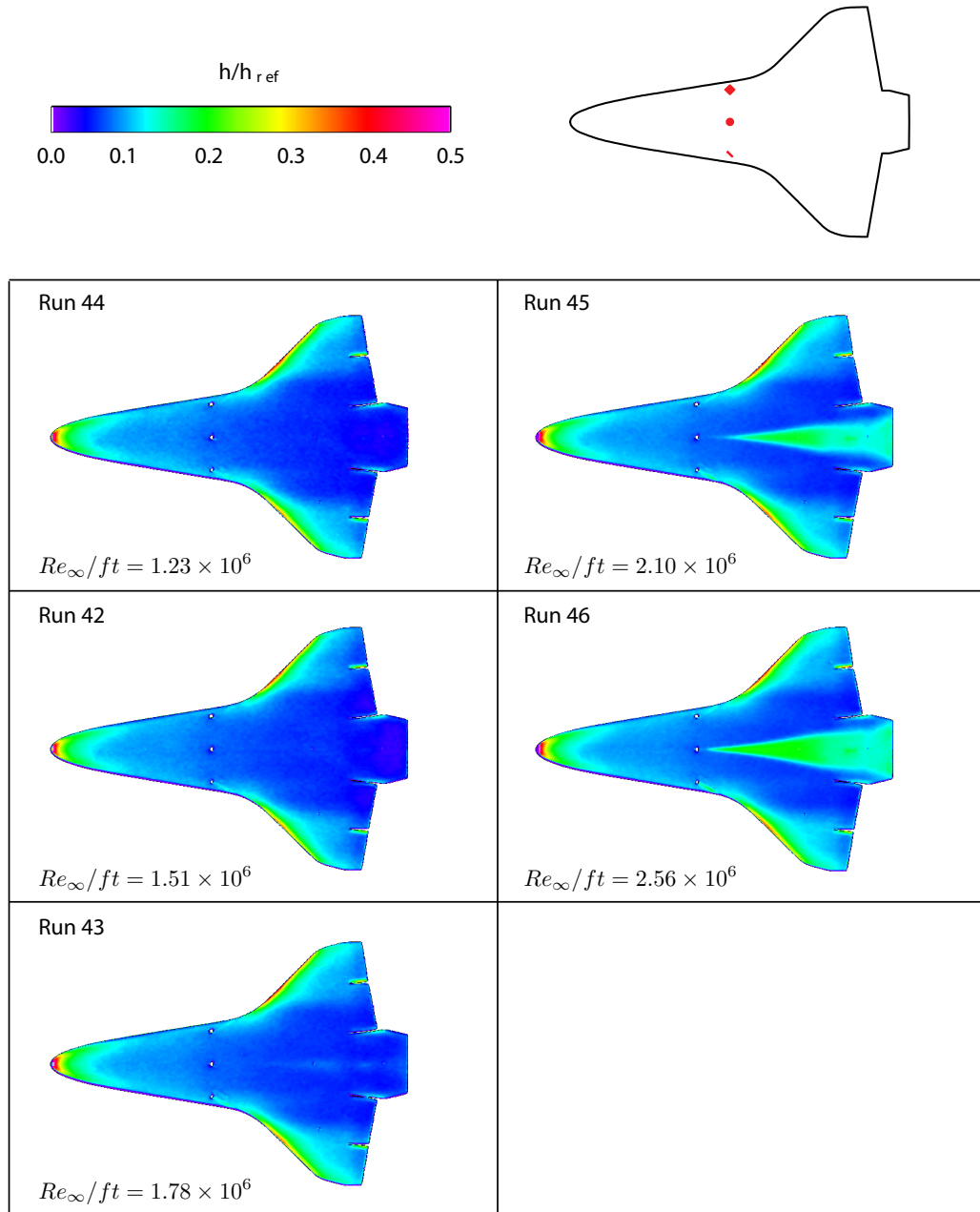


Figure 35. Global aeroheating images for model 3 with configuration 5B.

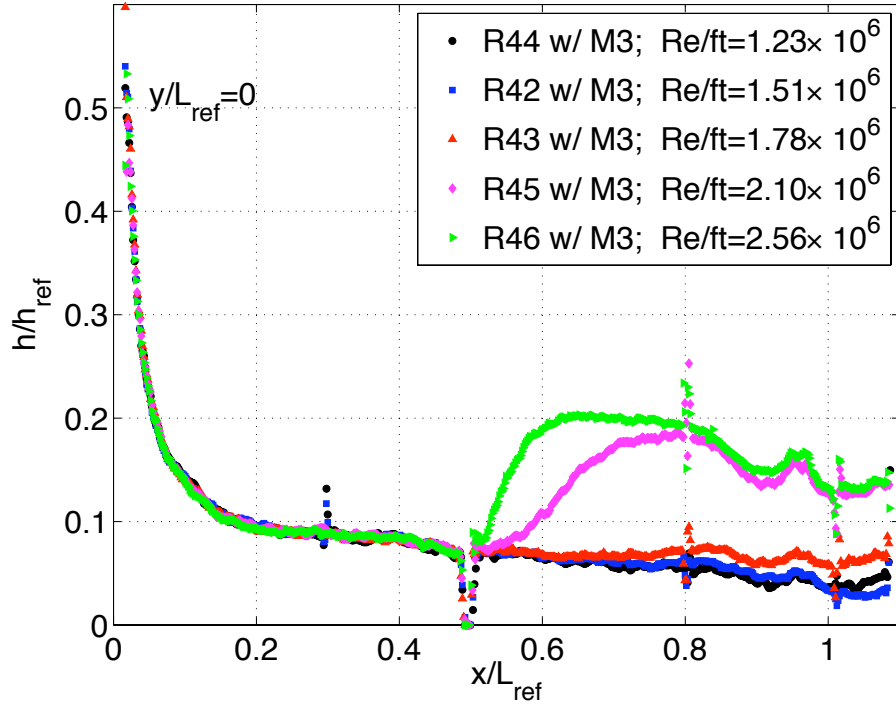


Figure 36. Streamwise line cuts of normalized heat-transfer measurements at $y/L_{ref} = 0$ for model 3 with configuration 5B.

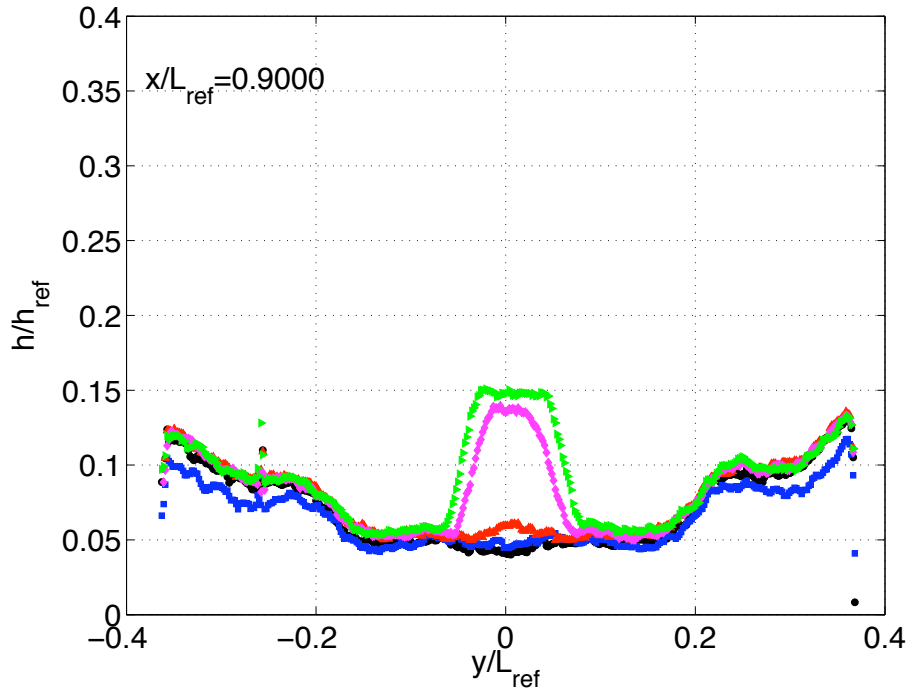


Figure 37. Spanwise line cuts of normalized heat-transfer measurements at $x/L_{ref} = 0.9$ for model 3 with configuration 5B.

Type	x/L	y/L
Blank	0.70	-0.1658
Blank	0.70	0
Blank	0.70	0.1658

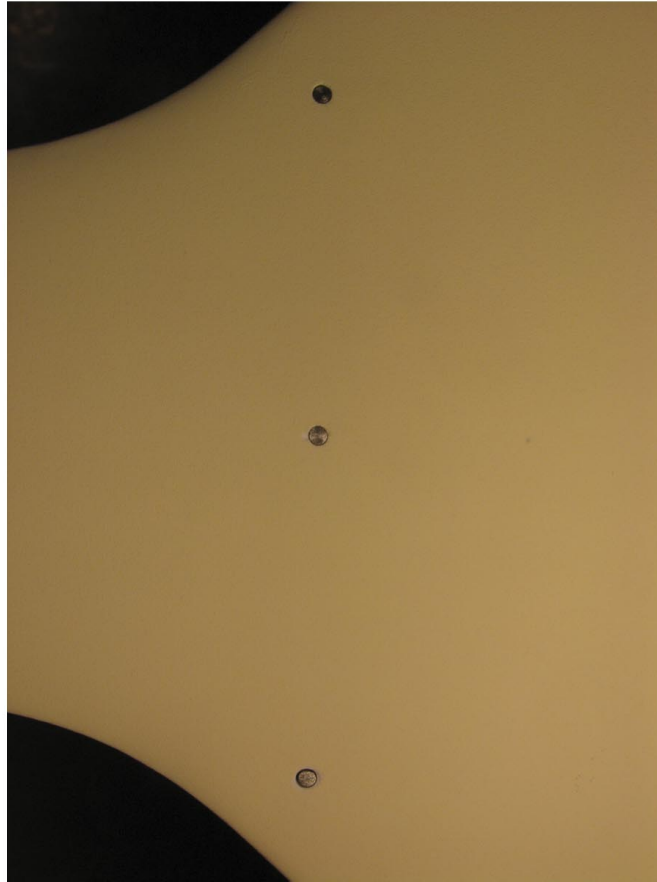


Figure 38. Close-up image of model 4 with three blank dowels installed.

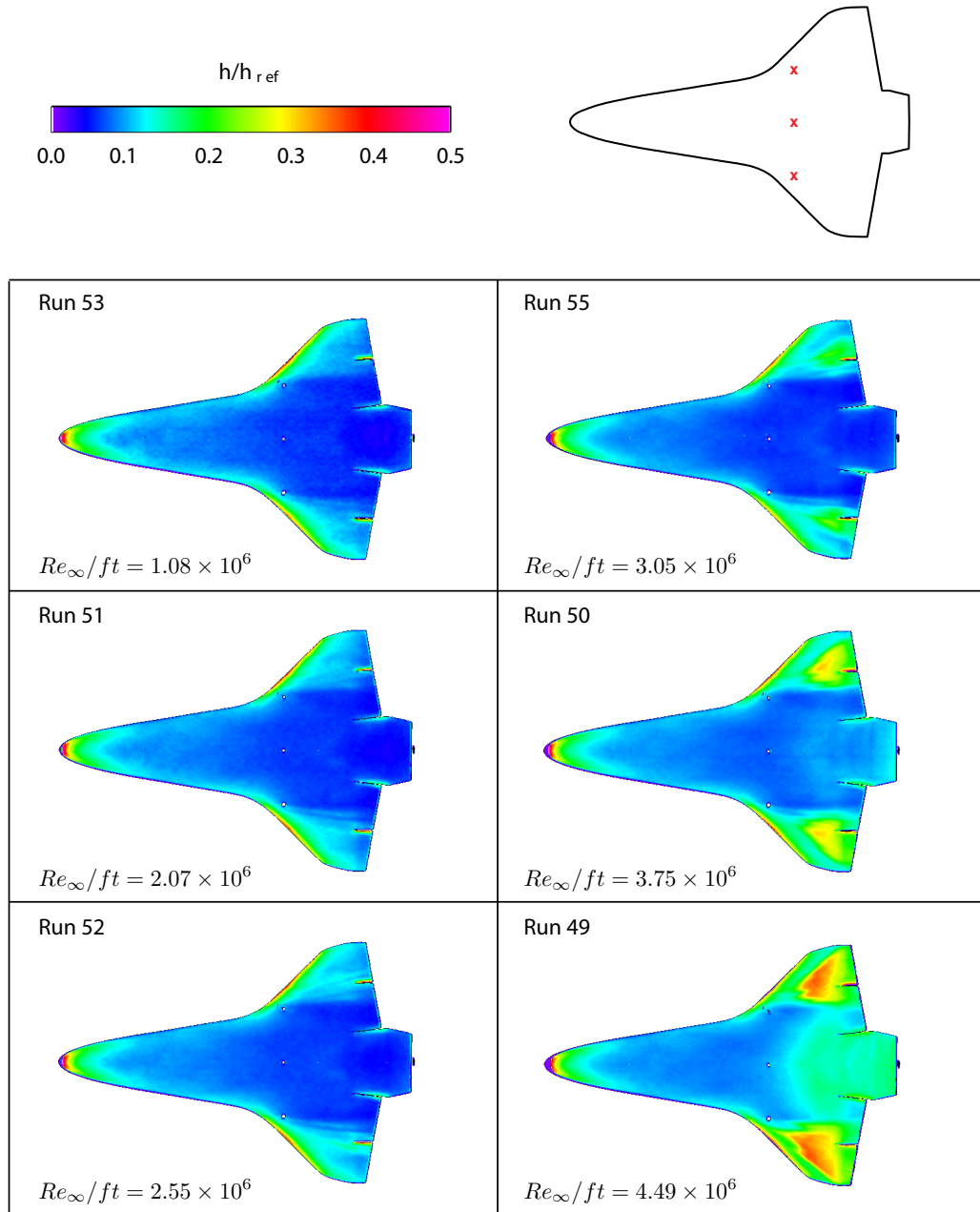


Figure 39. Global aeroheating images for model 4 with three blank dowels.

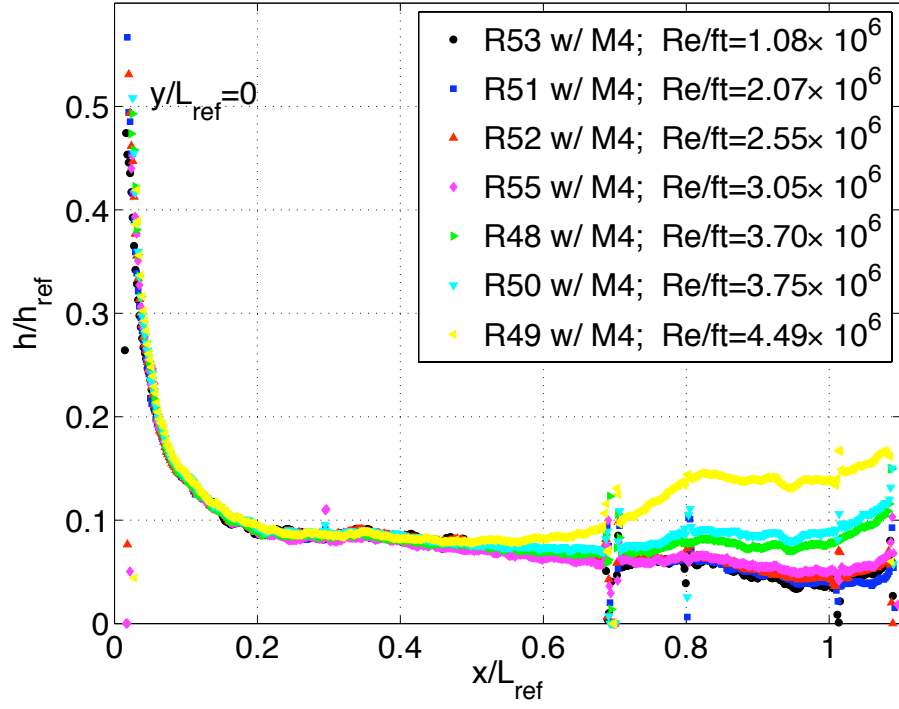


Figure 40. Streamwise line cuts of normalized heat-transfer measurements at $y/L_{ref} = 0$ for model 4 with three blank dowels.

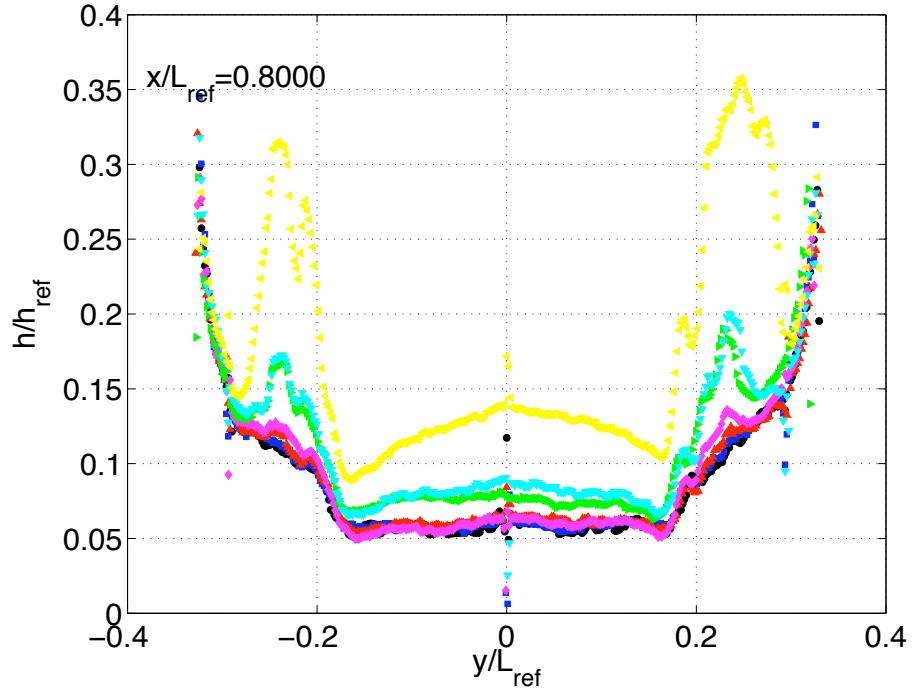


Figure 41. Spanwise line cuts of normalized heat-transfer measurements at $x/L_{ref} = 0.8$ for model 4 with three blank dowels

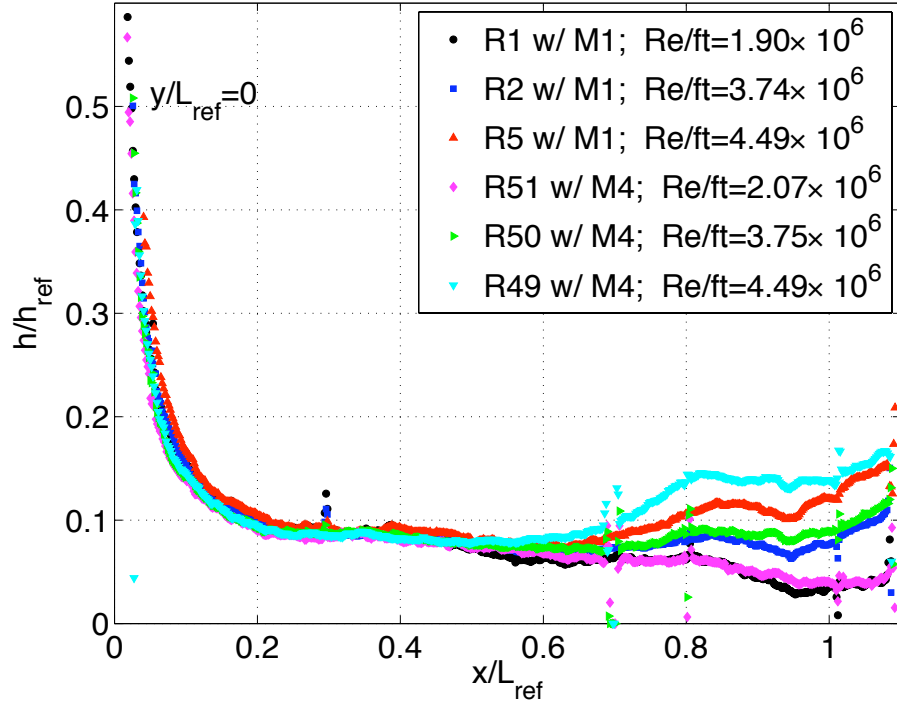


Figure 42. Streamwise line cuts of normalized heat-transfer measurements at $y/L_{ref} = 0$ for model 4 with three blank dowels and baseline model 1.

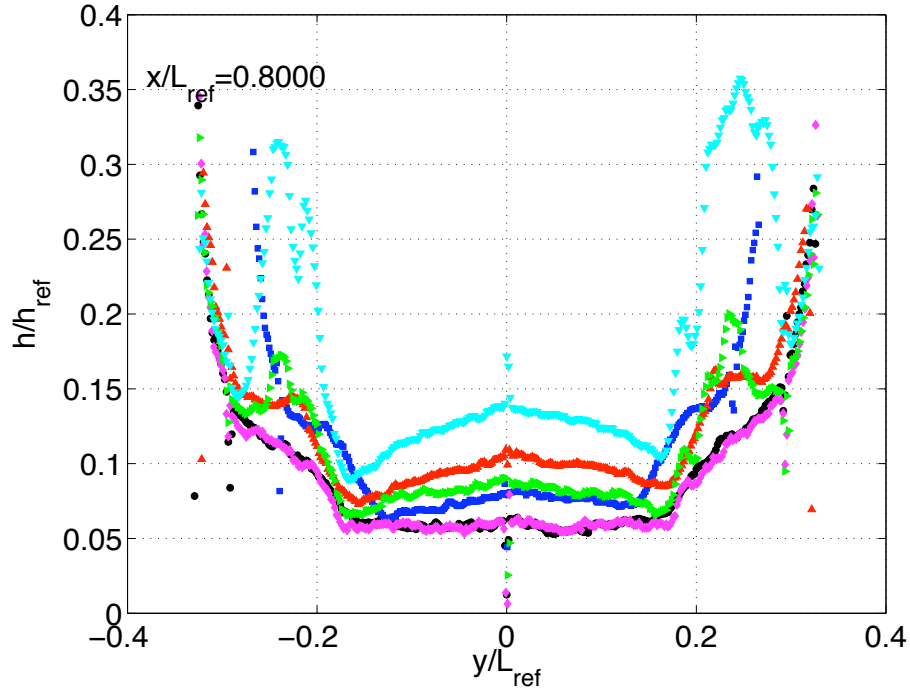


Figure 43. Spanwise line cuts of normalized heat-transfer measurements at $x/L_{ref} = 0.8$ for model 4 with three blank dowels and baseline model 1.

Type	x/L	y/L	k (in)
PB	0.70	-0.1658	0.008
F(+45°)	0.70	0	0.007
H	0.70	0.1658	0.007

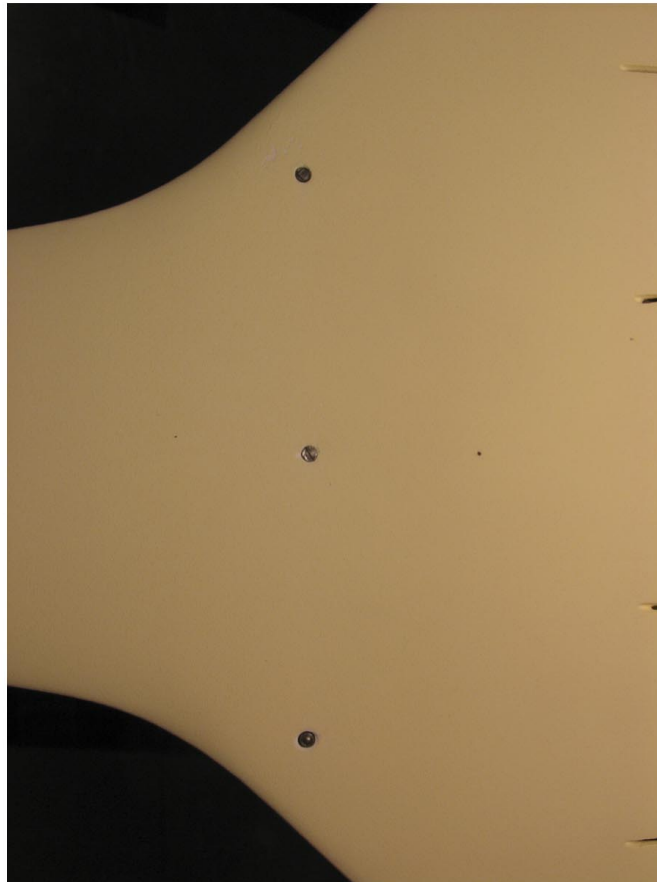


Figure 44. Close-up image of model 4 with configuration 6A. Clockwise rotation of fence relative to model centerline is denoted as positive angle.

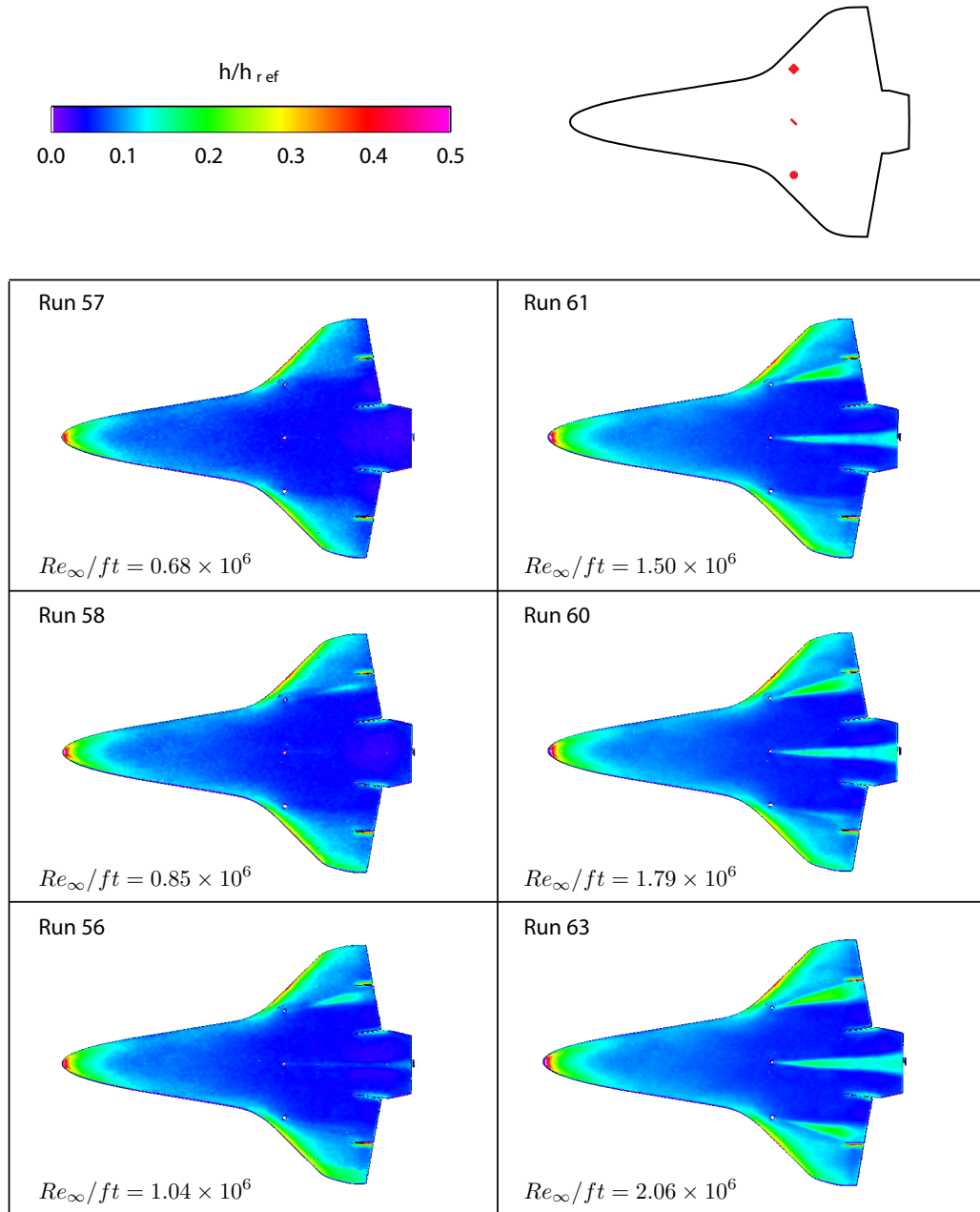


Figure 45. Global aeroheating images for model 4 with configuration 6A.

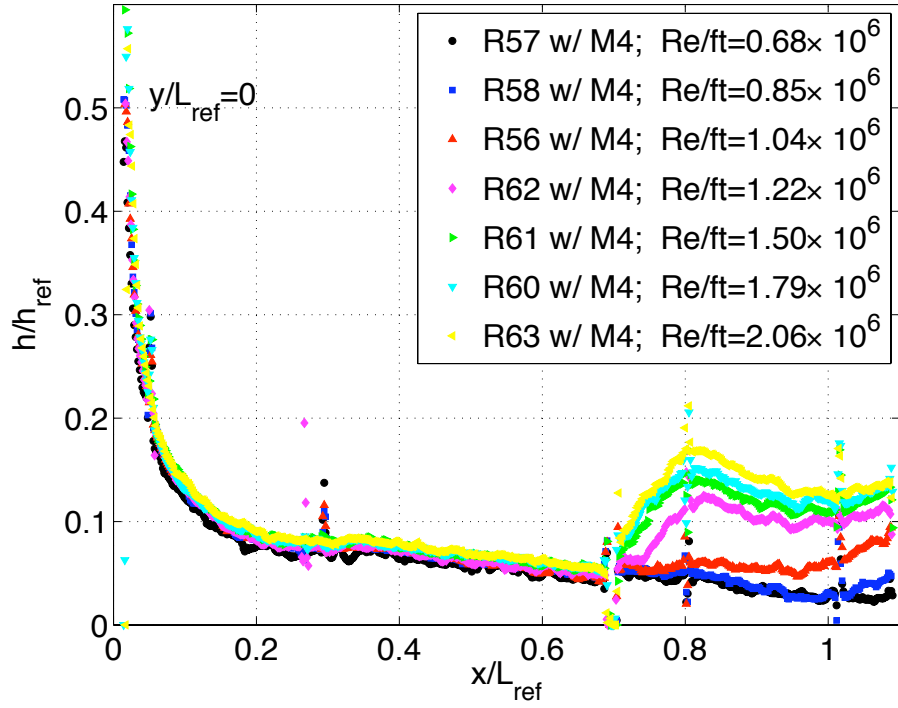


Figure 46. Streamwise line cuts of normalized heat-transfer measurements at $y/L_{ref} = 0$ for model 4 with configuration 6A.

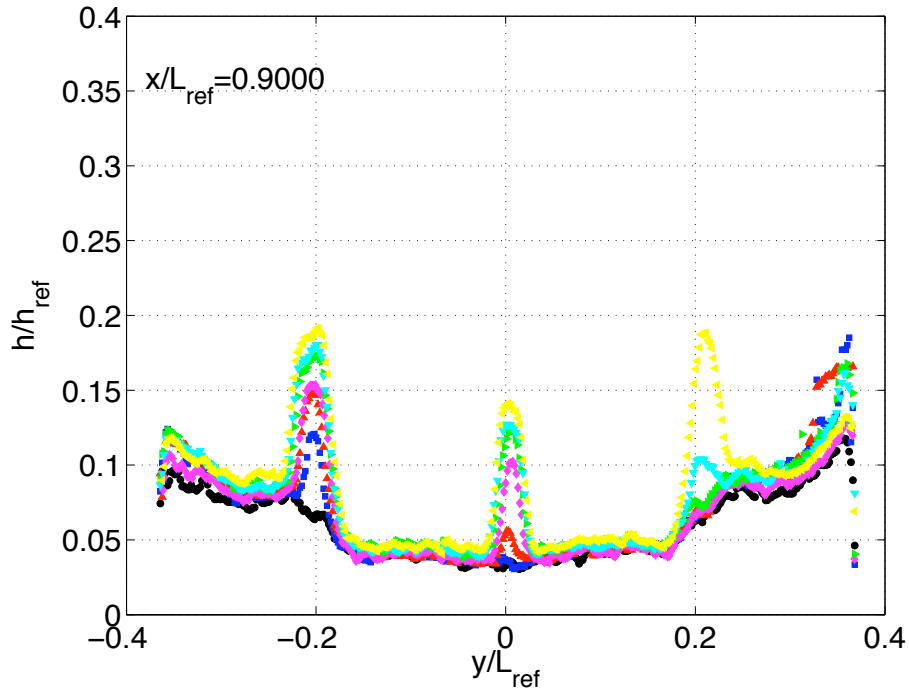


Figure 47. Spanwise line cuts of normalized heat-transfer measurements at $x/L_{ref} = 0.9$ for model 4 with configuration 6A.

Type	x/L	y/L	k (in)
PB(face @ 90°)	0.70	-0.1658	0.008
F(90°)	0.70	0	0.007
AF(90°)*	0.70	0.1658	0.006/0.004

* Highest edge of angled fence, AF, outboard.

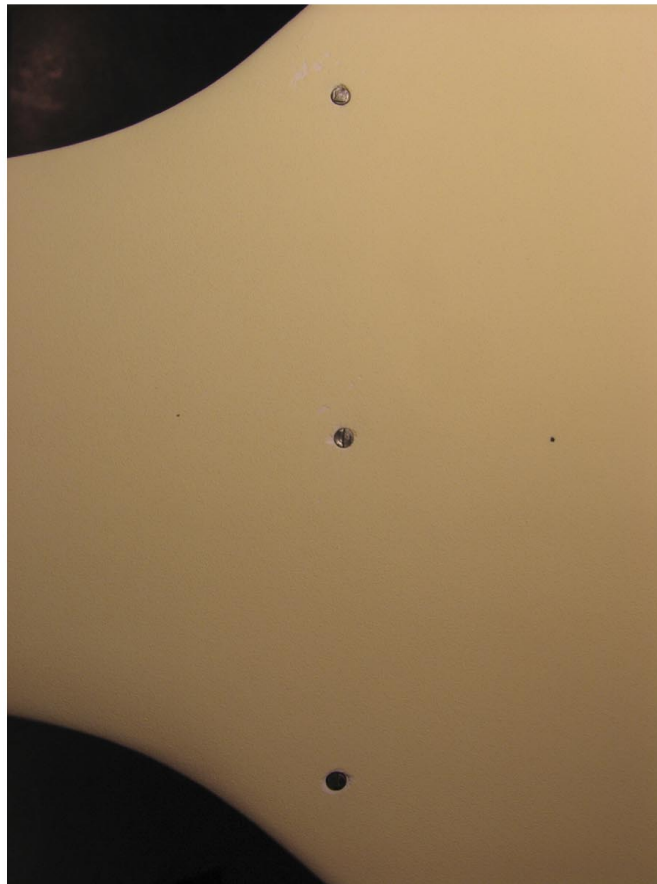


Figure 48. Close-up image of model 4 with configuration 6B. Diagonal of PB trip is at 45° from model centerline.

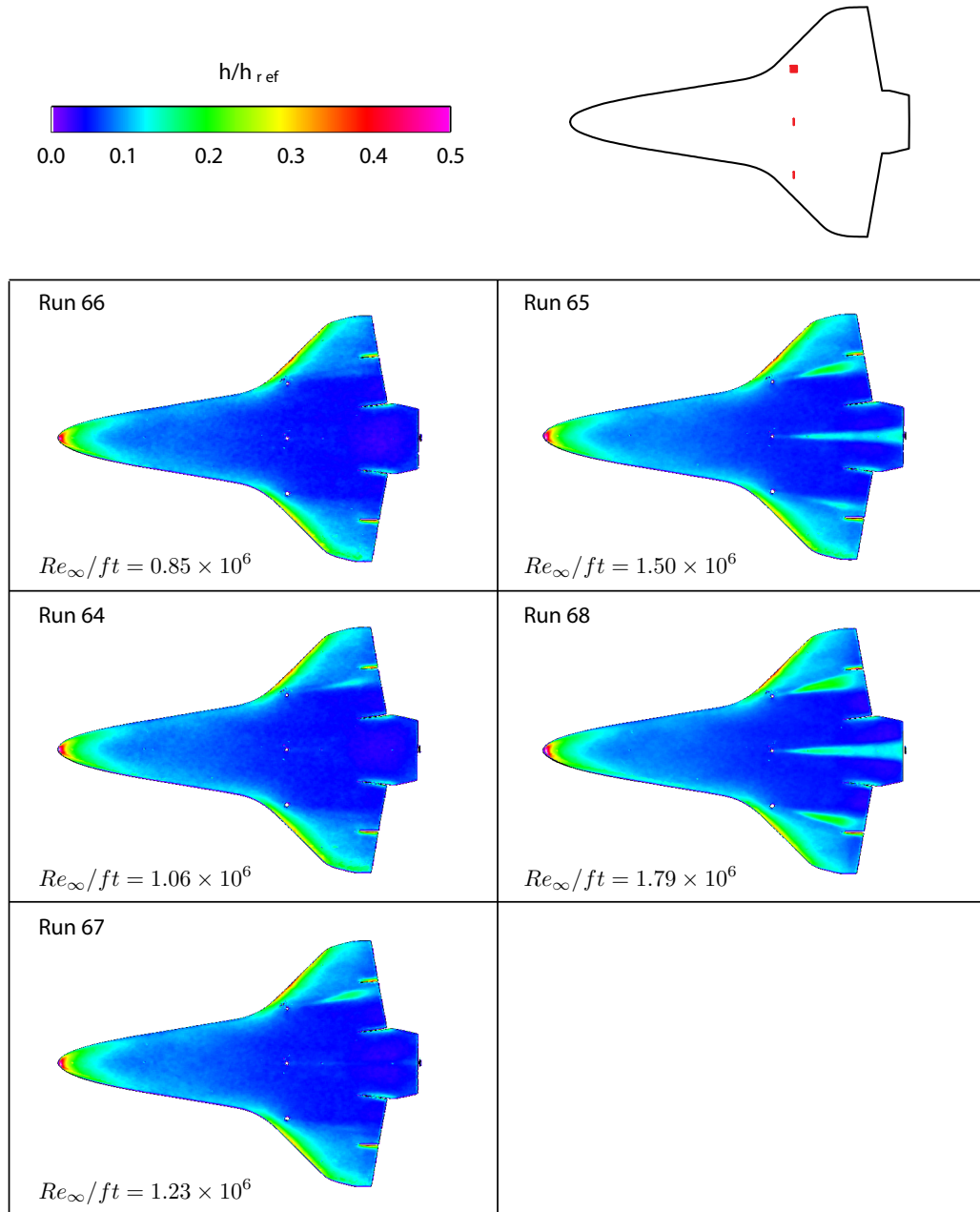


Figure 49. Global aeroheating images for model 4 with configuration 6B.

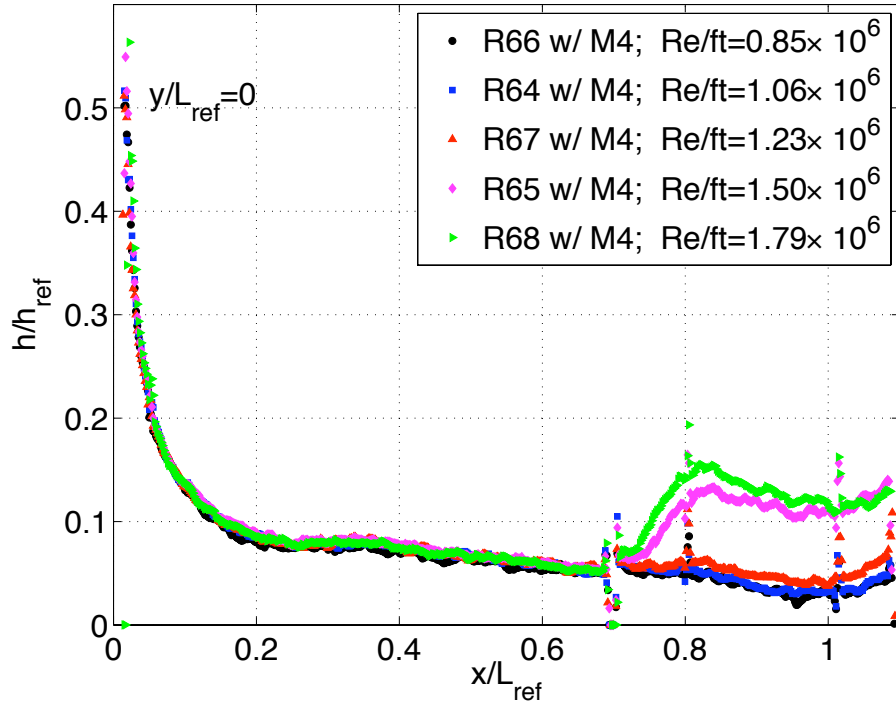


Figure 50. Streamwise line cuts of normalized heat-transfer measurements at $y/L_{ref} = 0$ for model 4 with configuration 6B.

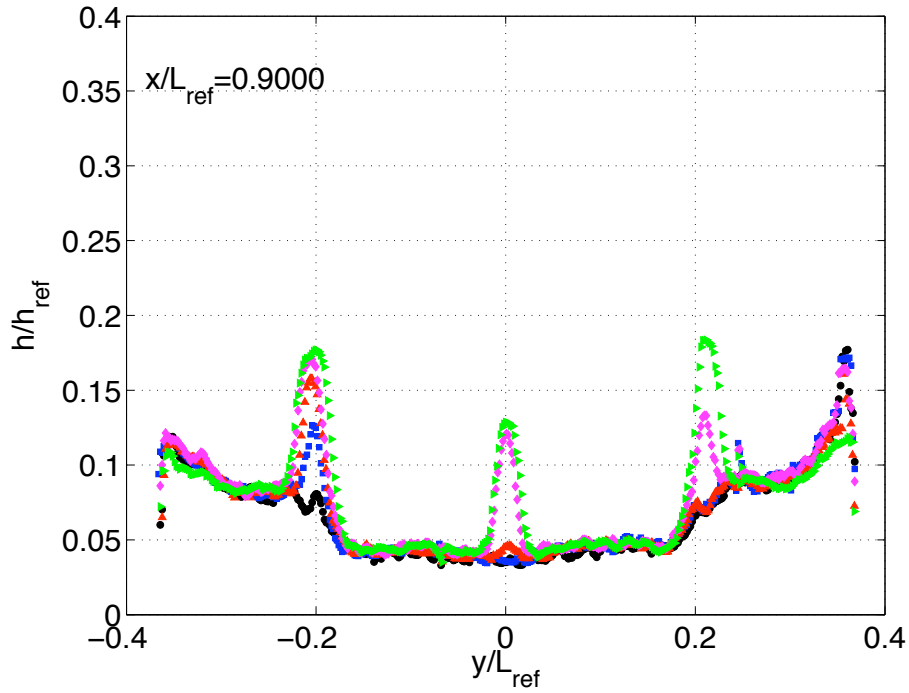


Figure 51. Spanwise line cuts of normalized heat-transfer measurements at $x/L_{ref} = 0.9$ for model 4 with configuration 6B.

Type	x/L	y/L	k (in)
PB(outboard face @ $\sim 22.5^\circ$)	0.70	-0.1658	0.008
F(0°)	0.70	0	0.007
AF(0°)*	0.70	0.1658	0.006/0.004

* Highest edge of angled fence, AF, upstream.

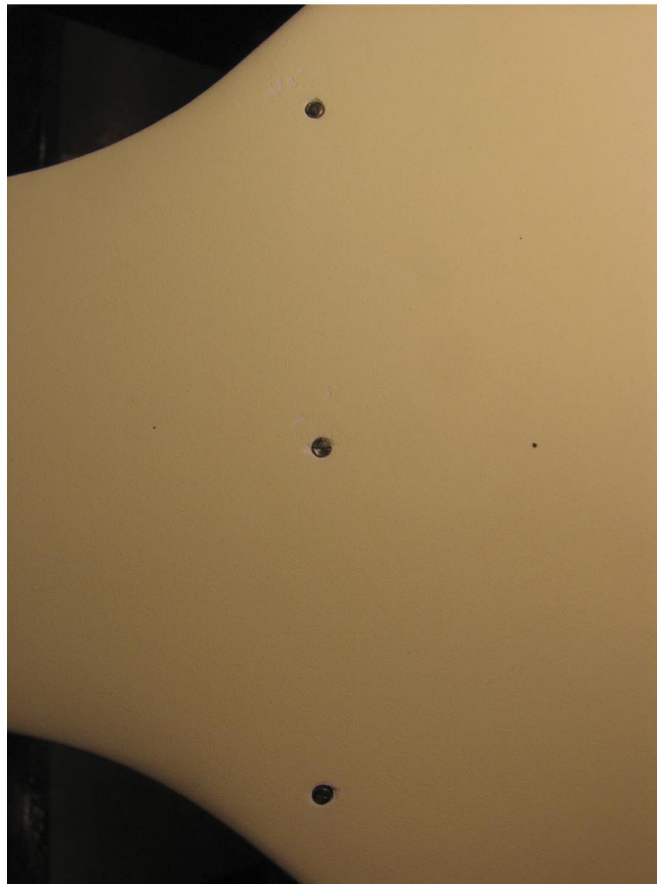


Figure 52. Close-up image of model 4 with configuration 6C. Diagonal of PB trip is approximately -22.5° from model centerline.

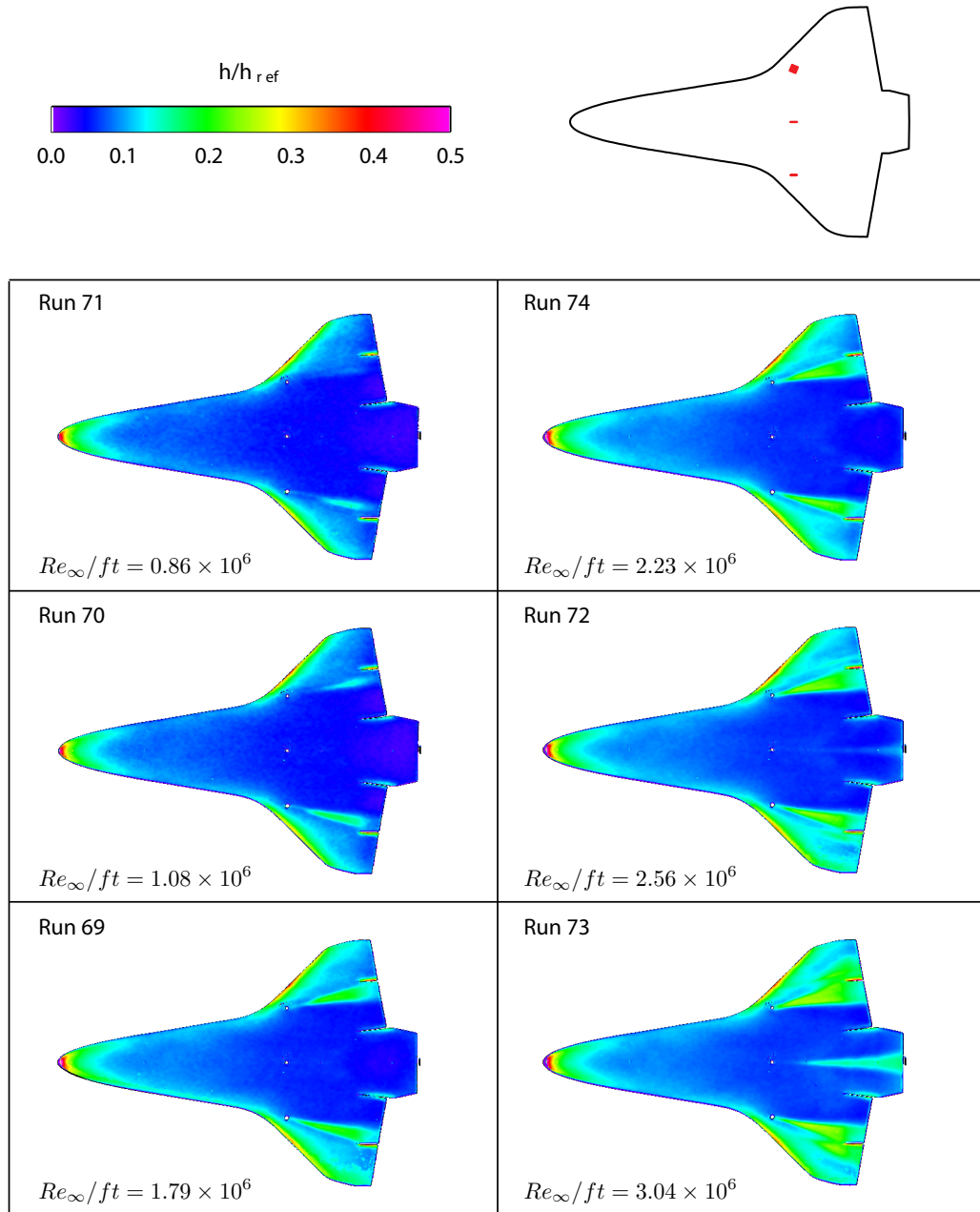


Figure 53. Global aeroheating images for model 4 with configuration 6C.

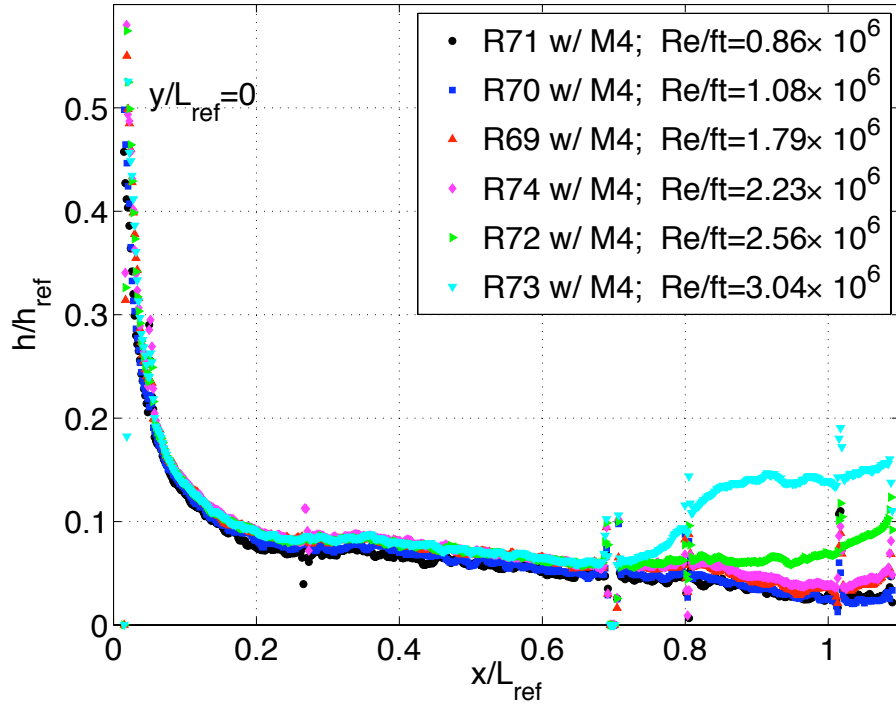


Figure 54. Streamwise line cuts of normalized heat-transfer measurements at $y/L_{ref} = 0$ for model 4 with configuration 6C.

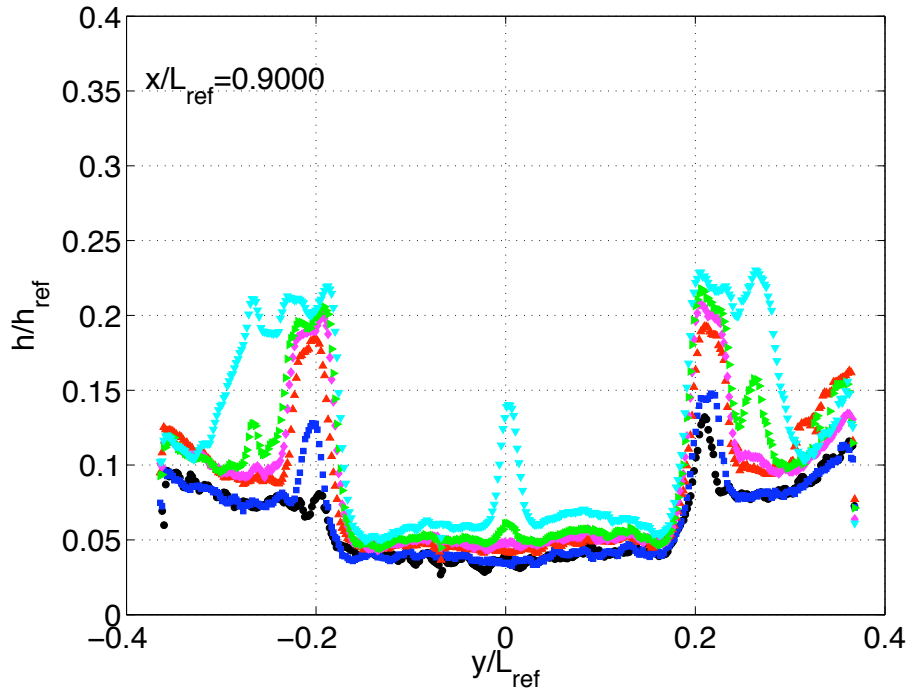


Figure 55. Spanwise line cuts of normalized heat-transfer measurements at $x/L_{ref} = 0.9$ for model 4 with configuration 6C.

Type	x/L	y/L
Blank	0.85	0

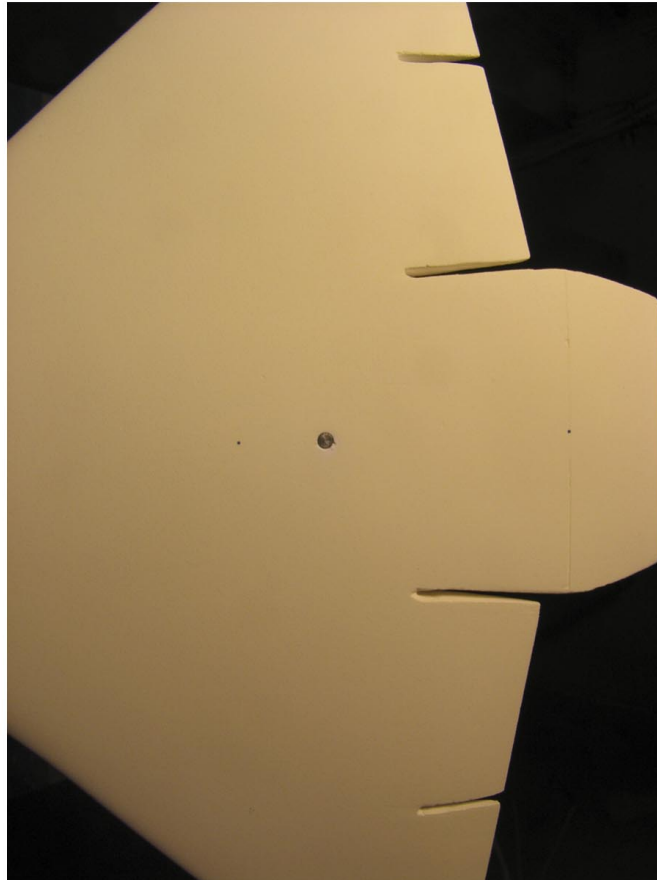


Figure 56. Close-up image of model 6 with a blank dowel installed.

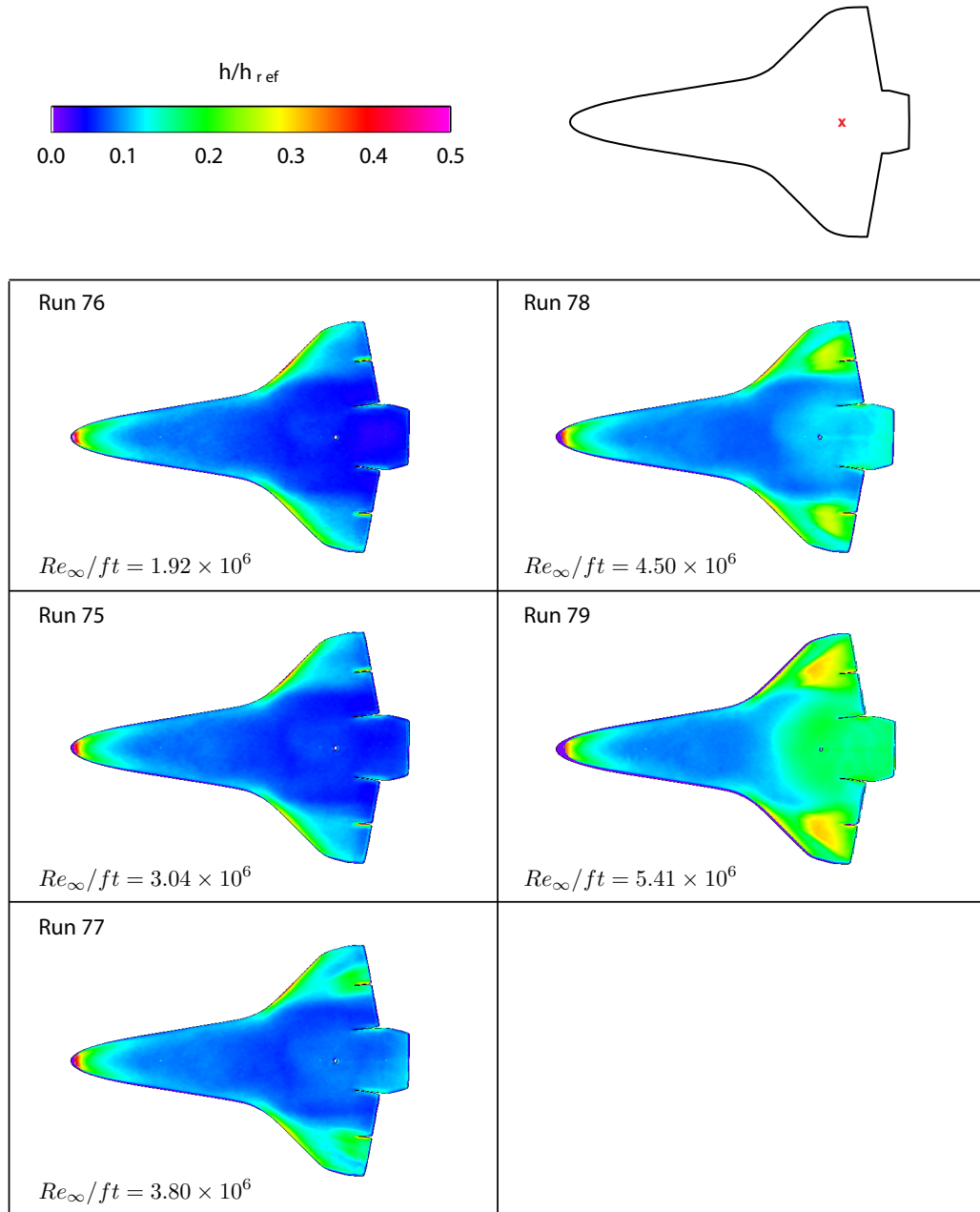


Figure 57. Global aeroheating images for model 6 with a blank dowel.

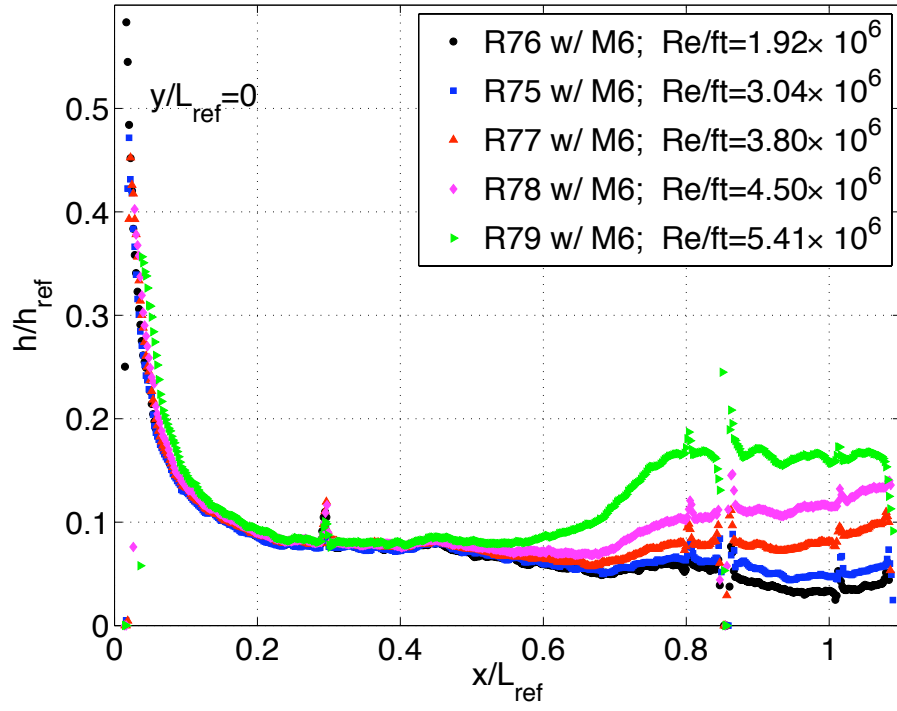


Figure 58. Streamwise line cuts of normalized heat-transfer measurements at $y/L_{ref} = 0$ for model 6 with a blank dowel.

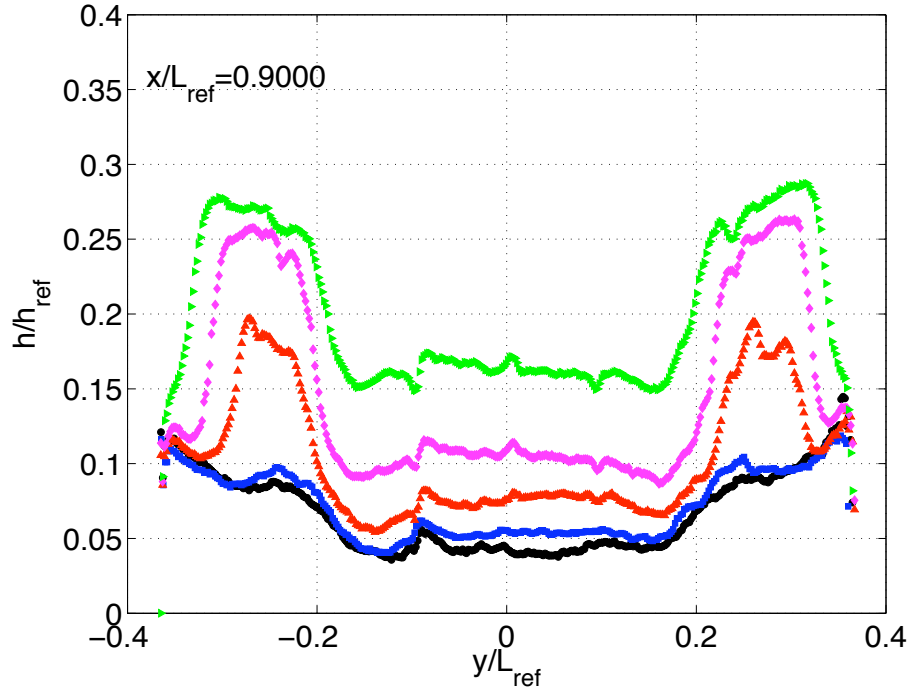


Figure 59. Spanwise line cuts of normalized heat-transfer measurements at $x/L_{ref} = 0.9$ for model 6 with a blank dowel.

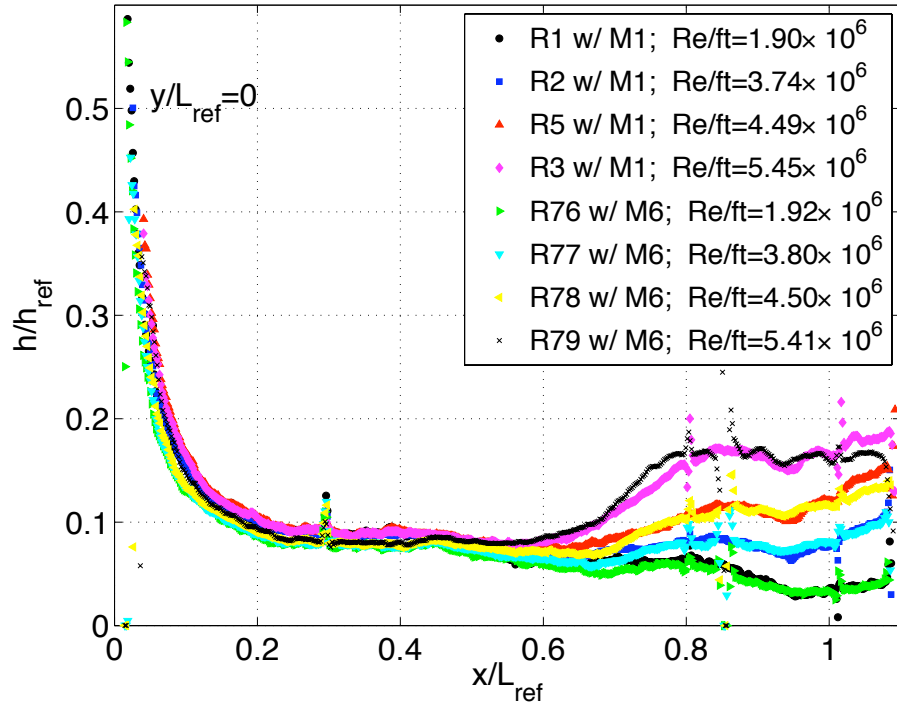


Figure 60. Streamwise line cuts of normalized heat-transfer measurements at $y/L_{ref} = 0$ for model 6 with a blank dowel and baseline model 1.

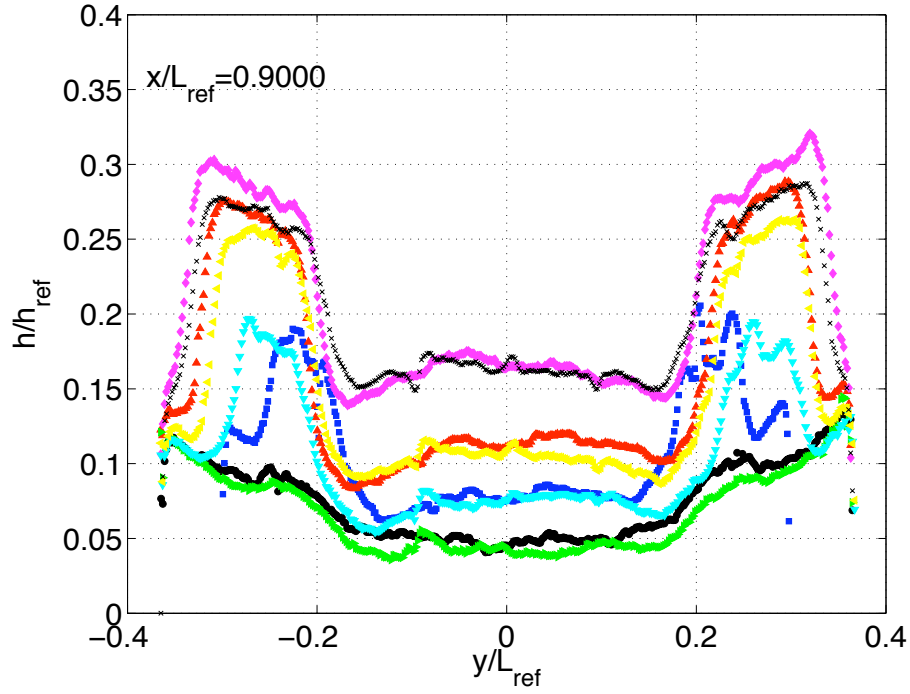


Figure 61. Spanwise line cuts of normalized heat-transfer measurements at $x/L_{ref} = 0.8$ for model 6 with a blank dowel and baseline model 1.

Type	x/L	y/L	k (in)
F(+45°)	0.85	0	0.011

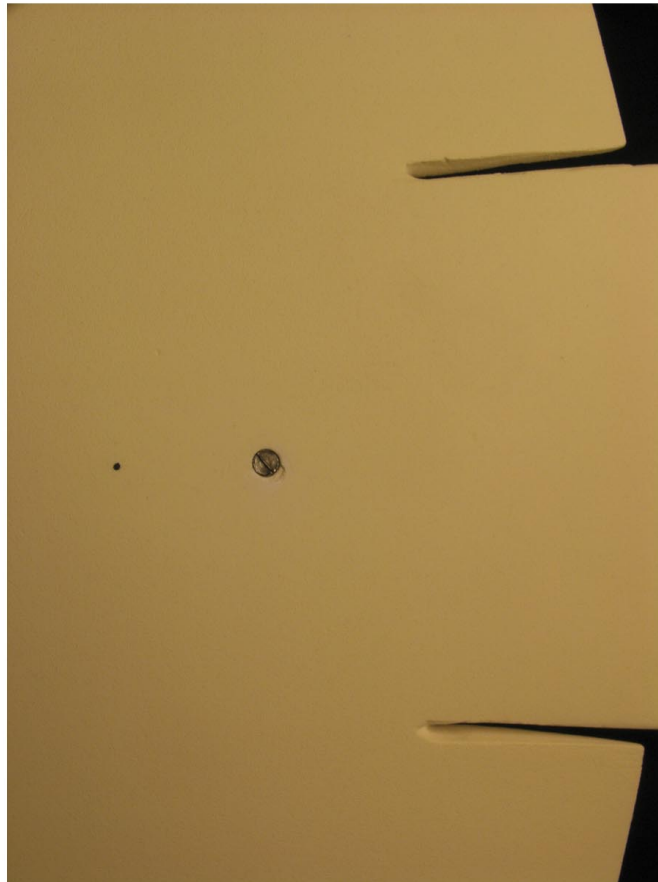


Figure 62. Close-up image of model 6 with configuration 12.

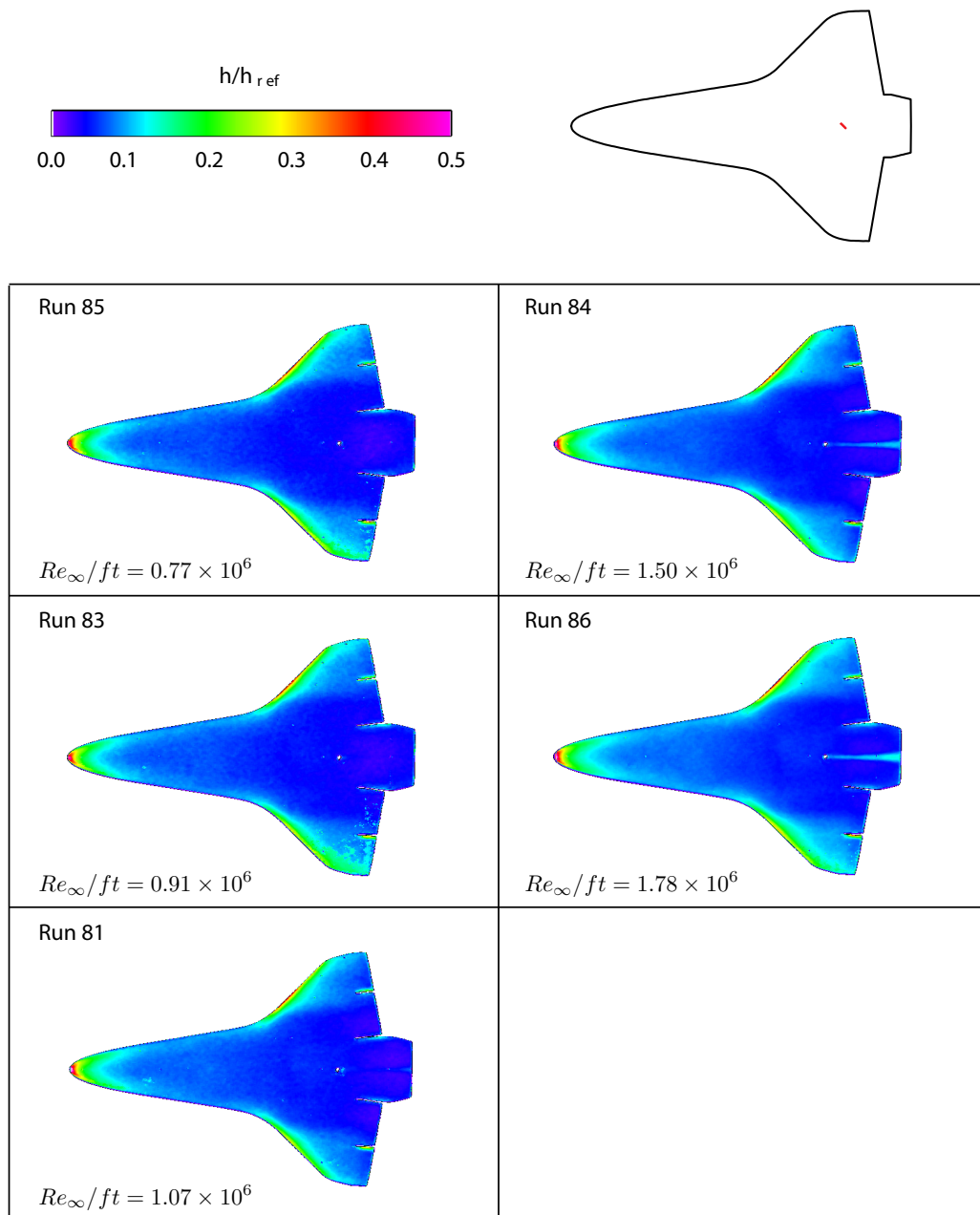


Figure 63. Global aeroheating images for model 6 with configuration 12.

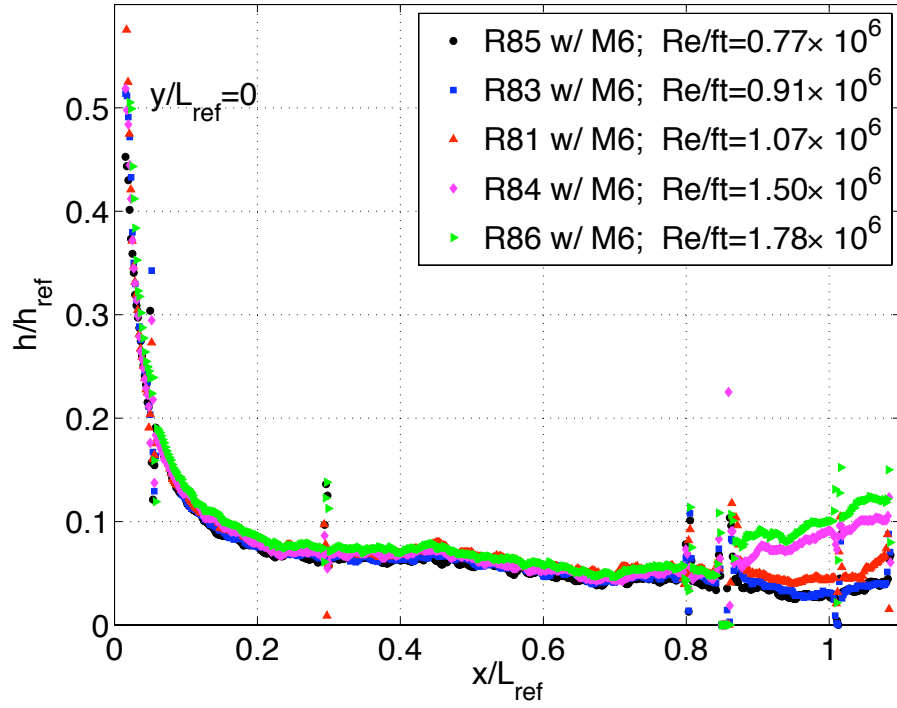


Figure 64. Streamwise line cuts of normalized heat-transfer measurements at $y/L_{ref} = 0$ for model 6 with configuration 12.

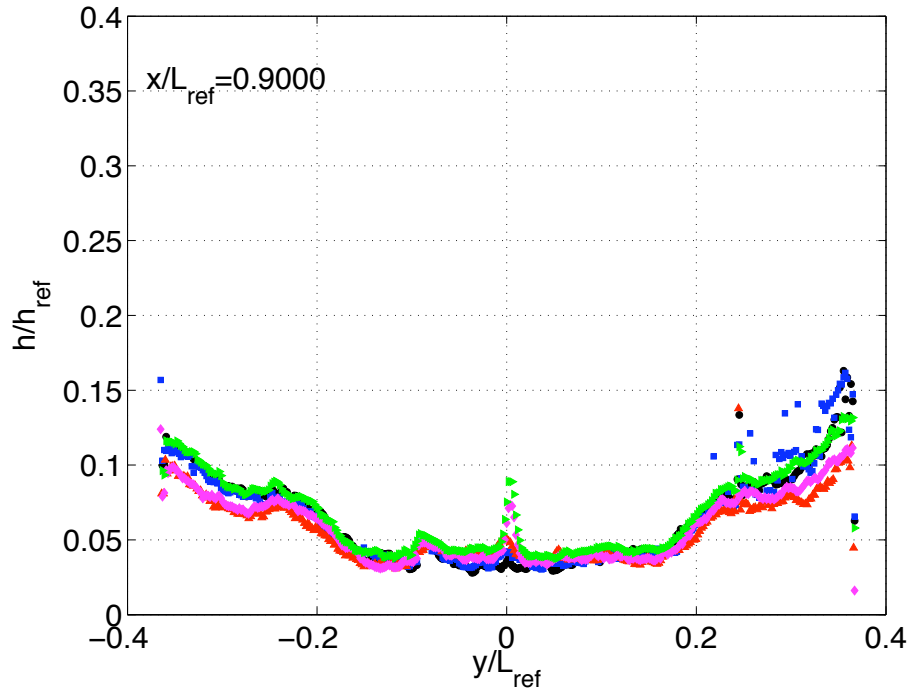


Figure 65. Spanwise line cuts of normalized heat-transfer measurements at $x/L_{ref} = 0.9$ for model 6 with configuration 12.

Type	x/L	y/L	k (in)
PB	0.85	0	0.010

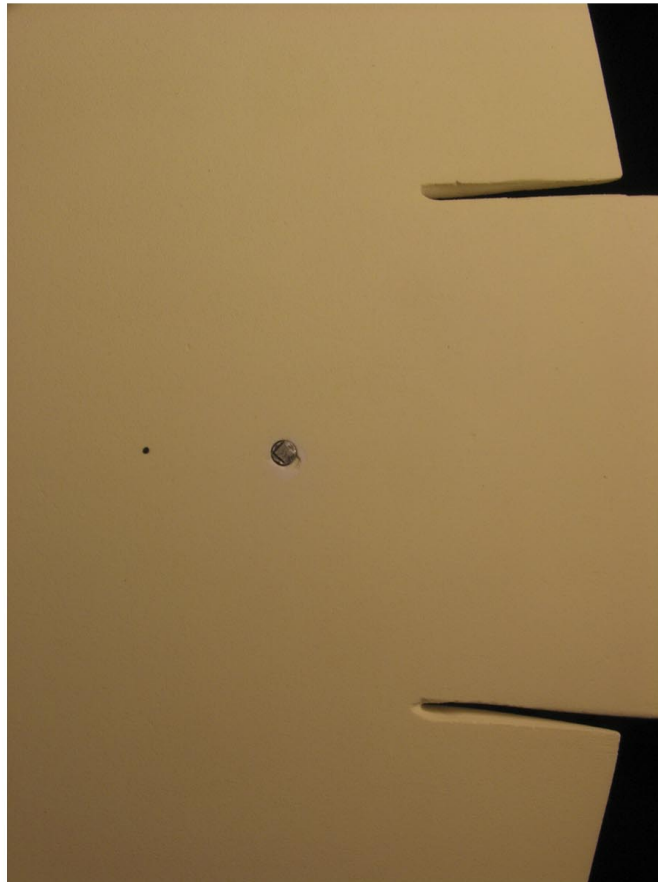


Figure 66. Close-up image of model 6 with configuration 12B.

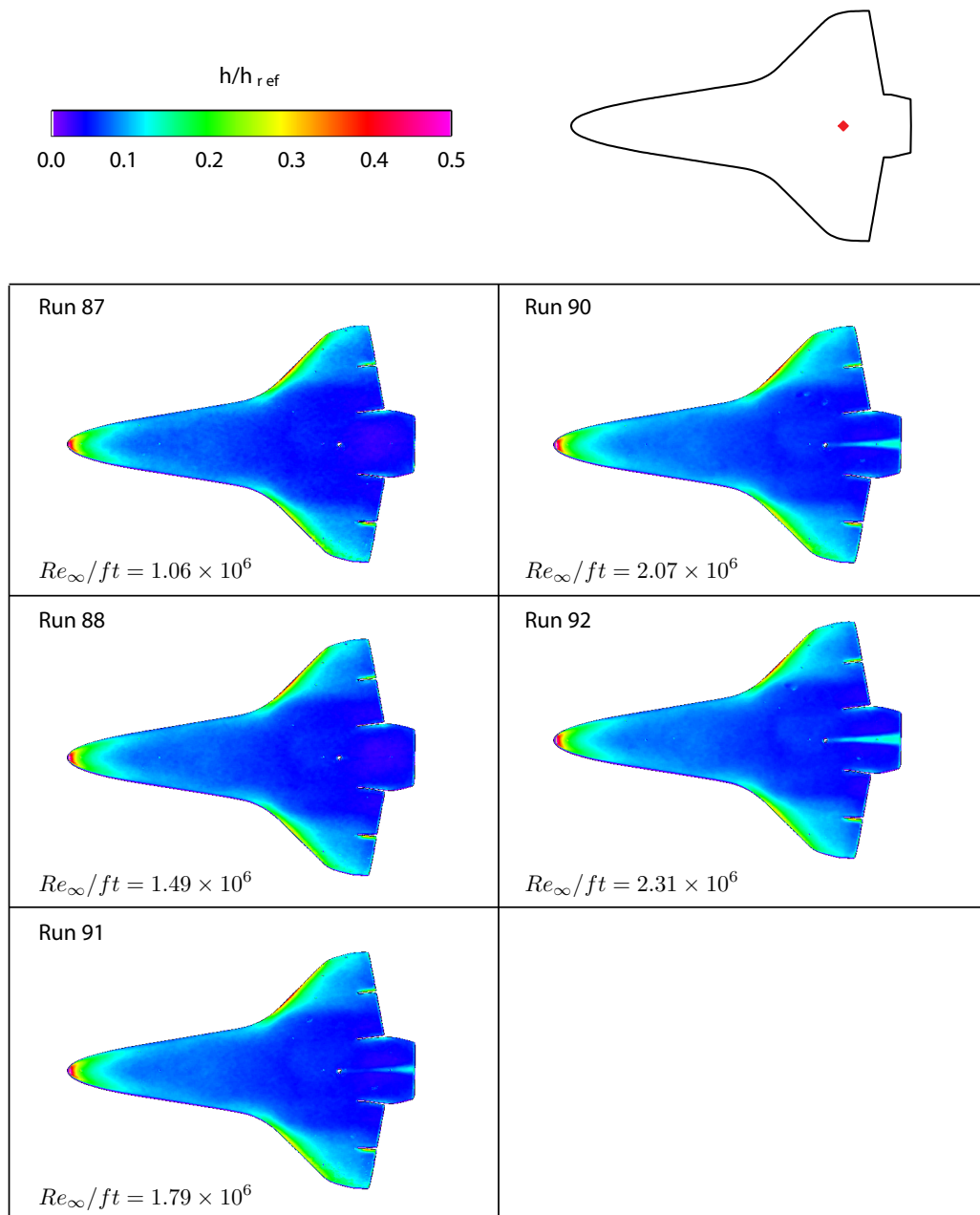


Figure 67. Global aeroheating images for model 6 with configuration 12B.

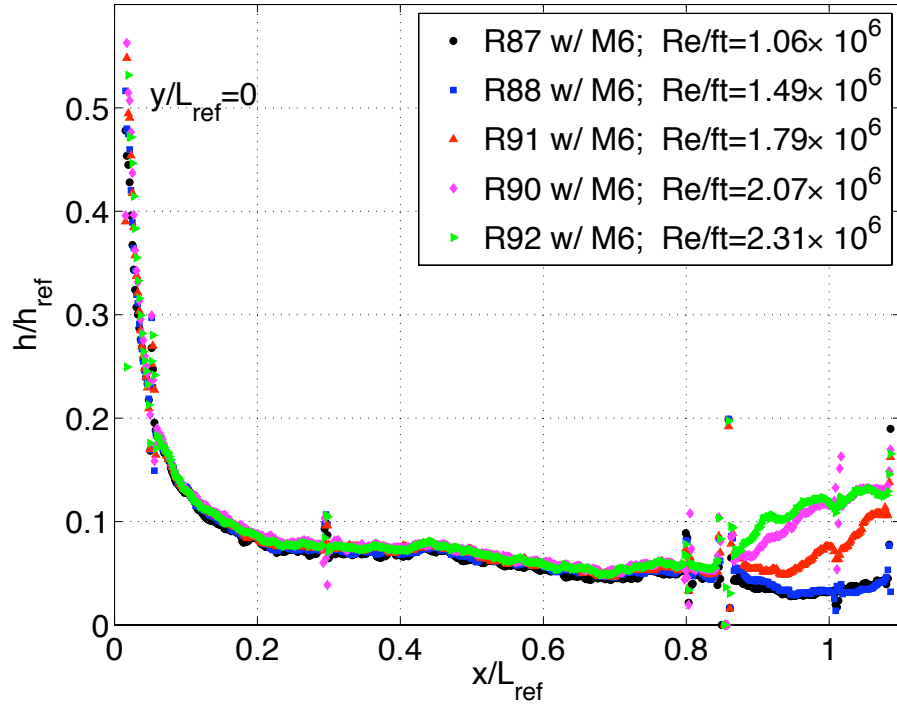


Figure 68. Streamwise line cuts of normalized heat-transfer measurements at $y/L_{ref} = 0$ for model 6 with configuration 12B.

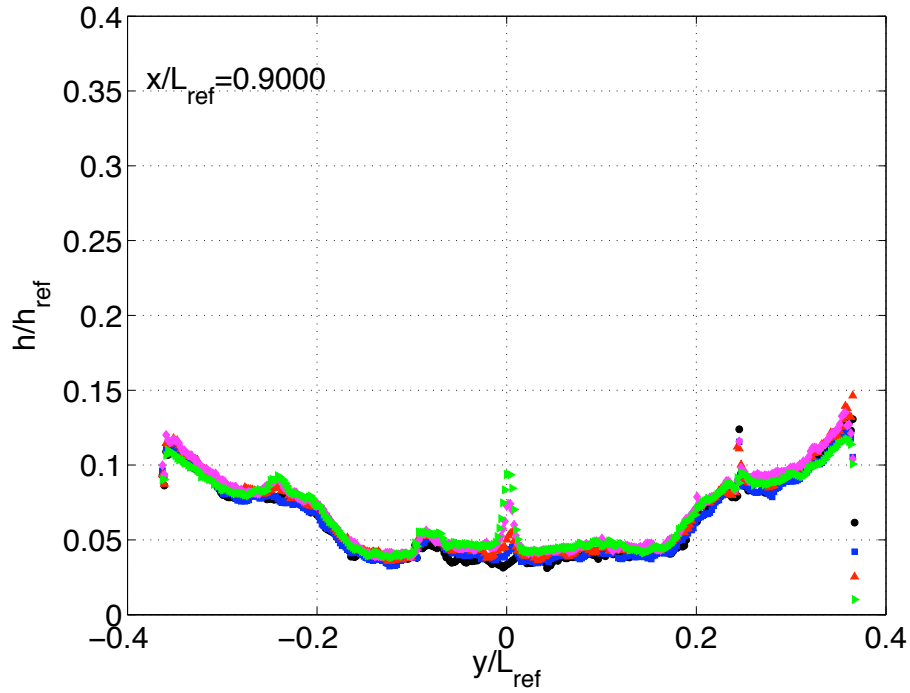


Figure 69. Spanwise line cuts of normalized heat-transfer measurements at $x/L_{ref} = 0.9$ for model 6 with configuration 12B.

Type	x/L	y/L	k (in)
RPB	0.85	0	0.010

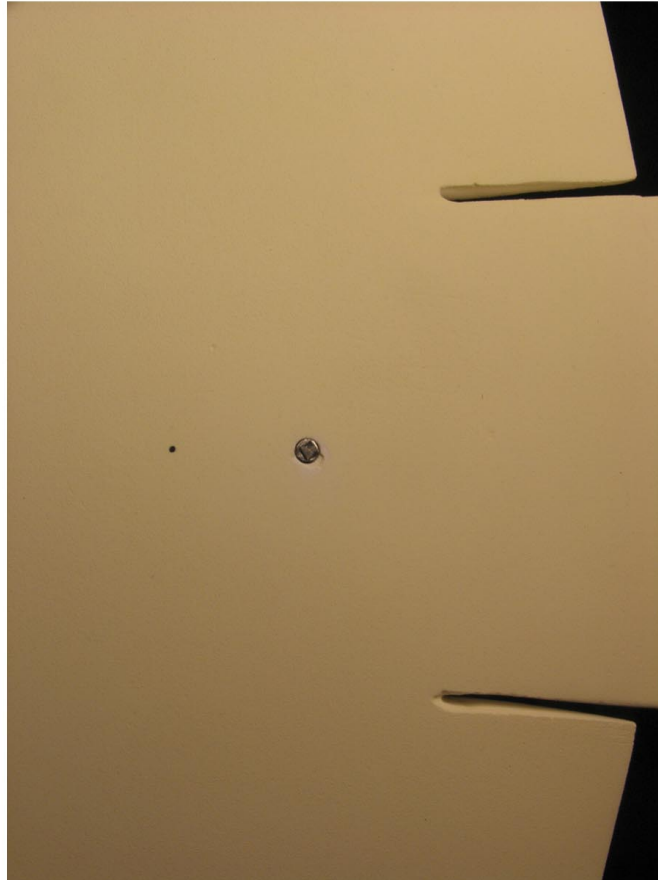


Figure 70. Close-up image of model 6 with configuration 12A.

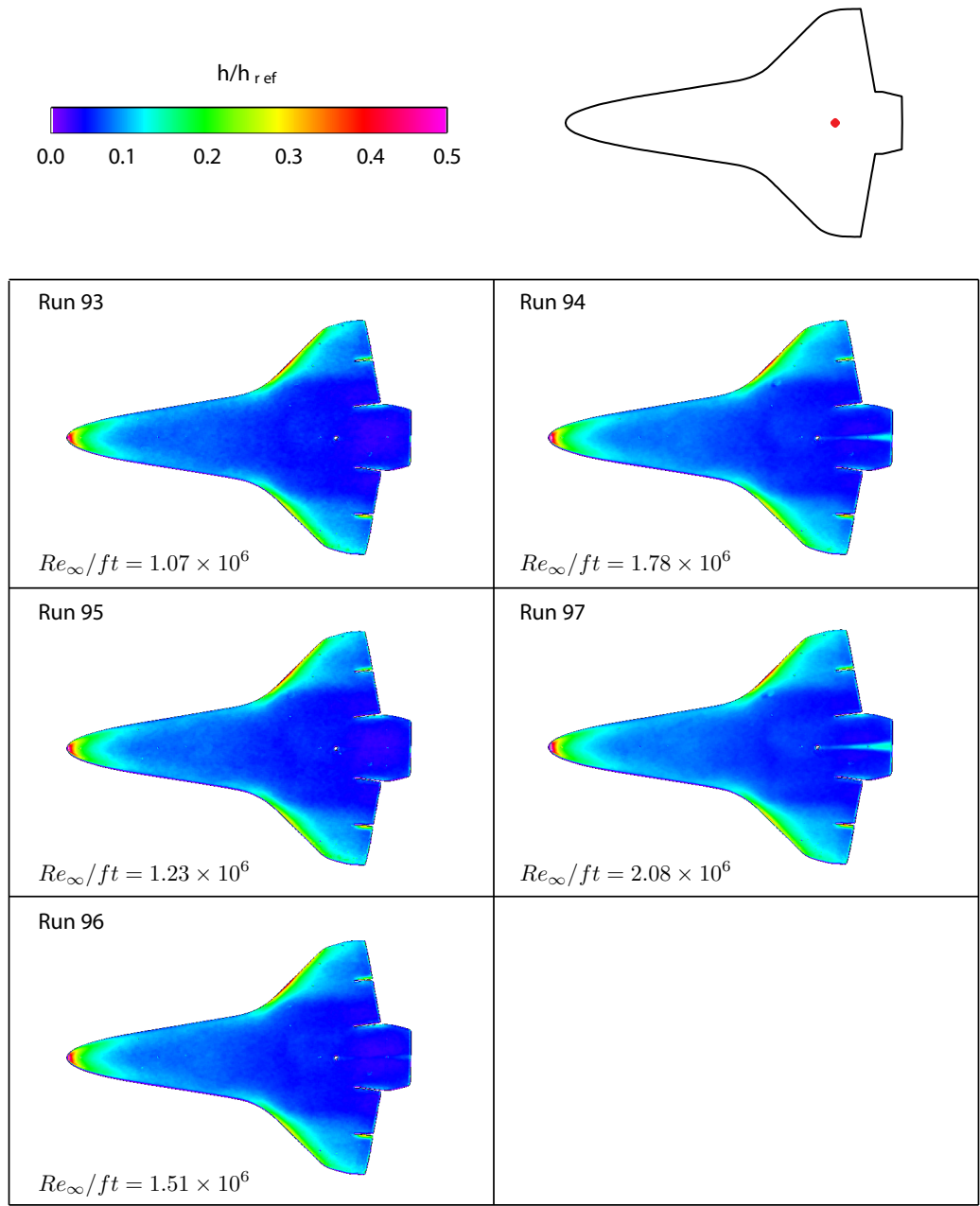


Figure 71. Global aeroheating images for model 6 with configuration 12A.

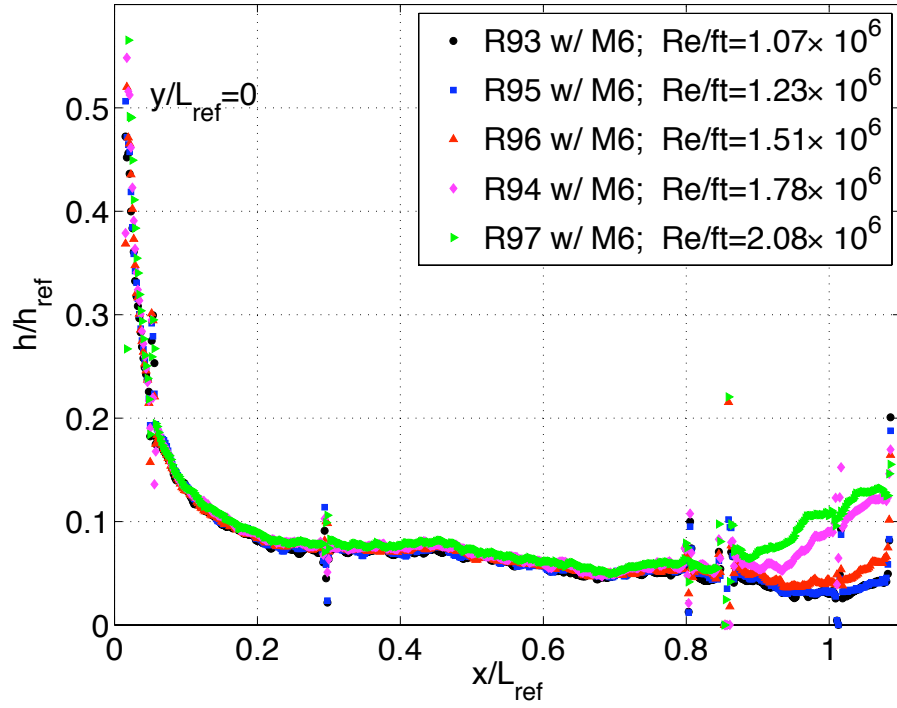


Figure 72. Streamwise line cuts of normalized heat-transfer measurements at $y/L_{ref} = 0$ for model 6 with configuration 12A.

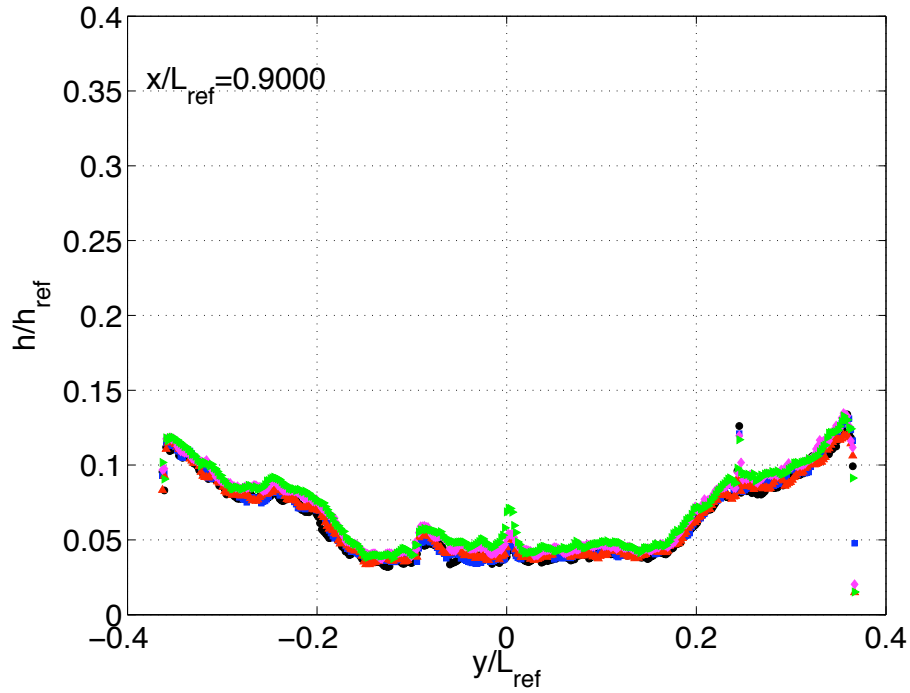


Figure 73. Spanwise line cuts of normalized heat-transfer measurements at $x/L_{ref} = 0.9$ for model 6 with configuration 12A.

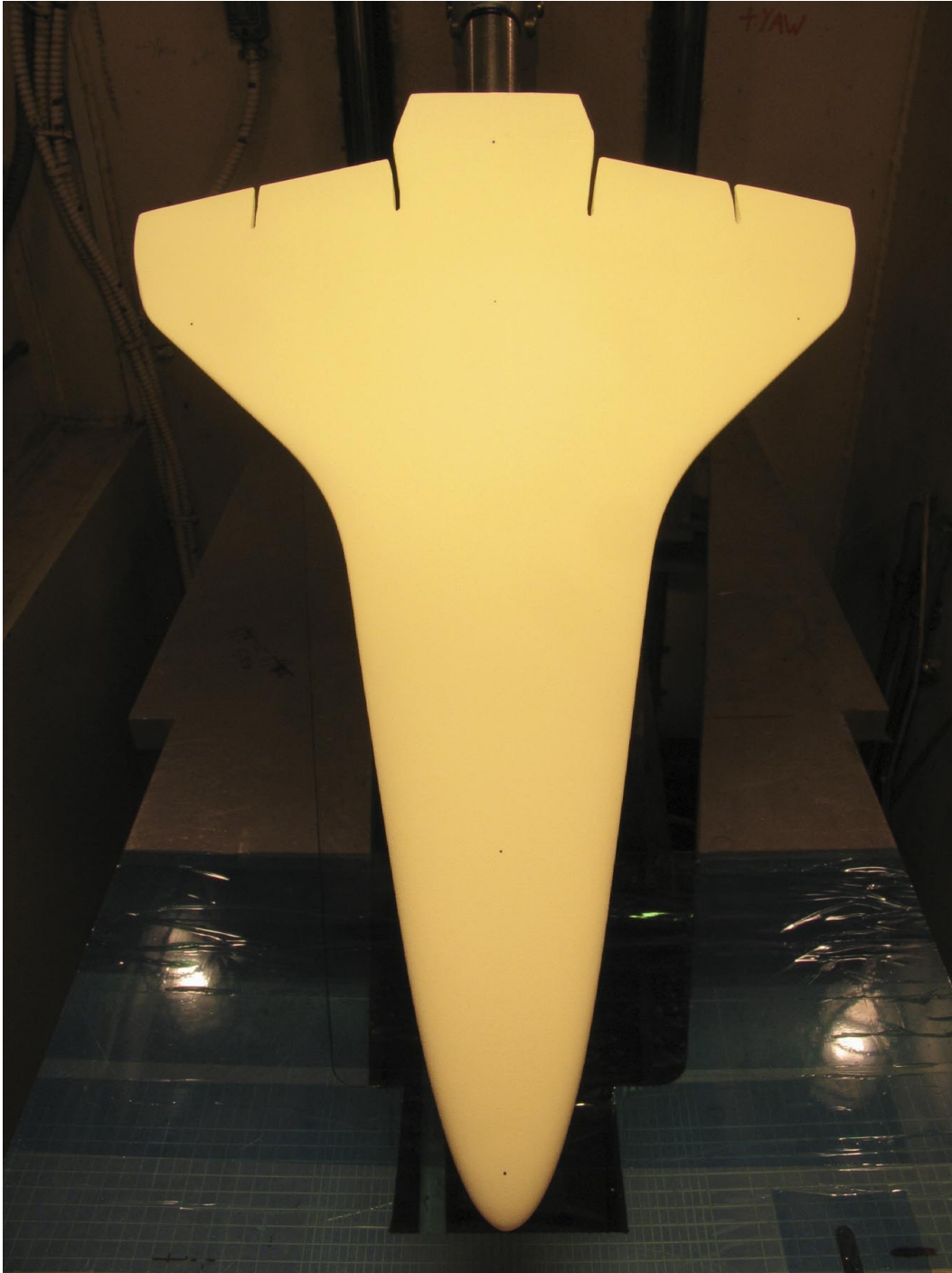


Figure 74. Photographic image of model 7 installed in the 20-Inch Mach 6 Air Tunnel.

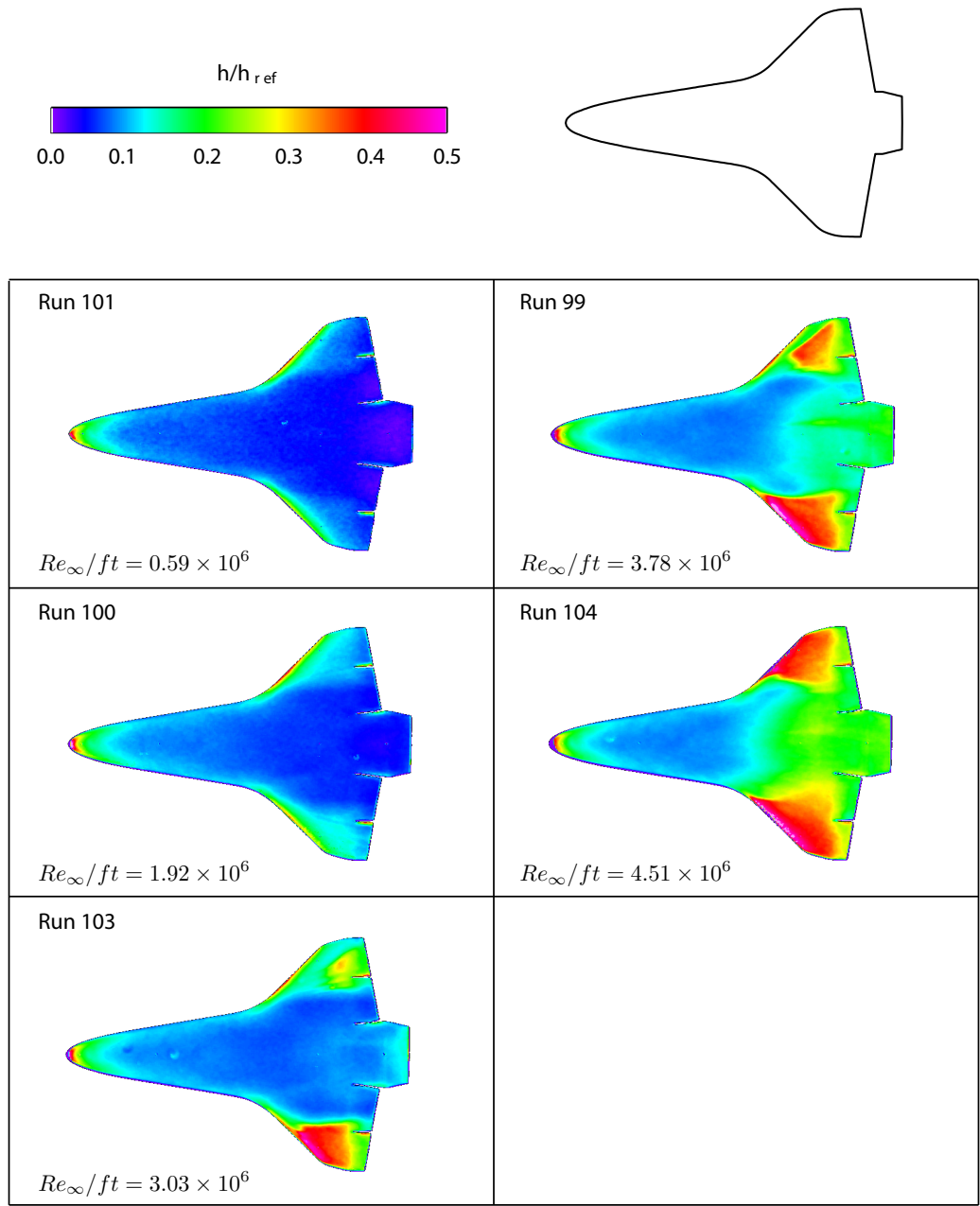


Figure 75. Global aeroheating images for baseline model 7.

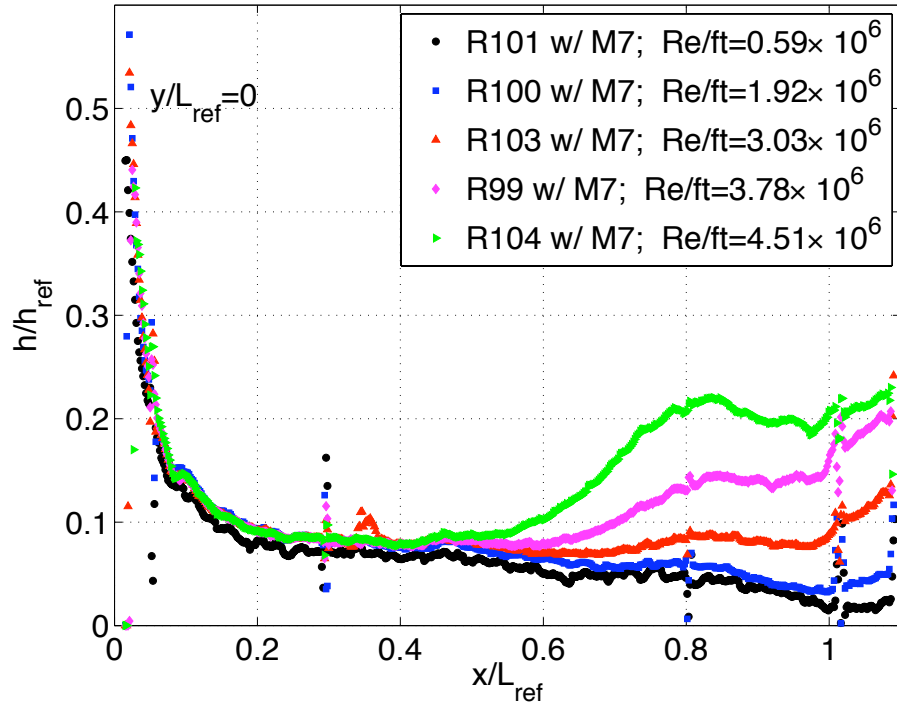


Figure 76. Streamwise line cuts of normalized heat-transfer measurements at $y/L_{ref} = 0$ for baseline model 7.

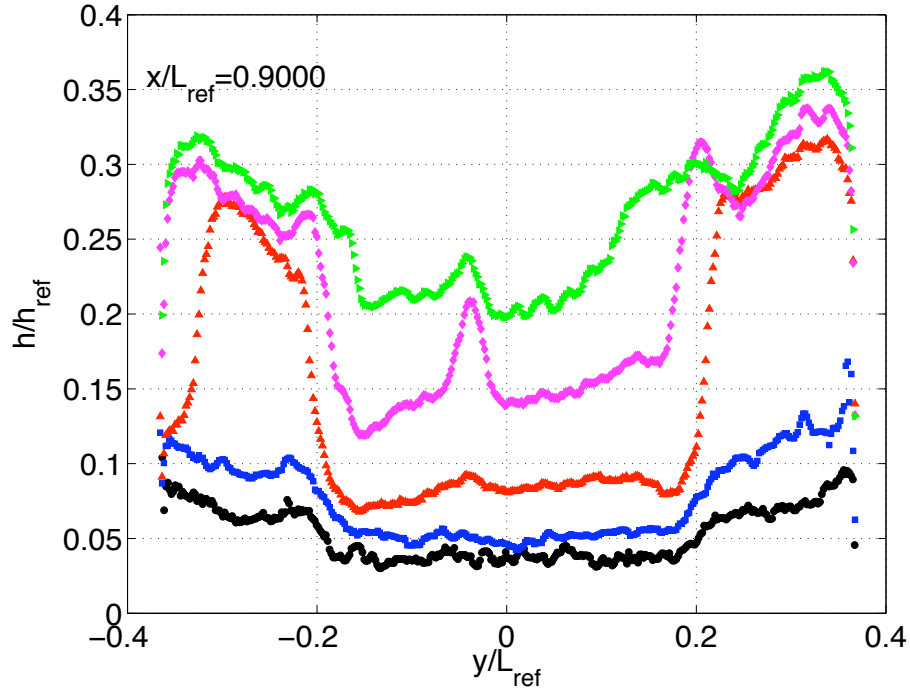


Figure 77. Spanwise line cuts of normalized heat-transfer measurements at $x/L_{ref} = 0.9$ for baseline model 7.

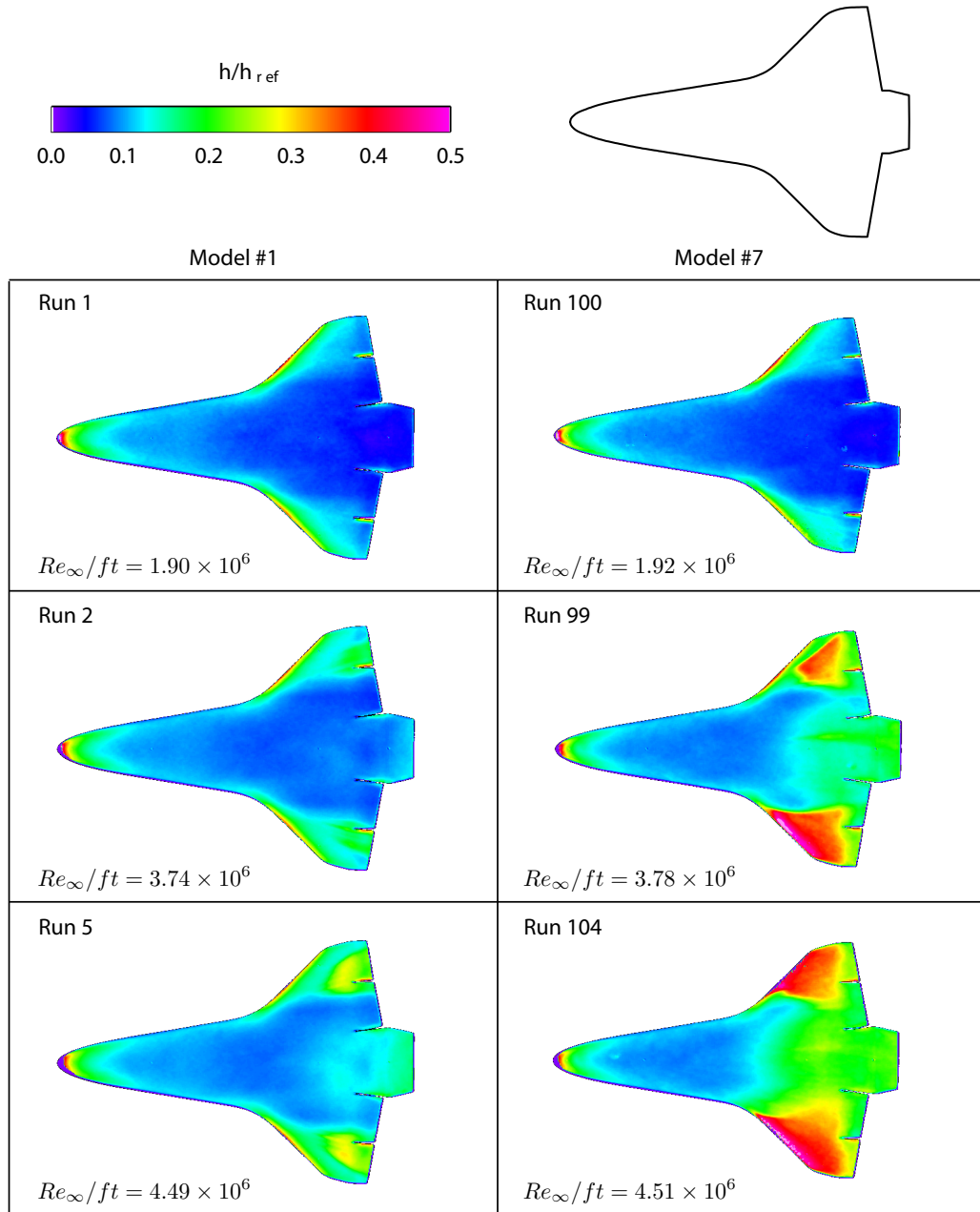


Figure 78. Global aeroheating images for baseline model 7 and baseline model 1.

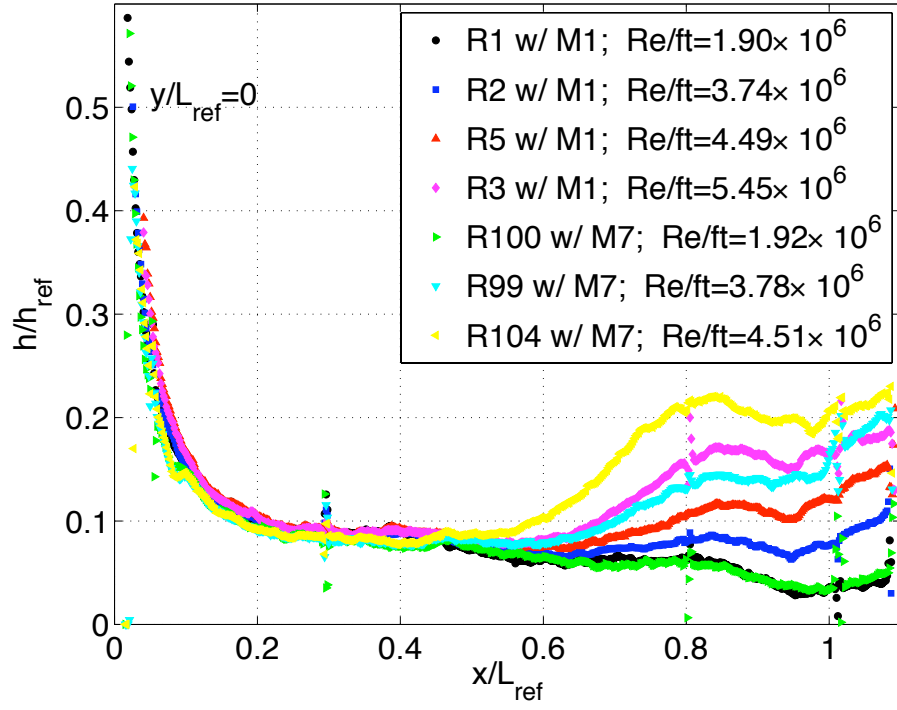


Figure 79. Streamwise line cuts of normalized heat-transfer measurements at $y/L_{ref} = 0$ for baseline model 7 and baseline model 1.

Type	x/L	y/L
Blank	0.74	-0.2348
Blank	0.74	0
Blank	0.74	0.2348

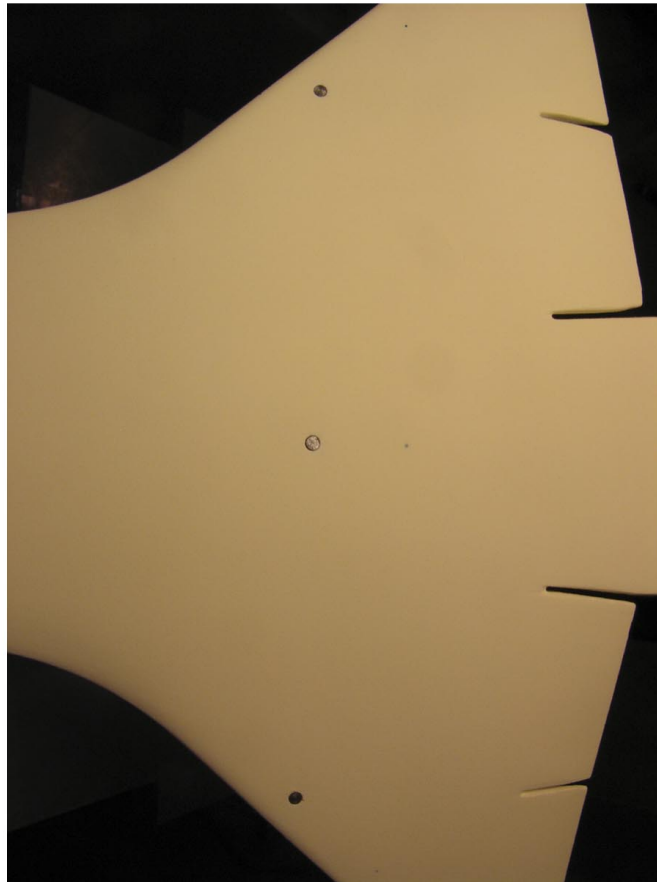
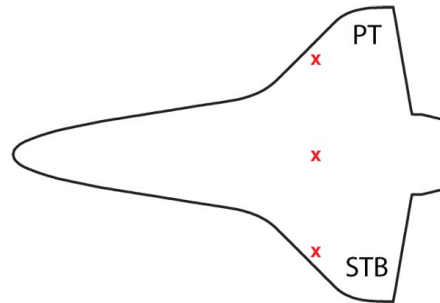


Figure 80. Sketch and close-up image of model 5 with three blank dowels installed.

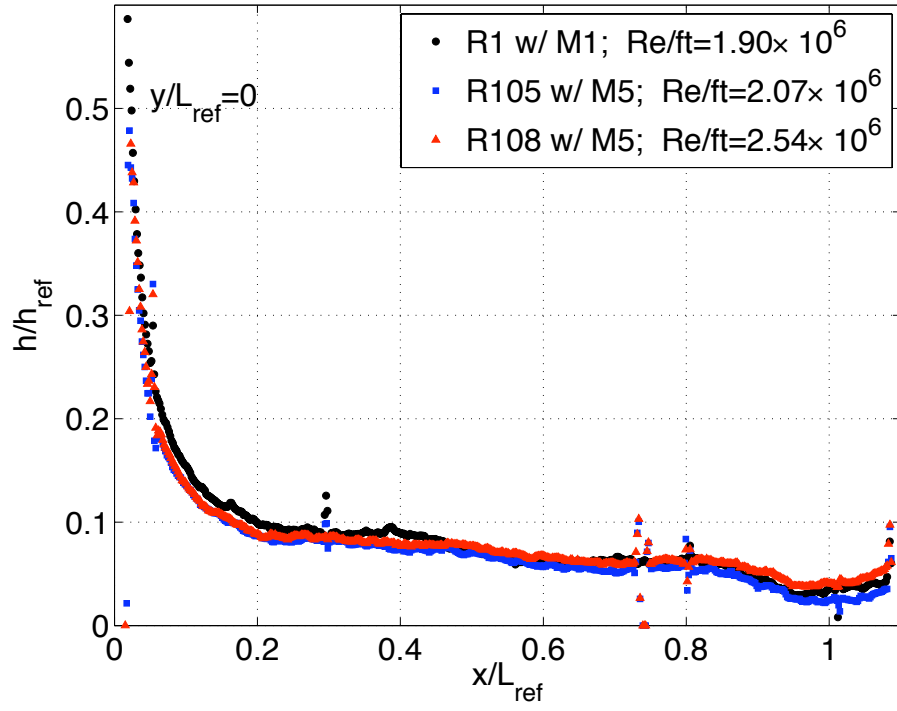


Figure 81. Streamwise line cuts of normalized heat-transfer measurements at $y/L_{ref} = 0$ for model 5 with three blank dowels and baseline model 1.

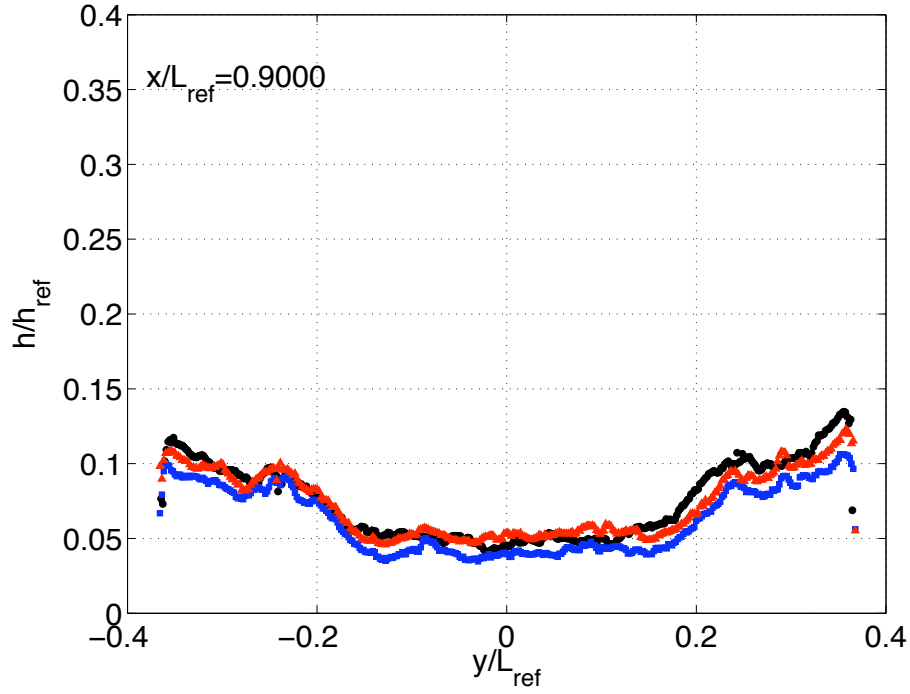


Figure 82. Spanwise line cuts of normalized heat-transfer measurements at $x/L_{ref} = 0.9$ for model 5 with three blank dowels and baseline model 1.

Type	x/L	y/L	k (in)
F(-45°)	0.74	-0.2348	0.007
F(+45°)	0.74	0	0.0011
PB	0.74	0.2348	0.008

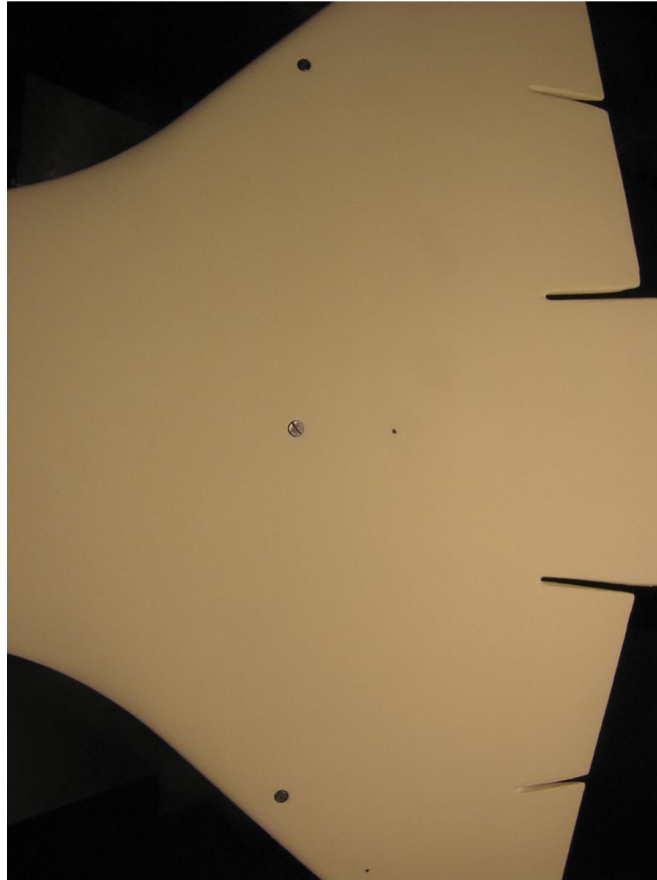


Figure 83. Close-up image of model 5 with configuration 8.

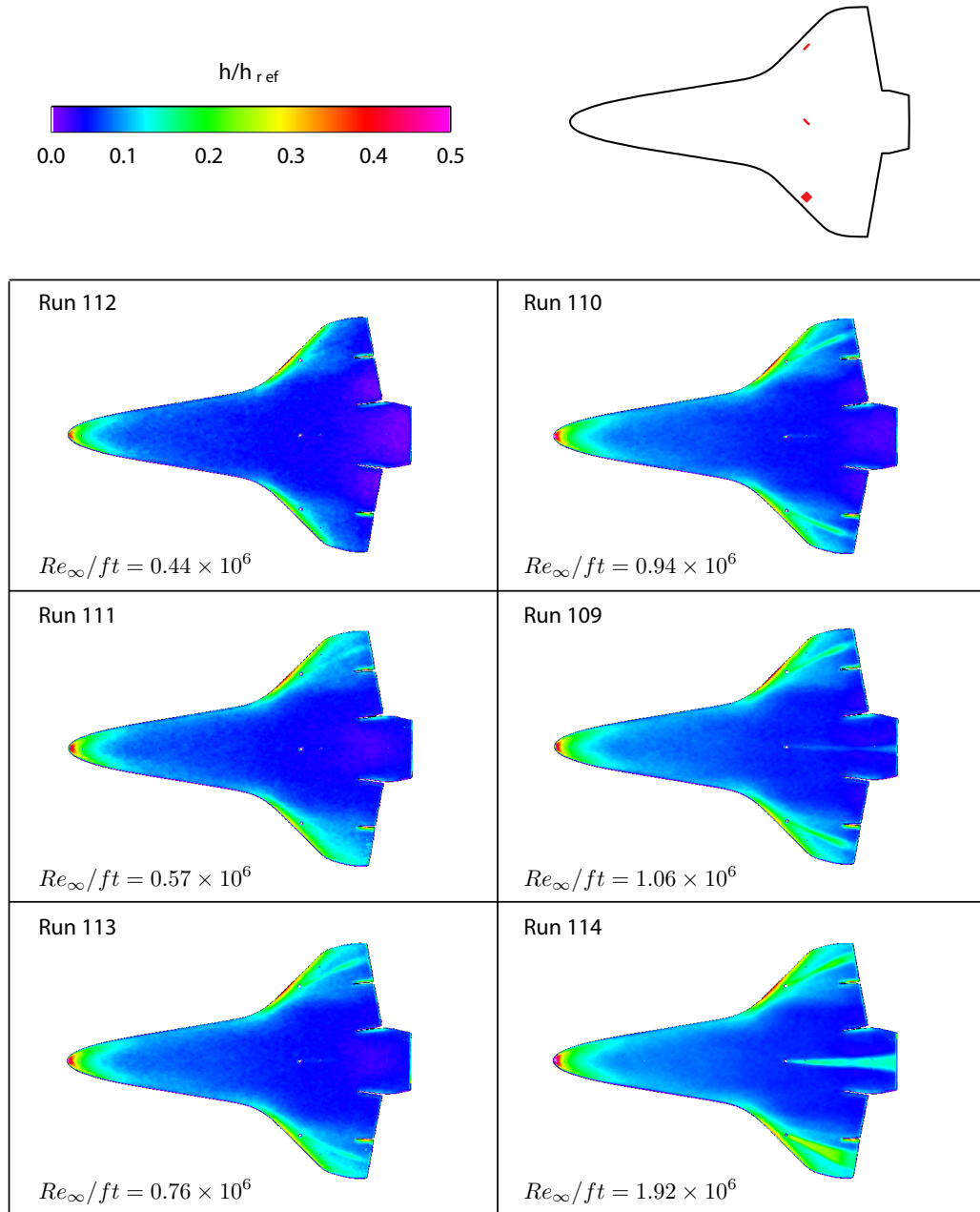


Figure 84. Global aeroheating images for model 5 with configuration 8.

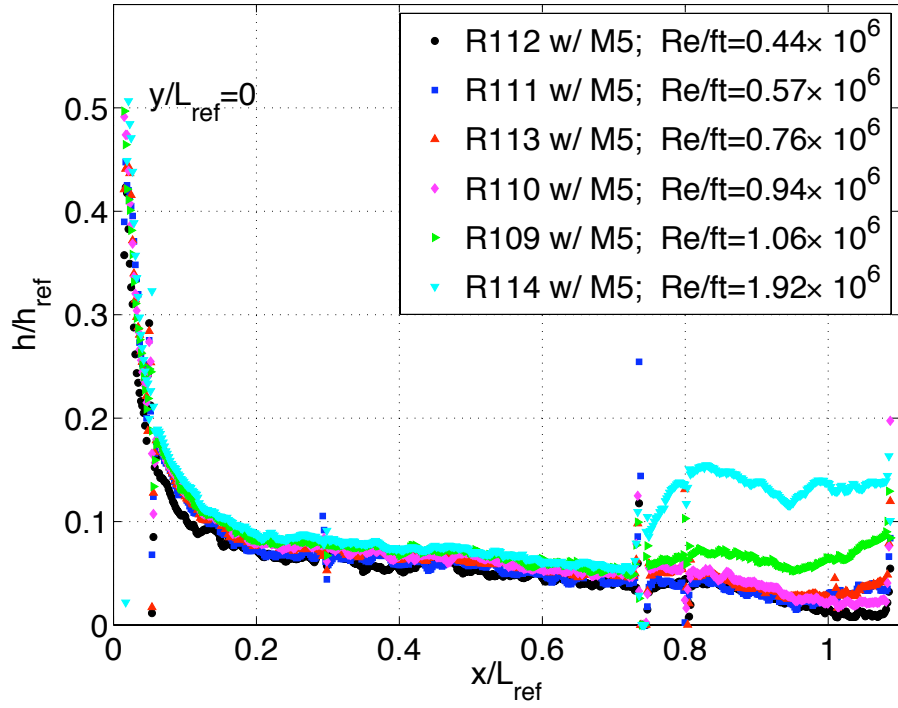


Figure 85. Streamwise line cuts of normalized heat-transfer measurements at $y/L_{ref} = 0$ for model 5 with configuration 8.

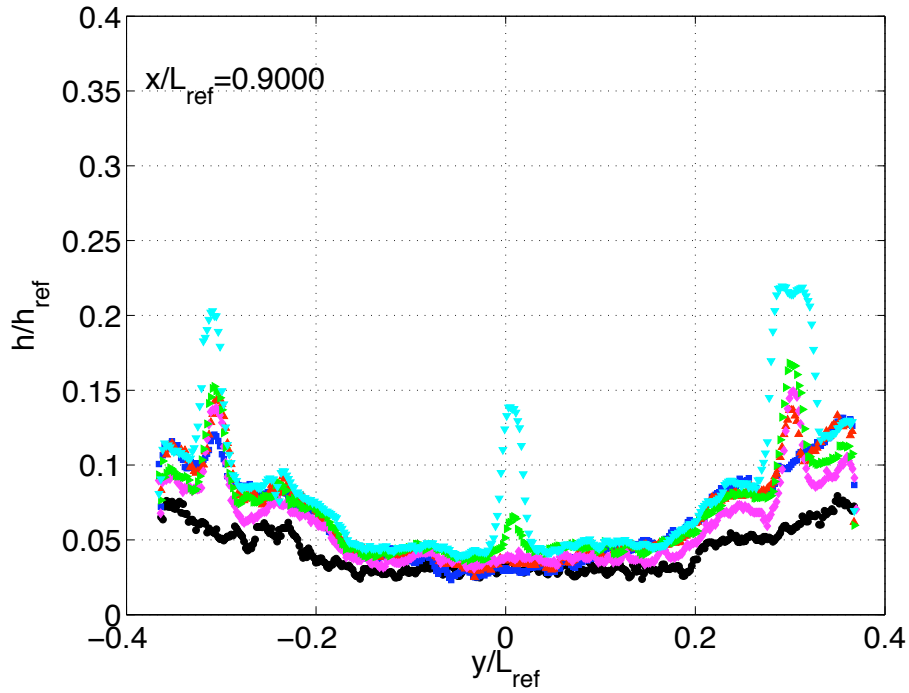


Figure 86. Spanwise line cuts of normalized heat-transfer measurements at $x/L_{ref} = 0.9$ for model 5 with configuration 8.

Type	x/L	y/L	k (in)
F(+45°)	0.74	-0.2348	0.007
PB	0.74	0	0.0010
AF(-45°)*	0.74	0.2348	0.006/0.004

* Highest edge of angled fence, AF, downstream.

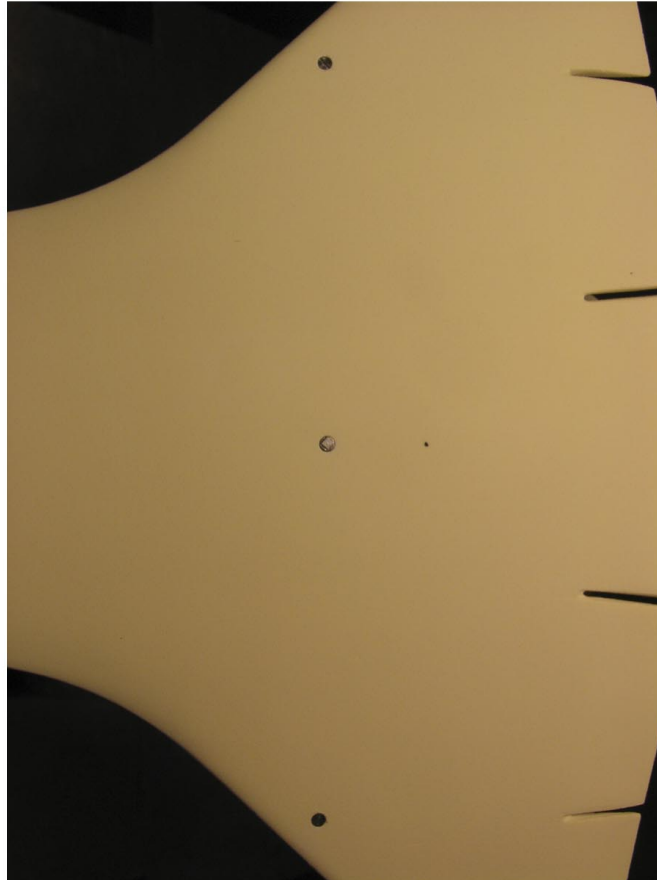


Figure 87. Close-up image of model 5 with configuration 8A.

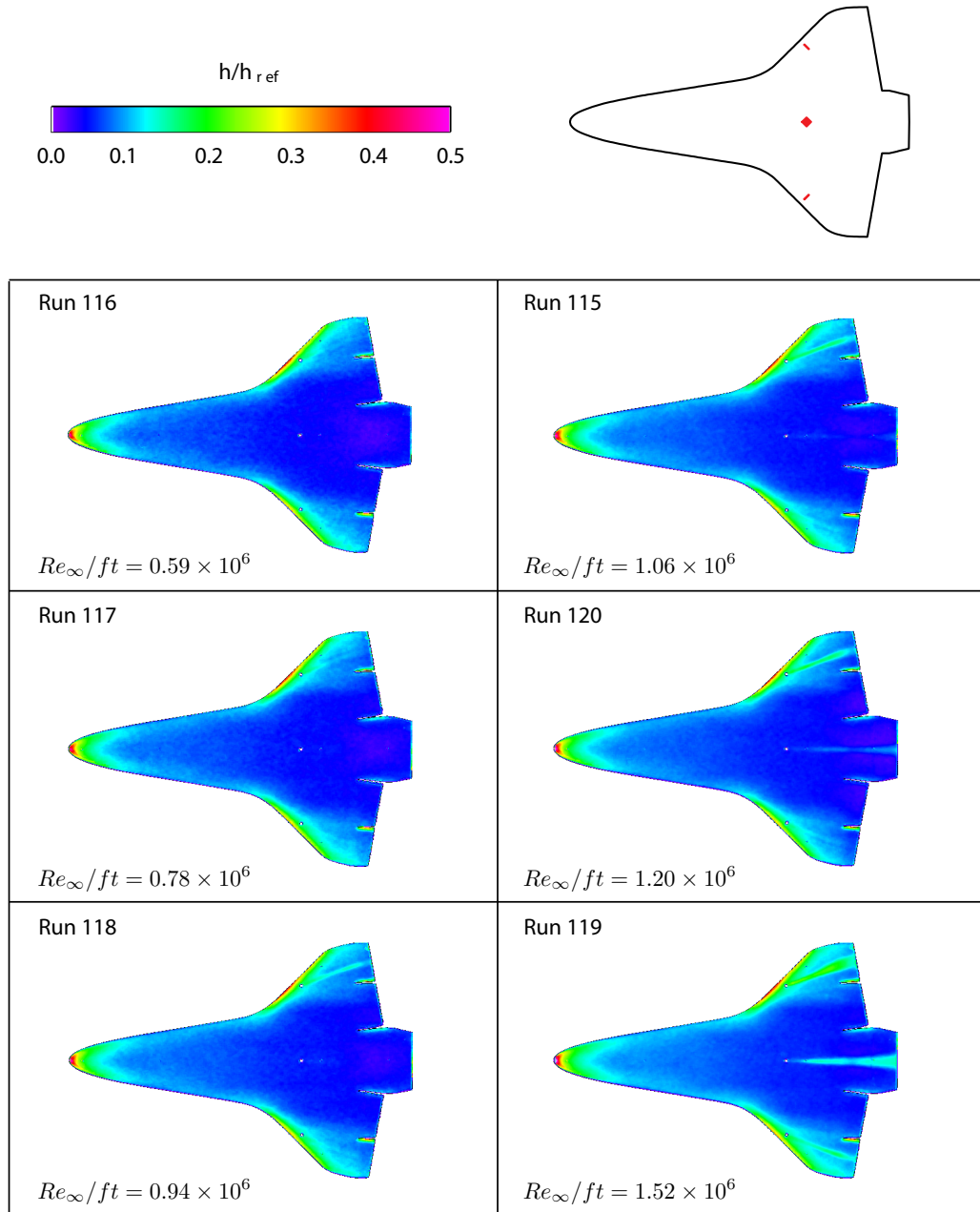


Figure 88. Global aeroheating images for model 5 with configuration 8A.

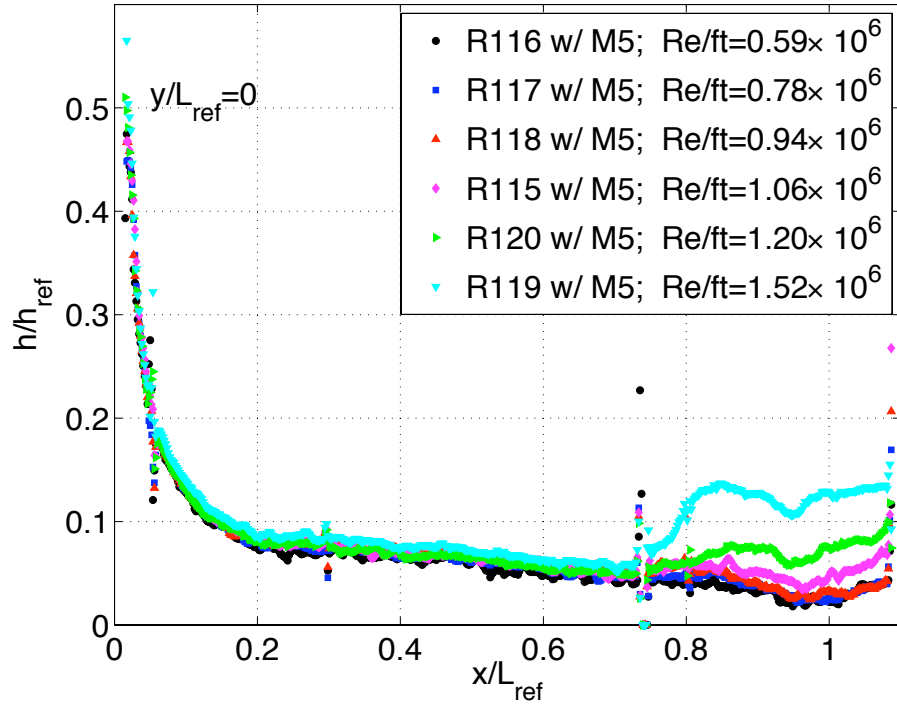


Figure 89. Streamwise line cuts of normalized heat-transfer measurements at $y/L_{ref} = 0$ for model 5 with configuration 8A.

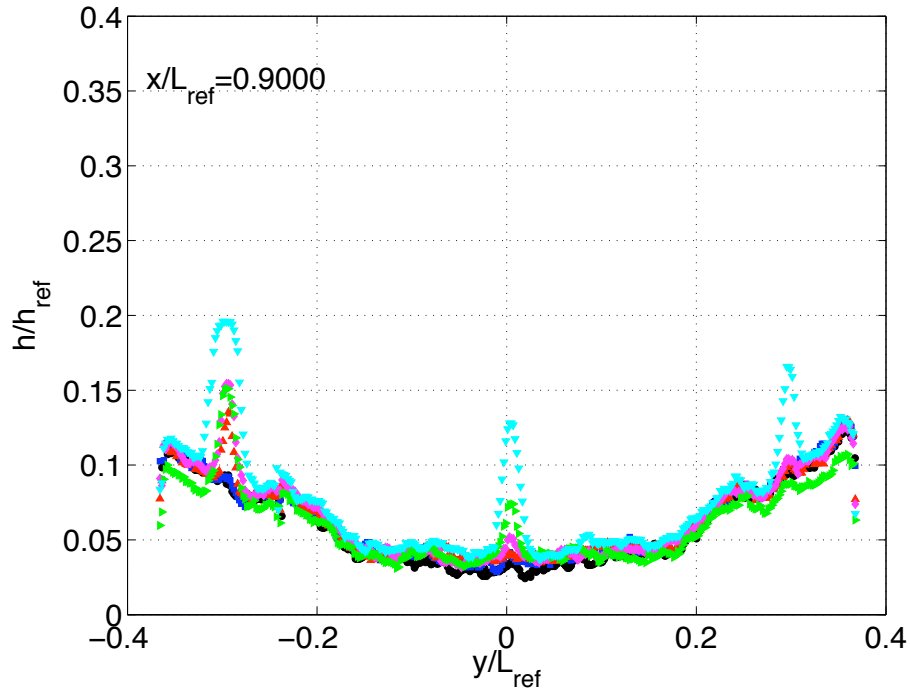


Figure 90. Spanwise line cuts of normalized heat-transfer measurements at $x/L_{ref} = 0.9$ for model 5 with configuration 8A.

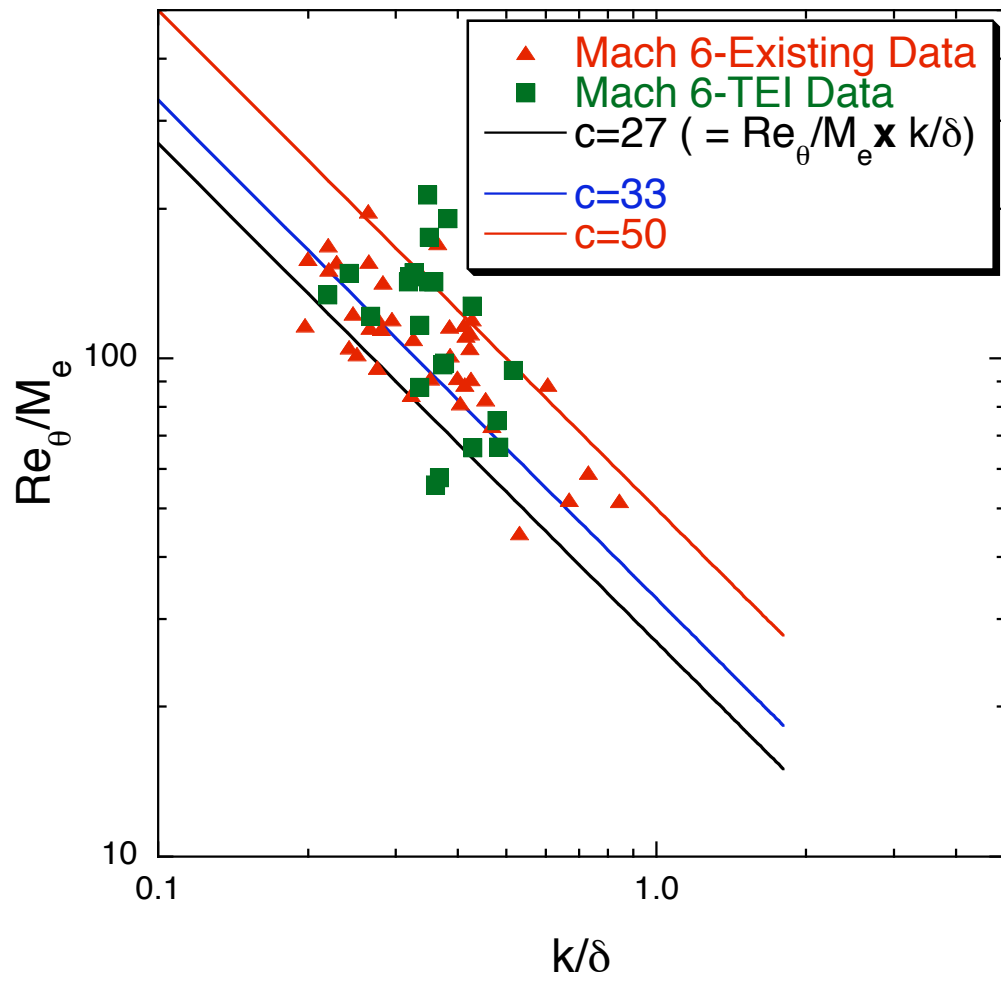


Figure 91. Comparison of existing Mach 6 data and newly acquired TEI data in the parameter space of the BLT Tool v.1.

REPORT DOCUMENTATION PAGE				Form Approved OMB No. 0704-0188	
<p>The public reporting burden for this collection of information is estimated to average 1 hour per response, including the time for reviewing instructions, searching existing data sources, gathering and maintaining the data needed, and completing and reviewing the collection of information. Send comments regarding this burden estimate or any other aspect of this collection of information, including suggestions for reducing this burden, to Department of Defense, Washington Headquarters Services, Directorate for Information Operations and Reports (0704-0188), 1215 Jefferson Davis Highway, Suite 1204, Arlington, VA 22202-4302. Respondents should be aware that notwithstanding any other provision of law, no person shall be subject to any penalty for failing to comply with a collection of information if it does not display a currently valid OMB control number.</p> <p>PLEASE DO NOT RETURN YOUR FORM TO THE ABOVE ADDRESS.</p>					
1. REPORT DATE (DD-MM-YYYY) 01-02-2008		2. REPORT TYPE Technical Memorandum		3. DATES COVERED (From - To)	
4. TITLE AND SUBTITLE Effect of Protuberance Shape and Orientation on Space Shuttle Orbiter Boundary-Layer Transition				5a. CONTRACT NUMBER	
				5b. GRANT NUMBER	
				5c. PROGRAM ELEMENT NUMBER	
6. AUTHOR(S) Rudolph A. King, Scott A. Berry, Michael A. Kegerise				5d. PROJECT NUMBER	
				5e. TASK NUMBER	
				5f. WORK UNIT NUMBER 377816.06.03.03.08	
7. PERFORMING ORGANIZATION NAME(S) AND ADDRESS(ES) NASA Langley Research Center Hampton, Virginia 23681-2199				8. PERFORMING ORGANIZATION REPORT NUMBER L-19425	
9. SPONSORING/MONITORING AGENCY NAME(S) AND ADDRESS(ES) National Aeronautics and Space Administration Washington, DC 20546-0001				10. SPONSOR/MONITOR'S ACRONYM(S) NASA	
				11. SPONSOR/MONITOR'S REPORT NUMBER(S) NASA/TM-2008-215103	
12. DISTRIBUTION/AVAILABILITY STATEMENT Unclassified-Unlimited Subject Category 34 Availability: NASA CASI (301) 621-0390					
13. SUPPLEMENTARY NOTES An electronic version can be found at http://ntrs.nasa.gov .					
14. ABSTRACT This document describes an experimental study conducted to examine the effects of protuberances on hypersonic boundary-layer transition. The experiment was conducted in the Langley 20-Inch Mach 6 Tunnel on a series of 0.9%-scale Shuttle Orbiter models. The data were acquired to complement the existing ground-based boundary-layer transition database that was used to develop Version 1.0 of the boundary-layer transition RTF (return-to-flight) tool. The existing ground-based data were all acquired on 0.75%-scale Orbiter models using diamond-shaped ("pizza-box") trips. The larger model scale facilitated in manufacturing higher fidelity protuberances. The end use of this experimental database will be to develop a technical basis (in the form of a boundary-layer transition correlation) to assess representative protrusion shapes, e.g., gap fillers and protrusions resulting from possible tile repair concepts. The primary objective of this study is to investigate the effects of protuberance-trip location and geometry on Shuttle Orbiter boundary-layer transition. Secondary goals are to assess the effects of gap-filler orientation and other protrusion shapes on boundary-layer transition. Global heat-transfer images using phosphor thermography of the Orbiter windward surface and the corresponding streamwise and spanwise heating distributions were used to infer the state of the boundary layer, i.e., laminar, transitional, or turbulent.					
15. SUBJECT TERMS boundary layer, transition, aeroheating, hypersonic, Orbiter					
16. SECURITY CLASSIFICATION OF:			17. LIMITATION OF ABSTRACT UU	18. NUMBER OF PAGES 100	19a. NAME OF RESPONSIBLE PERSON STI Help Desk (email: help@sti.nasa.gov)
a. REPORT U	b. ABSTRACT U	c. THIS PAGE U			19b. TELEPHONE NUMBER (Include area code) (301) 621-0390

